Gezamenlijke opleiding UHasselt en KU Leuven

Universiteit Hasselt | Campus Diepenbeek | Faculteit Industriële Ingenieurswetenschappen | Agoralaan Gebouw H - Gebouw B | BE 3590 Diepenbeek

Universiteit Hasselt | Campus Diepenbeek | Agoralaan Gebouw D | BE 3590 Diepenbeek
Universiteit Hasselt | Campus Hasselt | Martelarenlaan 42 | BE 3500 Hasselt

---

Faculteit Industriële Ingenieurswetenschappen

master in de industriële wetenschappen: nucleaire technologie

Masterthesis

Optimalisation of a Monte Carlo model regarding skin treatment using the XOFT AXXENT ELECTRONIC BRACHYTHERAPY (EBX) SYSTEM

Sander Grosemans
Scriptie ingediend tot het behalen van de graad van master in de industriële wetenschappen: nucleaire technologie, afstudeerrichting nucleair en medisch

PROMOTOR :
Prof. dr. Brigitte RENIERS

COPROMOTOR :
ing. Dries COLSON

2022
2023

Faculteit Industriële Ingenieurswetenschappen

master in de industriële wetenschappen: nucleaire technologie

Masterthesis

Optimalisation of a Monte Carlo model regarding skin treatment using the XOFT AXXENT ELECTRONIC BRACHYTHERAPY (EBX) SYSTEM

Sander Grosemans

Scriptie ingediend tot het behalen van de graad van master in de industriële wetenschappen: nucleaire technologie, afstudeerrichting nucleair en medisch

PROMOTOR :

Prof. dr. Brigitte RENIERS

COPROMOTOR :

ing. Dries COLSON

Preface

This master's thesis "Optimalisation of a Monte Carlo model regarding skin treatment using the XOFT AXXENT ELECTRONIC BRACHYTHERAPY (EBX) SYSTEM" marked the culmination of my journey to become an Industrial Engineer in Nuclear Technologies from both UHasselt and the KU Leuven. Although this thesis was by far the biggest challenge during my studies, both academically and mentally, I certainly look back on it with fond memories and I am proud of the final product.

I would like to express my gratitude to Prof. Dr. Brigitte Reniers and Ing. Dries Colson for their continuous support and guidance throughout the entire process of completing my thesis. I have lost times of how many times I was completely stuck before one of our meetings. Time after time, they helped me push through, therefore this work is as much theirs as it is mine. Furthermore, I would like I would like to extend my thanks to Burak Yalvac for his valuable assistance in conducting EBT3 film measurements during my research. Lastly, I would like to thank my family and friends for their unwavering support throughout my academic journey and the completion of my master's thesis, especially considering the fact that they had to endure long conversations about my passion for this work.

Table of Contents

List of tables

List of figures

Abstract

Brachytherapy has emerged as a promising treatment modality for nonmelanoma (NMSC) skin lesions due to its excellent dose conformality. Nevertheless, the radioactive nature of brachytherapy sources can be problematic. Therefore, electronic brachytherapy (eBT) replaces these sources with x-ray tubes. This thesis aims to improve an existing Monte Carlo (MC) model of the XOFT Axxent Electronic Brachytherapy (eBx) System to generate transversal dose profiles that are within 10% of measured transversal dose profiles.

Transversal dose profiles specific to the XOFT eBx System were evaluated in three setups: (1) in air, (2) on the surface of a 10x10x4 cm Plastic Water LR phantom, and (3) at 1 cm depth inside the phantom. EBT3 films were employed to measure the transversal dose profiles while the simulated transversal dose profiles were generated using the original TOPAS MC model. A comparison was then made between the corresponding profiles for each setup. Finally, the original TOPAS model was iteratively refined until the best fit was achieved.

The best fit was achieved using a circular electron beam with a diameter of 1.596944 mm and a Gaussian angular distribution of the electrons, with a mean (μ) of 0° and a standard deviation (σ) of 45°, measured relative to the beam axis. This resulted in a maximal difference for the transversal dose profiles of 6.3 % in air, 5.0 % on the surface of the Plastic Water LR phantom and 3.0 % at 1 cm depth inside the phantom. As such, the new model was validated for transversal dose profiles.

Abstract in Dutch

Brachytherapie is een veelbelovende behandelingsvorm voor niet-melanoom gerelateerde huidletsels (NMSC) vanwege de uitstekende dosisconformiteit. De radioactieve aard van de brachytherapiebronnen kan echter problematisch zijn. Bijgevolg vervangt elektronische brachytherapie (eBT) deze bronnen door röntgenbuizen. Deze thesis beoogt een bestaand Monte Carlo (MC) model van het XOFT Axxent Electronic Brachytherapy (eBx) System te verbeteren om transversale dosisprofielen te genereren die binnen 10% liggen van gemeten profielen.

Transversale dosisprofielen voor het XOFT eBx System werden geëvalueerd in drie opstellingen: (1) in lucht, (2) op het oppervlak van een 10x10x4 cm Plastic Water LR fantoom en (3) op een diepte van 1 cm in het fantoom. EBT3-films werden gebruikt voor metingen, terwijl gesimuleerde profielen werden gegenereerd met het originele TOPAS MC-model. Er werd een vergelijking gemaakt tussen de overeenkomstige profielen voor elke opstelling. Vervolgens werd het TOPAS-model iteratief verfijnd tot de beste overeenkomst werd bereikt.

De beste overeenkomst werd bereikt met een circulaire elektronenbundel van 1,596944 mm diameter en een Gaussische hoekverdeling van de elektronen (μ=0°, σ=45°) ten opzichte van de bundelas. Dit resulteerde in maximale verschillen tussen overeenkomstige profielen van 6,3% in de lucht, 5,0% op het oppervlak van het Plastic Water LR fantoom en 3,0% op 1 cm diepte in het fantoom. Bijgevolg was het nieuwe model gevalideerd voor transversale dosisprofielen.

1 Introduction

1.1. Radiotherapy in the modern clinic

On average, a staggering 1 in 2 people will be confronted with cancer at some point in their lifetime [1]. Additionally, there continues to be an upward trend of new cases reported worldwide. In 2012, the International Agency for Research on Cancer (IARC) reported 12.7 million new cases of cancer and 7.6 million cancer-related deaths [2]. In 2018, the IARC reported 18.1 million new cases of cancer and 9.6 million fatalities [3]. Consequently, this high rate of occurrence is the main reason for cancer being the leading cause of death in the modern world [4]. On the other hand, significant progress has been made by medical personnel and researchers to understand, treat, and, most importantly, prevent the metastasis of cancer[4]. The most common and effective forms of treatment can be distinguished into 5 categories: surgery, immunotherapy, chemotherapy, hormonal therapy and radiation therapy [4]. The latter continues to be an essential part in the battle of cancer, as 50% of patients diagnosed with a form of cancer are subjected to radiotherapy at some point during their treatment [4, 5]. The main goal of radiotherapy is to damage the DNA in tumour cells by irradiating the tumour with charged particles like electrons and photons. As such, the application of radiotherapy can (1) cure cancer, (2) slow or stop cancer growth, (3) lower the risk of recurrence and (4) improve the quality of life of palliative patients [5, 6]. However, as radiotherapy indiscriminately damages cells in the patient’s body, healthy cells can be damaged similarly. This can result in side effects such as hair loss, swelling and possibly even radiation induced tumours [7]. Therefore, an adequate treatment plan is paramount to limit the irradiation of healthy tissue. Radiotherapy can treat just about every type of cancer, including prominent applications in the fight against cervical, prostate, and breast cancers. Radiotherapy can be divided into 2 subcategories. Teletherapy irradiates the patient from outside the patient’s body, while brachytherapy irradiates the patient from inside or near the body.

1.2. Brachytherapy

1.2.1 Conventional brachytherapy

The etymology of the word Brachy can be traced back to ancient Greece, where *brachios* indicated something or someone being in close vicinity [8, 9]. Indeed, in conventional brachytherapy, radioactive sources are placed inside or close to the patient's body. There are two types of brachytherapy depending on the dose rate of the source [8].

Low dose rate (LDR) brachytherapy entails the implementation of a radioactive source over an extended period of time [8]. As such, the sources may remain in the patient for up to a week. However, a particular type of LDR brachytherapy called permanent seed brachytherapy uses sources with a particularly low activity that consequently remain permanently in the patient. These sources, which are often called seeds, are tiny metal containers carrying radionuclides whose activity is negligible after a few months. Figure 1 displays a handful of seeds containing the radio-isotope Iodine-125.

Figure 1: Radioactive seeds (which have a size comparable to a grain of rice) filled with Iodine-125 [10]

Brachytherapy treatments categorized under high dose rate (HDR) brachytherapy are typically administered over a much shorter time window than LDR brachytherapy [8]. Ranging from 5 to 20 minutes, these types of treatments involve placing highly radioactive sources close to or inside the patient. Indeed, the HDR brachytherapy devices are equipped with long, hollow tubes called applicators in which the HDR sources are transported to certain positions pre-set by the physician. These locations are referred to as the dwell positions and are chosen as to maximize the efficacy of the treatment. After the treatment time has expired, the sources are transferred back into the HDR brachytherapy device. Figure 2 depicts a HDR brachytherapy device used to treat a variety of cancers.

Figure 2: HDR brachytherapy device equipped with applicators [11]

Some clinicians perceive brachytherapy to be the ultimate form of a conformal radiotherapeutic treatment as it is unrivalled in its ability to deliver a very large dose to the tumour (or the gland which holds the tumour) while simultaneously limiting the dose absorbed by the surrounding healthy tissue [12, 13]. This results in a lower rate of side effects (previously outlined in section 1.1) after administering radiotherapy compared to teletherapy. Additionally, brachytherapy proves to be very cost effective. On the other hand, it should be noted that brachytherapy also has some unfavourable effects which are not present in teletherapy treatments. Most of these disadvantages stem from the inherent nature of a radioactive source. During a radioactive material's lifecycle, it continuously strives to transition to a stable state. During this phenomenon, several particles are emitted which in turn can translate into a dose delivered to the patient. This means that (1) there is no way to turn off the radioactive sources during the treatment and (2) that the dose delivered to the patient depends on the activity of the source used in the brachytherapy treatment. This gives way to an array of different problems when brachytherapy is used. Firstly, the sources need to be replaced on a regular basis when their activity has decreased below the threshold that is deemed necessary for treatment. As a consequence, these old sources contribute significantly to the nuclear waste of a clinic. Secondly, a potential risk could arise when the sources are stolen since the radioactive materials in the sources could theoretically be repurposed for malignant means. Logically, the clinics try to limit this risk by constructing rules and security systems. These in turn result in tedious and long routines for the medical personnel. Thirdly, a hypothetical accident where the source gets stuck in the patient during the treatment would have catastrophic consequences as the source cannot be turned off. Lastly and most importantly, there is no way to account for inhomogeneities and differences in radiosensitivity between different tissues, as the dose delivered in the patient depends on the activity of the source used in the patient.

Due to a combination of several factors, including (1) the aforementioned disadvantages, (2) the dislike of invasive procedures of some patients and (3) the advanced knowledge required to effectively carry out a treatment, the interest in brachytherapy has declined in several countries over the past few decades. Indeed, the Belgium Health Care Knowledge Centre (KCE) reported that the number of brachytherapy treatments administered in Belgium decreased by almost 50% between 2007 and 2019 [14]. A national survey carried out by the Belgian SocieTy of Radiation Oncology (BeSTRO) in 24 Belgian radiation oncology centres concluded that brachytherapy was only used in a select few cases [15]. Furthermore, modern variations are often not covered. As such, patients have no regular access to these methods of treatments which could potentially lead to suboptimal results. A similar downtrend was also recorded in the United States. [16] revealed that the number of prostate brachytherapy treatments carried out on 182,000 eligible patients decreased from 44% in 2004 to 38% in 2009. More recently, [17] conducted a study on the employment of brachytherapy for the treatment of 7,654 patients diagnosed with cervical cancer. They registered a decrease in usage of brachytherapy from 96.7% in 2004 to 86.1% in 2011.

Coincidentally, the alternative in the form of teletherapy treatments increased in popularity with use of stereotactic radiotherapy (SBRT) and intensity-modulated radiotherapy (IMRT) increasing from 3.3% to 13.9% in the same timeframe. However, several specialists in the field do not agree with this late evolution and emphasize that the main goal of radiotherapy, is and always will be, to treat patients effectively and maximize survival rate. It is therefore remarkable that brachytherapy proves to be especially effective in the treatment of the cervical and prostate cancers. Recent research concluded that (1) the cure rate of cervical cancers could be elevated by 10 % on average across the United States and (2) that there is no better option for the treatment of localized prostate cancer than brachytherapy, provided high-quality brachytherapy is administered [13]. As such, specialists in the field have been pushing for a renaissance of brachytherapy in the modern clinic. In Belgium similar efforts are made by BeSTRO to spark interest in the use of brachytherapy in Belgium by including more information about brachytherapy in their training program [15].

1.2.2 Electronic Brachytherapy & skin cancer

A very promising development in the field of brachytherapy is the use of Electronic Brachytherapy (EBT). One of the only similarities between conventional brachytherapy and EBT is the way they are administered. Contrary to the radioactive sources used in brachytherapy, no radioactive sources are used in EBT. Instead EBT opts to use a miniaturized version of the X-ray tube, which has historically been used for diagnostic purposes. In these X-ray tubes, electrons are accelerated from the cathode to the target anode, producing photons due to the interactions of these electrons in the target. This adaptation eliminates the majority of the disadvantages related to the radioactive sources mentioned in section 1.2.1. Indeed, in contrast to these sources, (1) the x-ray tubes stop emitting photons when the voltage supply has been turned off and (2) the dose rate and the maximal photon energy can be adapted by changing the tube current and tube voltage, respectively. While conventional brachytherapy is one of the oldest forms of radiotherapy which has been used for more than a millennium, EBT is a relatively young spinoff with the production of the first prototype dating back to 1996 [18]. Indeed, Alan Sliski of the Photoelectron Corporation designed a miniaturized x-ray source that used tube voltages ranging from 10 kV to 90 kV using currents from 1 nA to 100 µA [19]. The system, which was designed for interstitial radiosurgery, used a very small accelerator that generated x-rays at the end of a needle-shaped probe [18, 19]. Nowadays there are 6 different vendors who each produce variations of EBT systems. The systems and their manufacturers are XOFT(iCAD), Intrabeam (Zeiss), Papillon (Ariane), Photoelectric Therapy (Xstrahl), SRT 100 (Sensus Healthcare) and finally Esteya (Elekta) [19].

An interesting application of EBT is found in superficial brachytherapy to treat skin cancer, where it can be used to complement conventional brachytherapy, various teletherapy treatments and surgery. There are 3 main types of skin cancer: melanoma, basal-cell skin cancer (BCC) and squamous-cell skin cancer (SCC) [20]. Melanoma is the most aggressive skin cancer and has an average 5-year survival rate across all the SEER stages of 94% [21]. However, melanoma is known for its rapid proliferation after it establishes itself in the skin. As such, the distant SEER stage, where the cancer has spread throughout the body only has a 32% 5-year survival rate [21]. Melanomas are often surgically removed as they are generally not radiosensitive [22]. Conversely, in some cases, radiotherapy is used on very early-stage melanomas or after surgery to minimize the risk of recurrence. BCC and SCC are often grouped under the umbrella term nonmelanoma skin cancer (NMSC). They are less aggressive than melanoma and consequently have a higher survival rate. The 5-year survival rate across all the SEER stages is 100% and 95% for BCC and SCC, respectively [23]. Although deaths caused by BCC and SCC are relatively uncommon, the incidence continues to increase [24]. Additionally, NMSCs often appear in sun-exposed skin [24]. Considering the extravagant appearance of these malignancies this may severely limit quality of life. Therefore, certain treatments must be devised and tested to treat NMSCs exclusively.

For the treatment of skin cancer, superficial EBT and conventional superficial brachytherapy appear to have several unrivalled qualities. Firstly, brachytherapy does not incur dose build up at the surface, as the source is located inside or close to the tumour [12]. This is often not the case using other radiation techniques like teletherapy, where the source is located outside the patient's body and, therefore, relatively far away from the tumour. Secondly, the excellent dose conformity that brachytherapy offers results in limited irradiation of the subcutaneous layer, which allows for safe hypofractionation [12]. Finally, superficial brachytherapy, like regular brachytherapy, is cost effective [12].

1.3 Outline of thesis

1.3.1 Earlier work

This thesis is part of a larger initiative where several students work in close cooperation with NuTeC and MAASTRO clinic to construct and validate a Monte Carlo (MC) model capable of characterising the dose output of the XOFT Accent electronic brachytherapy (eBx) System regarding superficial skin EBT treatment. As such, In her thesis, M. Wieme modelled a virtual model of the XOFT eBx System equipped with a 35 mm conical applicator, which was created using the Monte Carlo tool TOPAS [25]. This model was then validated for Half value layers (HVL) and the photon spectrum. On the other hand, S. Arits used a similar model which was validated for Percentual Depth Dose (PDD) measurements [26]. Additionally, several other measurements and experiments were carried out using the XOFT eBx System. These can be found in [25] and [26].

The PDD curves were measured using an Exradin A20 ionization chamber in a 15x15x2 cm phantom of (a) RW3 and (b) Plastic Water LR [26]. These were then compared to PDD curves generated in TOPAS using smaller 15x15x4mm phantoms constructed out of the same materials [26]. These smaller phantoms were embedded with a cylinder corresponding to the sensitive volume of the Exradin A20 ionization chamber, in which the absorbed dose was measured [26]. The results are shown in figure 3 and 4 for RW3 and Plastic Water LR, respectively.

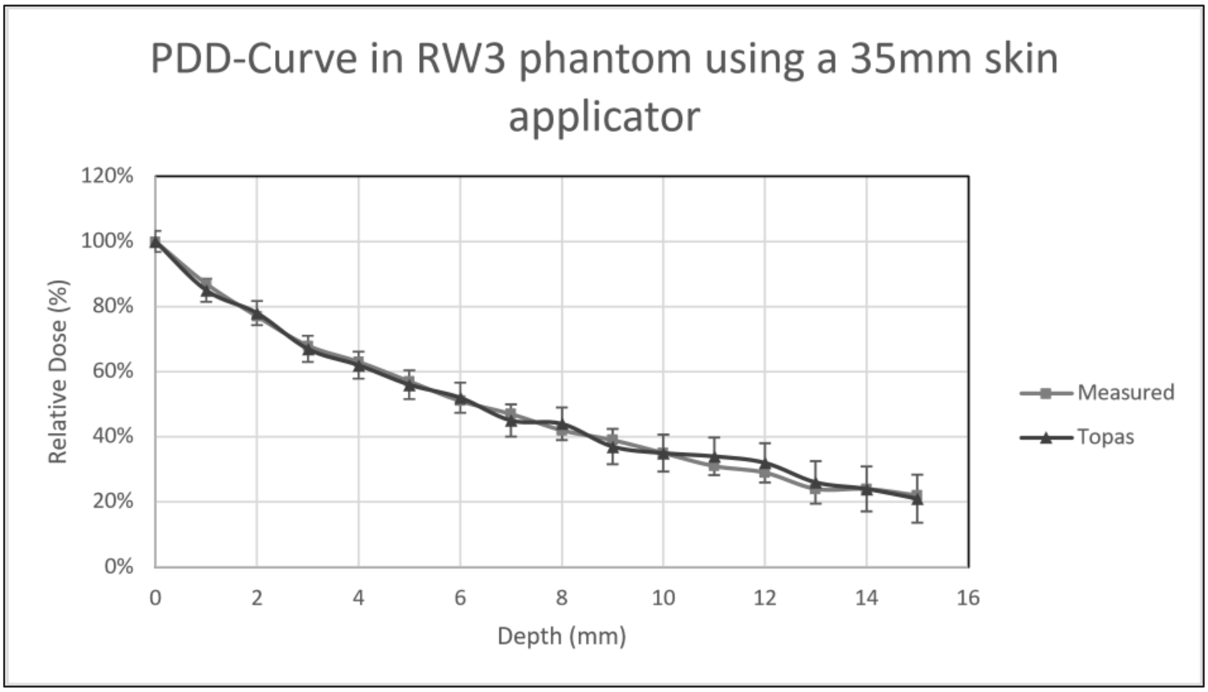

Figure 3: Measured and simulated PDD curves in RW3 using a conical 35 mm applicator [26, p. 66]

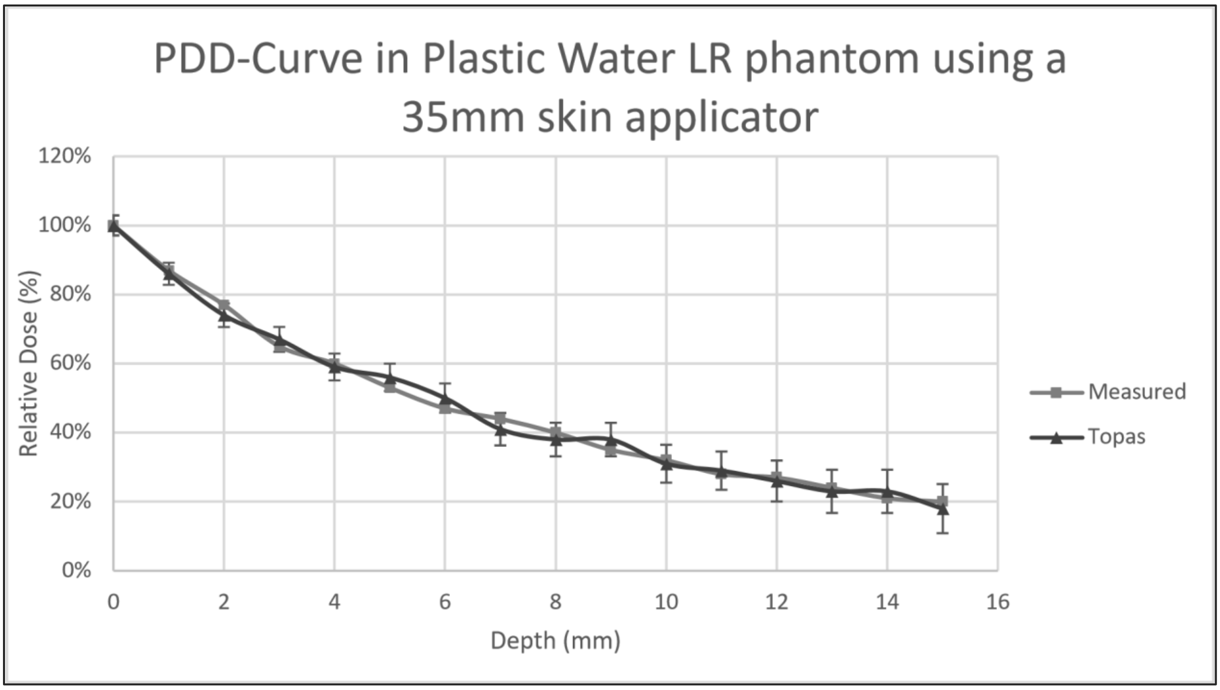

Figure 4: Measured and simulated PDD curves in Plastic Water LR using a conical 35 mm applicator [26, p. 67]

Although the simulated PDD curves were found to be noisier with increasing depth, the difference between the measured PDD curves and the simulated PDD curves never exceeded the uncertainty intervals. Therefore, it was concluded that the model was validated for the prognosis of PDD curves in both RW3 and Plastic Water LR phantoms.

The second batch of measurements tried to determine if the same TOPAS MC model could predict transversal dose profiles using the aforementioned RW3- and Plastic Water LR phantoms. The transversal dose profiles were recorded by placing EBT3 films on the surface of each phantom and at 1 cm depth in each phantom. After the EBT3 films were irradiated using the S700 source inside the XOFT eBx System, they were subsequently scanned and evaluated using the accompanying software filmQA pro™ v.7. Finally, the measured and simulated transversal dose profiles on the surface of the RW3 phantom were compared. Figure 5 shows the results.

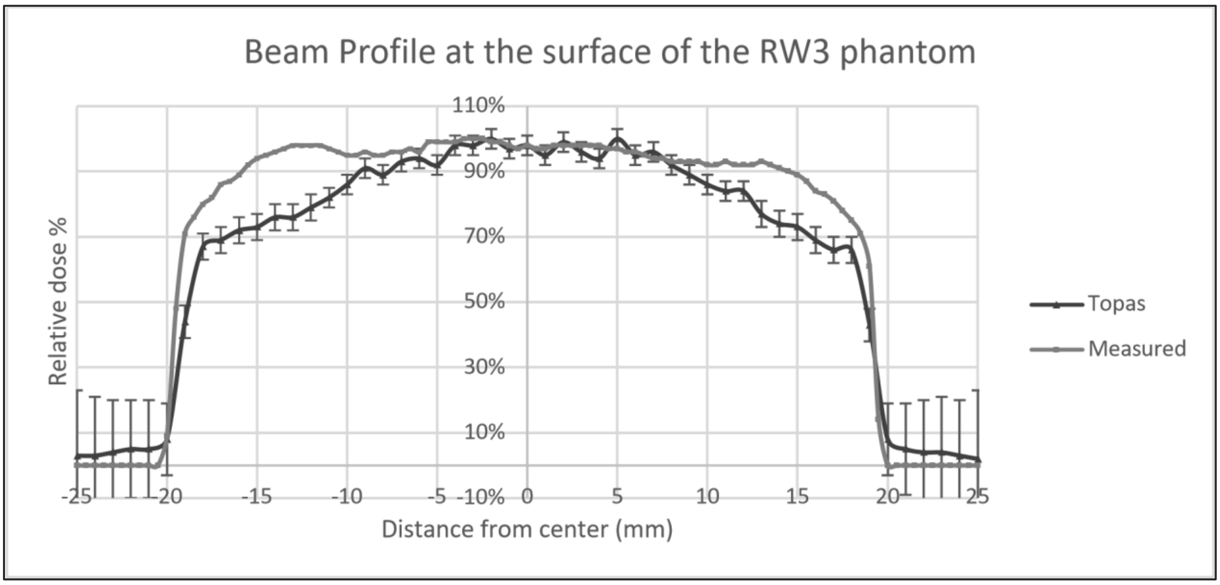

Figure 5: Measured and simulated transversal dose profiles recorded at the surface of the RW3 phantom [26, p. 72]

It was first concluded that the transverse profiles coincided within a few percent on and close to the beam's central axis. This was partly attributable to the normalisation carried out at the centre. Nevertheless, this aligned with the conclusions made earlier using the PDDs. On the other hand, significant discrepancies in dose at the edges of the profiles were recorded, revealing that the TOPAS MC model needed additional modifications.

1.3.2 Current objectives

As conveyed in 2.1, the Topas MC model ought to be adjusted to ensure that simulated transversal dose profiles generated by the Topas MC model are representative of transversal dose profiles measured using EBT3 films. Only when the model can generate both PDDs and transversal dose profiles that accurately represent their measured counterparts, it can be used to predict superficial radiotherapy treatments using the XOFT eBx System.

Consequently, this thesis's main goal is to optimize the current original Topas MC model to validate the model for the prediction of transversal dose profiles (1) in air, (2) on the surface of a Plastic Water LR phantom and (3) at 1 cm depth inside this phantom. The current hypothesis is that certain parameters of the electron beam in the simulation are simplified representations of how the electron beam behaves in the real x-ray tube. These parameters, pertaining to properties like the size, the shape and the spread of the electron beam, will hence be adapted until the final Topas MC model can produce simulated transversal dose profiles that are within 10% of measured transversal dose profiles using EBT3 films.

The second goal of this thesis aims to concretize the impact of the adaptation of each electron beam parameter on the associated simulated transversal dose profiles and to summarize these findings in a convenient table.

To make correct conclusions, the amount of initial histories simulated during each irradiation with the TOPAS MC model is adapted to guarantee an uncertainty less than 3% on the absorbed dose regarding the simulated transversal dose profiles produced using the TOPAS MC model.

2 X-ray tubes: functionality and physics

This chapter aims to provide just enough explanation to understand the functionality and the physics of the S700 x-ray tube used in the XOFT eBx System. Appendix A serves as an extension to this chapter and provides additional information.

2.1 Production & acceleration of electrons

The core idea of an x-ray tube is to produce x-ray photons by irradiating a (tungsten) target anode with electrons. These x-ray photons are subsequently used to irradiate the patient for diagnostic, or, in the case of the S700 source, radiotherapeutic purposes. Generally, these electrons are generated due to thermionic emission from a heated filament, which serves as the cathode in the x-ray tube [27]. Indeed, the filament is heated to very high temperatures (around 2000°C), thereby adding energy to the electrons through thermal excitation [27]. This results in some electrons overcoming their associated energetic barrier in the heated filament, and therefore freeing themselves from their host atoms, becoming so-called free electrons [27, 28]. This energetic barrier, defined as the work function, is strongly dependent on the filament material [27, 28]. After the electrons are removed from the heated filament, they are accelerated to the target anode by an electric field. Simultaneously, this beam of electrons is focused using a series of focusing electrodes.

2.2 Photon production in the target

After travelling through the x-ray tube from the filament cathode to the target anode, the electrons in the electron beam impinge on the target. While traversing the target, they may interact with orbital electrons and atomic nuclei [29]. Due to these coulomb interactions the incident electrons may scatter (elastic collision) or lose energy (inelastic collision). The total amount of energy deposited in the target per unit pathlength by an electron is defined as the electron stopping power of the target which will henceforth be truncated to stopping power. The total stopping power $\mathrm{S_{tot}}$ can be divided into 2 parts. The collision stopping power $\mathrm{S_{col}}$ governs energy losses correlated to coulomb interactions between the incident electron and orbital electrons resulting in ionization or excitation of the target atom. The radiative stopping power $\mathrm{S_{rad}}$ represents energy losses correlated to radiative interactions between the incident electron and the target nucleus [29]. The total stopping power can be calculated using formula 1. The minus signifies that the stopping power is relative to the energy deposited into the target along the track x and not relative to the kinetic energy $\mathrm{E_k}$ lost by the electron along the track x.

$$S_{tot} = -\langle\frac{dE_k}{dx}\rangle = S_{col} + S_{rad} \tag{1}$$

In practice the total stopping power is often replaced by the mass stopping power $\left(\frac{\mathrm{S}}{\rho}\right)_{\mathrm{tot}}$, which signifies the ratio of the total stopping power to the density ρ of the target [29]. The method used to calculate the mass stopping power is given in formula 2.

$$\left(\frac{S}{\rho}\right)_{tot} = \left(\frac{S}{\rho}\right)_{col} + \left(\frac{S}{\rho}\right)_{rad} \tag{2}$$

In reality, $\left(\frac{\mathrm{S}}{\rho}\right)_{\mathrm{tot}}$ governs all possible inelastic collisions of an electron in the target material. Out of all these possibilities, there are two main interactions which produce photons. The first type of photons are bremsstrahlung photons. These photons result from the negatively charged electrons emitting a photon with an energy equal to $\mathrm{h\nu}$ when they are decelerated and deflected by the positively charged force field of the target nucleus [29, 30]. This phenomenon is visualized in figure 6.

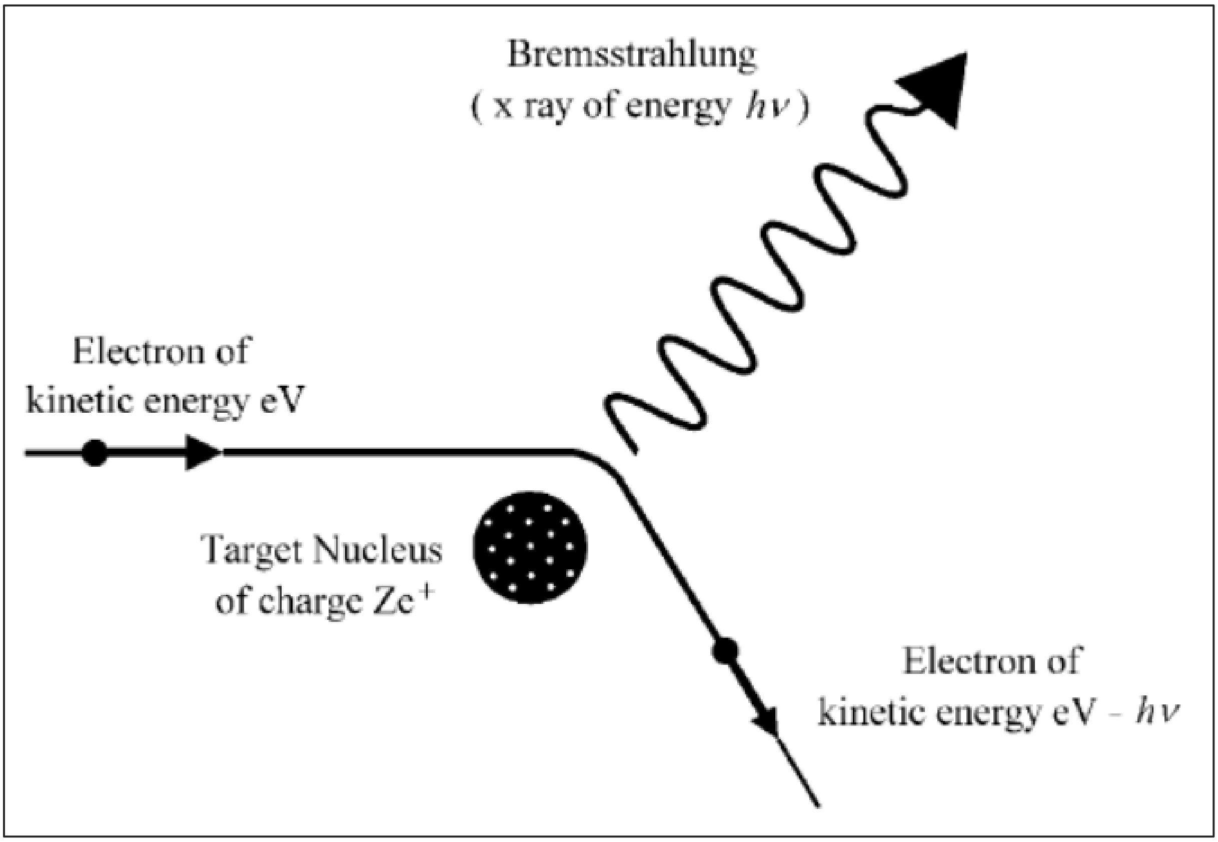

Figure 6: Production of a Bremsstrahlung photon [30, p. 92]

The energy of these photons is of continuous nature with energies ranging from zero up to the energy of the incident electron [29, 30]. The angular distribution of these photons depends on the kinetic energy of the incident electrons, which in turn is linearly proportional to the tube voltage V_t [27]. The angular distribution becomes more forward peaked when the kinetic energy of the incident electron increases as visualized in figure 7. The velocity of the incident electrons was given as a ratio to the speed of light in vacuum, represented by β.

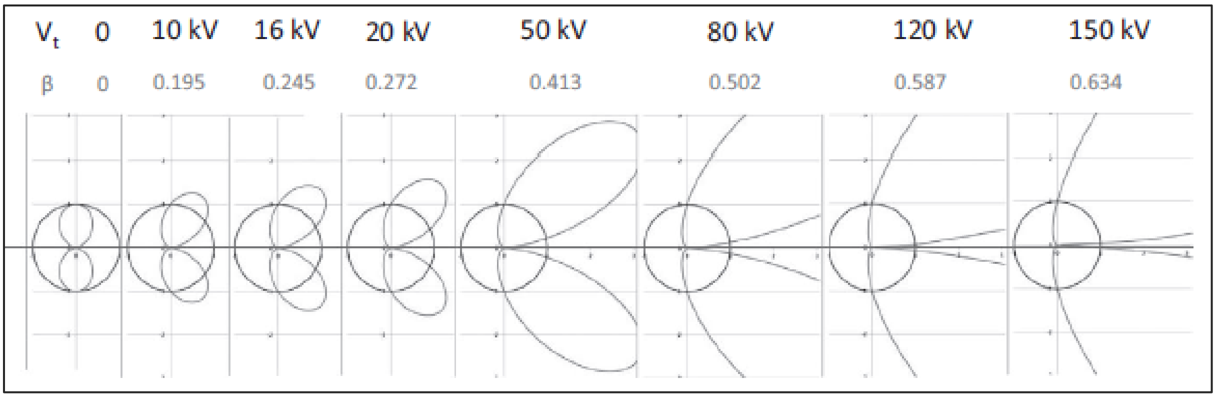

Figure 7: Angular distribution of electrons as a function of the kinetic energy of the incident electrons [27, p. 63]

Bremsstrahlung photons are accounted for in the mass stopping power equation by the mass radiative stopping power $\left(\frac{S}{\rho}\right)_{\mathrm{rad}}$.

The second type of photons are the characteristic photons [30]. They originate from hard collisions of incident electrons with orbital electrons. When an incident electron transfers more energy to an orbital electron than the binding energy of that orbital electron in the corresponding shell, the orbital electron will be ejected from the atom. Because electrons fill the lower energy levels first to minimize the atom's total energy, an electron from a higher energy level will jump down to fill in the vacancy. However, because the binding energy of the higher energy shell, from whence the electron came, is greater than the binding energy of the lower shell, this excess energy is radiated out of the atom by a photon. The term "characteristic photon" reflects the fact that the discrete energies of these photons are unique to the atom itself, providing information about the shell structure of the corresponding atom. Figure 8 illustrates the emission of such a characteristic x-ray photon.

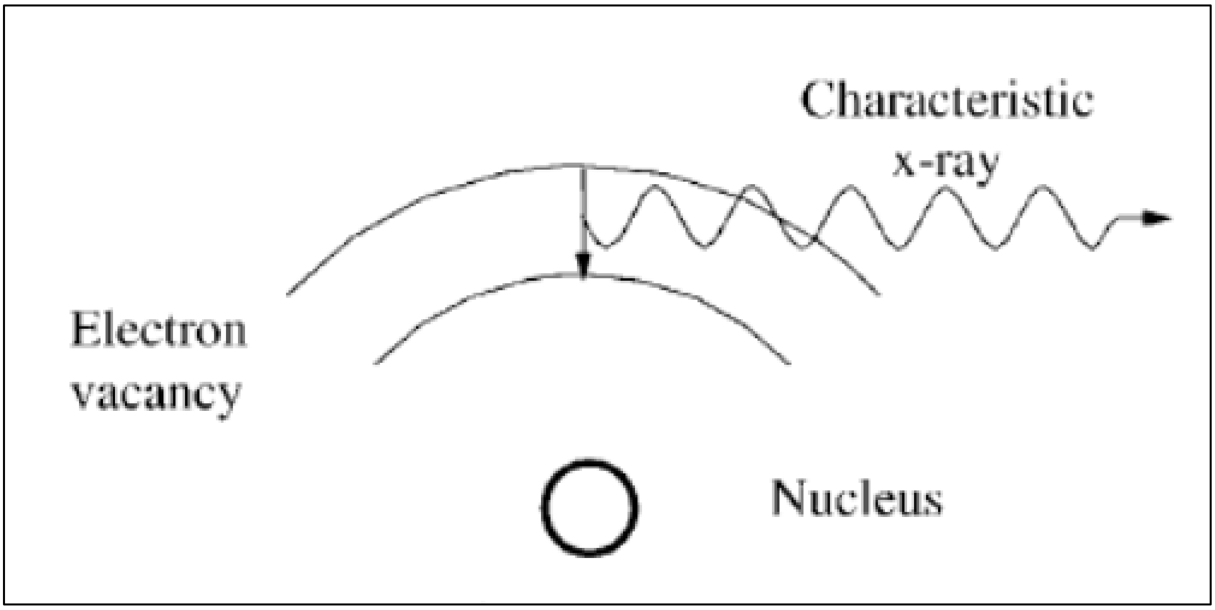

Figure 8: x-ray emission as a result of a vacancy in the upper shell [30, p. 93]

However, characteristic x-ray emission is not the only process that atoms can use to dispose of excess energy. Indeed, instead of the characteristic x-ray being emitted, it can interact with a higher energy electron upon which that electron is ejected from the atom. These ejected electrons are called Auger electrons. This process is visualized in figure 9.

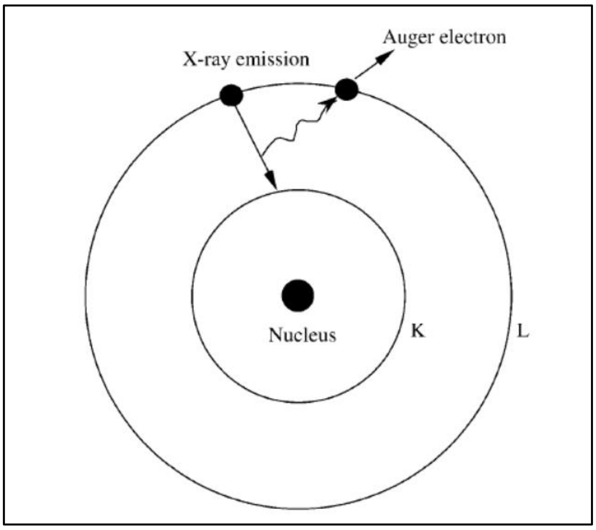

Figure 9: Ejection of an Auger electron from the atom [30, p. 97]

In practice, characteristic x-ray and auger electron emission compete to discard excess energy [30]. Figure 10 depicts the ratio η, which represents the ratio of characteristic X-ray emission to Auger electron emission, as a function of the atomic number Z of the target. It is apparent that x-ray emission grows in importance as Z increases. From Z ≈ 80 auger electron emission is negligible.

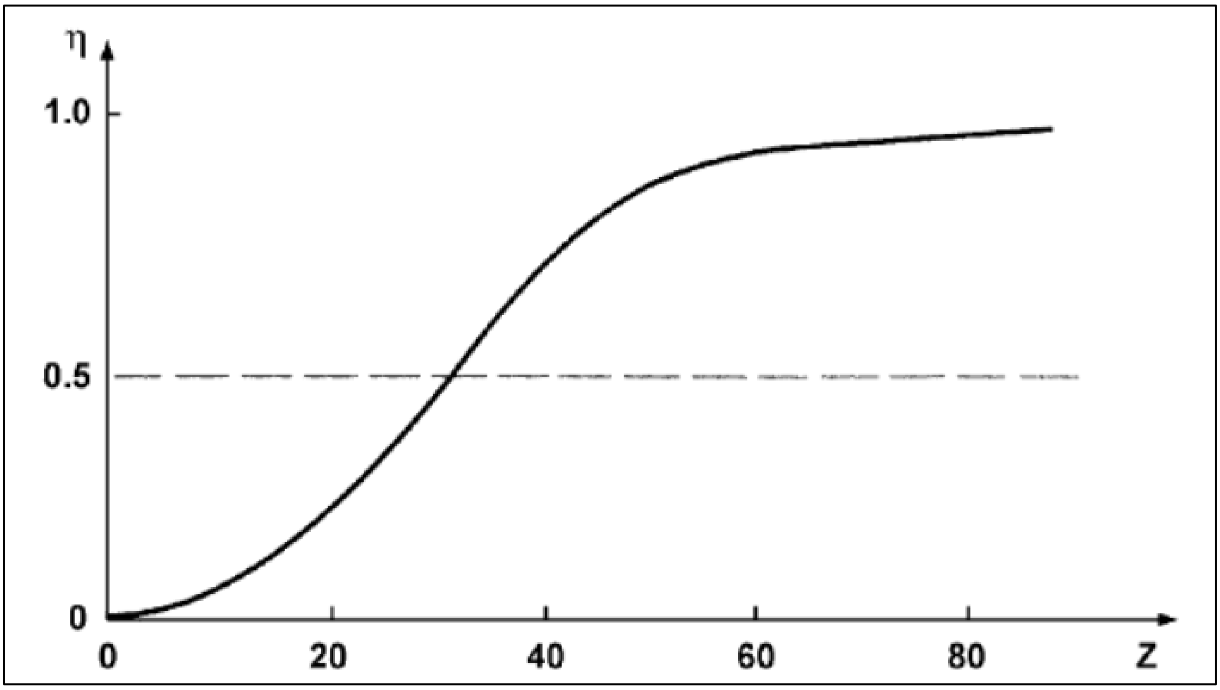

Figure 10: η as a function of the atomic number Z [30, p. 97]

Considering that some hard collisions induce the emission of characteristic x-rays, the importance of characteristic x-ray photons can be represented by the mass collisional stopping power $\left(\frac{S}{\rho}\right)_{\mathrm{col}}$.

Considering these two sources of photons, the resulting photon spectrum generated by an x-ray tube consists of (1) a continuous spectrum of bremsstrahlung, super positioned by (2) the discrete characteristic x-rays [30]. Logically, the material used to construct the target should be selected with the goal of maximizing the yield of these photon sources. As $\mathrm{S_{col}} \sim \mathrm{Z}$ and $\mathrm{S_{rad}} \sim \mathrm{Z}^2$, a high Z material is therefore desired [29]. However, even while using high Z materials, the photon production efficiency is very low. Indeed, most of the primary energy carried by the electrons impinging on the target is converted to heat, representing almost 60% of the initial amount of energy [27]. Using superficial and orthogonal x-rays, on average only 1% of the primary energy is converted into bremsstrahlung [27, 29]. Worse still, only about 0.1 % of the primary energy is converted to characteristic x-rays in Tungsten targets [27]. The remaining ~39% of primary energy is lost to backscattering electrons. As a result, Tungsten is often chosen as the target material as (1) it is a high Z material (Z=74) and (2) it is excellent for heat dissipation. This last statement is echoed by the fact that tungsten has highest melting point (3410 °C), greatest strength at high temperatures, and lowest thermal expansion of all known metals [31].

In addition to the material selection, the thickness of the target also has important implications on the resulting photon beam. How "thick" a target is deemed to be, is determined by comparing the thickness of this target to the range of the electrons in the target material R, which is calculated conform to formula 3. In this formula, $\mathrm{E_{ki}}$ signifies the initial kinetic energy of the considered electron [27].

$$R = \int_0^{E_{ki}} \left(\frac{S}{\rho}(E_k)\right)_{tot}^{-1} dE_k \tag{3}$$

Thick targets have a thickness in the order of R and are often called reflection targets because the majority of the x-rays are distributed orthogonally to the target [32]. These targets are often characterized by their excellent heat dissipation. Thin targets, with a thickness much lower than R (a few microns), are often called transmission targets as the majority of x-rays are produced through the target [32]. Compared to thick reflection targets they lack in heat dissipation, but produce a smaller focal spot size using similar power levels [32]. Due to the absence of the anode heel effect, transmission targets also enjoy greater symmetry on the associated transversal dose profiles and a steeper PDD curve compared to reflection targets, which limits the dose to healthy tissue nearby the tumour [33]. Due to the importance of these advantages when brachytherapy is considered, most EBT systems use a transmission type target. This group also includes the S700 source used in the XOFT eBx System. Figure 11 (a) and 11 (b) show x-ray distributions using a thick and thin target, respectively.

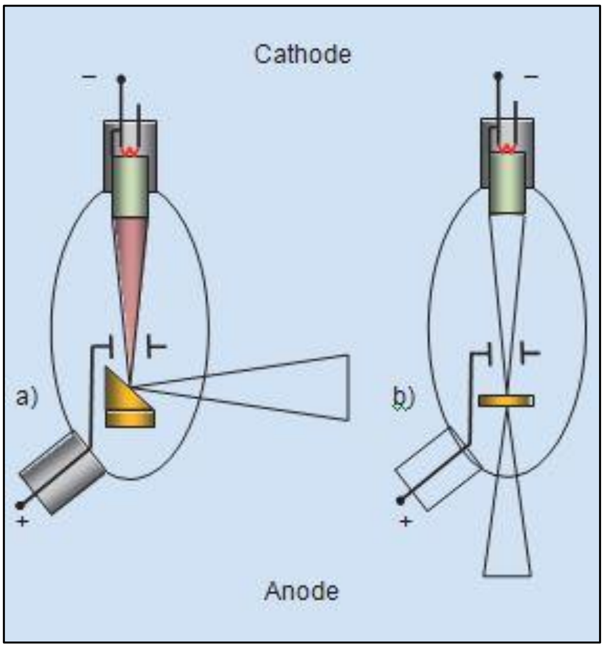

Figure 11: x-ray distribution using (a) a thick target and (b) a thin target [32]

2.3 Absorbed dose in the tumour

As mentioned in section 1.1, radiotherapy is used to damage the DNA of tumour cells, which impedes their functionality and multiplication. In particular, the S700 source inside the XOFT eBx System induces an absorbed dose in the tumour cells by irradiating them with x-ray photons. These photons can damage the DNA in these cells directly by ionising the associated atoms, or indirectly by creating reactive oxygen species (ROS). More detailed information about these mechanisms can be found in [30].

The most prevalent interactions of photons in matter are (1) the photoelectric effect, (2) Compton scattering and (3) pair production [29]. In the photoelectric effect, a photon interacts with a tightly bound orbital electron. Upon the interaction, the photon carries over all its energy to the orbital electron. The orbital electron is subsequently removed from the atom. The kinetic energy $\mathrm{E_K}$ of this ejected electron is the difference between the energy of the incident photon hv and the former binding energy $\mathrm{E_B}$ between the electron and the shell it formerly resided in [29]. This is embodied by formula 4.

$$E_K = hv - E_B \tag{4}$$

Figure 12 shows a photoelectric event in action. A photon interacts with an orbital electron of the K-shell, which ejects the electron out of the atom [27]. According to 3.3 an electron strives to configure its electrons in the most energy-efficient manner. Therefore an L shell electron falls down to the K shell to fill the vacancy. The excess energy is radiated outwards via K_α x-ray emission or by emission of auger electrons.

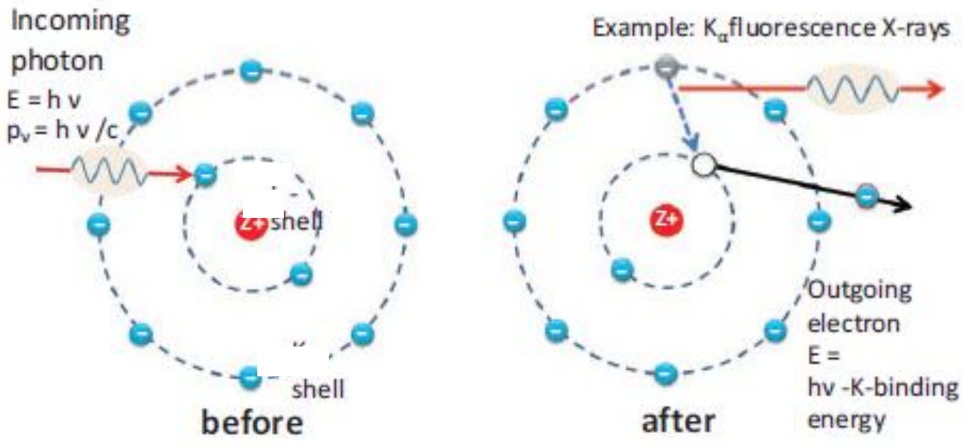

Figure 12: photoelectric effect on a K-shell electron [27, p. 101]

The photoelectric effect is subject to the proportionalities conveyed by formula 5 and 6. τ_m is the mass attenuation coefficient for the photoelectric effect and $_\mathrm{a}\tau$ is the atomic attenuation coefficient for the photoelectric effect [29]. Attenuation coefficients govern the proclivity of a photon to interact in a certain material.

$$\tau_m \sim \left(\frac{Z}{hv}\right)^3 \tag{5}$$

$$_a\tau \sim \frac{Z^4}{(hv)^3} \tag{6}$$

Compton scattering differs with the photoelectric effect in the sense that the incident photon does not disappear after interacting with an orbital electron [29]. Indeed, the photon transfers part of its energy to the electron resulting in an electron being ejected out of the atom parallel to the incident photon being scattered with a lower energy. This interaction considers the orbital electron to be free and stationary and the electron's binding energy is therefore negligible. Given that the amount of energy remaining for the photon after the interaction is equal to hv', then the kinetic energy of the electron is the energy of the incident photon hv reduced by hv' [29]. Figure 13 gives a schematic representation of Compton scattering.

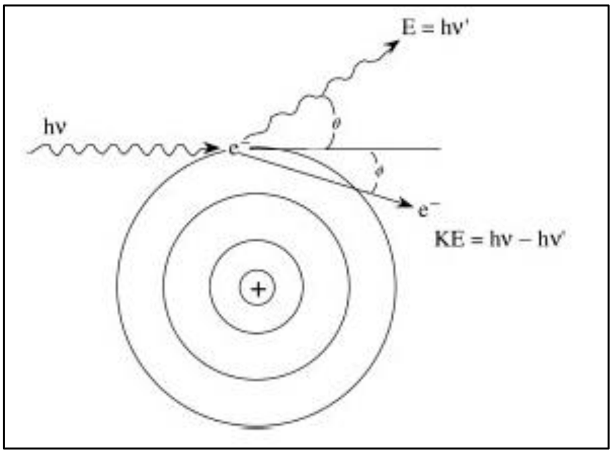

Figure 13: Compton scattering [30, p. 273]

For Compton scattering, the electronic- and mass attenuation coefficient are independent of Z [29]. On the other hand, the atomic Compton attenuation coefficient ${}_{a}\sigma_{C}$ is linearly proportional to the atomic number Z.

The last photon interaction process covered in this thesis is pair production. In pair production, a high-energy photon is converted into an electron-positron pair in the strong electro-magnetic field of a nucleus [29]. This process is visualised in figure 14.

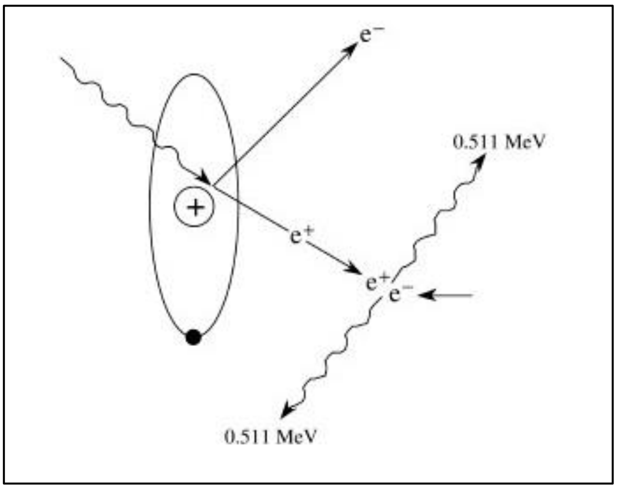

Figure 14: pair production [30, p. 275]

Considering that both fermions have a rest mass of 511 keV, the initial photon has to have a minimal energy of 1022 keV for pair production to occur. Acknowledging the fact that even in an extreme case the photons produced by x-ray tubes in EBT have an energy of 100 keV, pair production is not relevant for this thesis.

In conclusion, the probability for a photon to undergo a certain type of interaction depends on the energy of the photon $h\nu$ and the atomic number Z [29]. As depicted in figure 15, the photoelectric effect dominates at low energies while Compton scattering is especially relevant for intermediate energies. Finally, high energies are dominated by pair production. The red line shows the maximal possible energy of a photon created by the S700 source. Based on this, most photon interactions in the skin lesions will be accounted for by the photoelectric effect totalled with a small amount of Compton scattering.

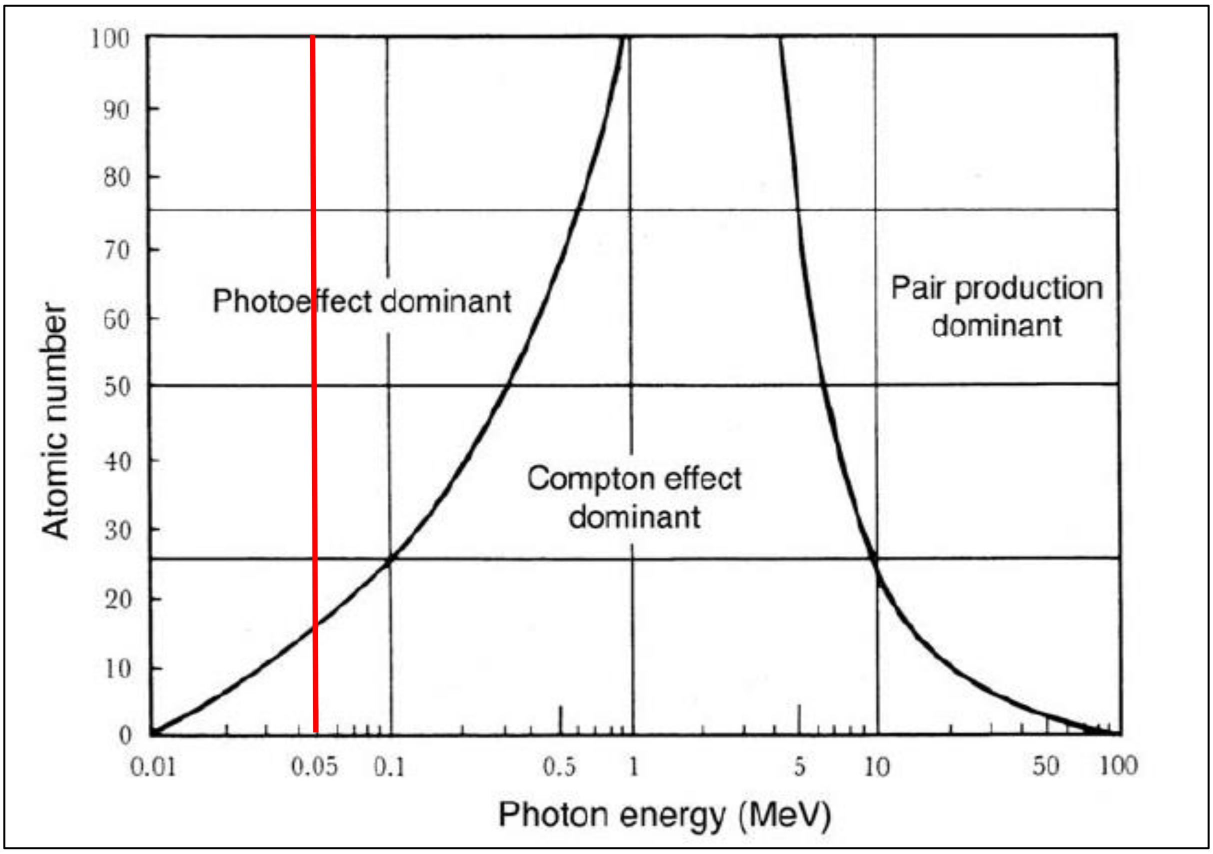

Figure 15: Regions of relative predominance of photon interactions in matter [29, p. 37]

3 XOFT eBx System

As discussed earlier in section 1.2.2, electronic brachytherapy systems, like the XOFT eBx System, use a miniaturized radiotherapeutic x-ray source to deliver a highly localized dose deposition inside the patient and are therefore ideal for treatment of (NMSC-related) skin lesions. This chapter is specifically dedicated to this system. To begin, section 3.1 lists (1) the most important components and their structure and (2) specifications pertaining to the XOFT EBX System. Then, section 3.2 continues with the applied dosimetry protocol, which is typically used to calculate the dose administered in the patient after an irradiation using the XOFT eBx System. To conclude this chapter, section 3.3 lists typical photon spectra associated with the XOFT eBx System.

3.1 Components and specifications

The XOFT eBx System designed by XOFT, inc. uses the accompanying S700 miniature x-ray source to deliver an adaptive dose to the patient. The diameter of this 10 mm long source equals 2.25 mm, surrounded by a catheter of 5.6 mm [34, 35, 36]. In this catheter a specialized perfluoropolyether heat transfer fluid (Galden HT 135) is pumped by a peristaltic pump to dissipate the heat created in the tungsten target. This allows users to achieve higher dose rates without damaging the surrounding structures or the source [34]. The tungsten transmission type target is lined inside the Aluminium-Nitride tip using an Yttrium binding [18, 34]. The electrons, impinging on this target, are created due to thermionic emission from a heated filament. Figure 16 shows the S700 source and its internal structure using a longitudinal cross section. Additionally, figure 17 displays a simplified model of the S700 source in the catheter, while figure 18 shows a screenshot of a Standard Tessellation Language (STL) file of the tip courtesy of XOFT, inc.

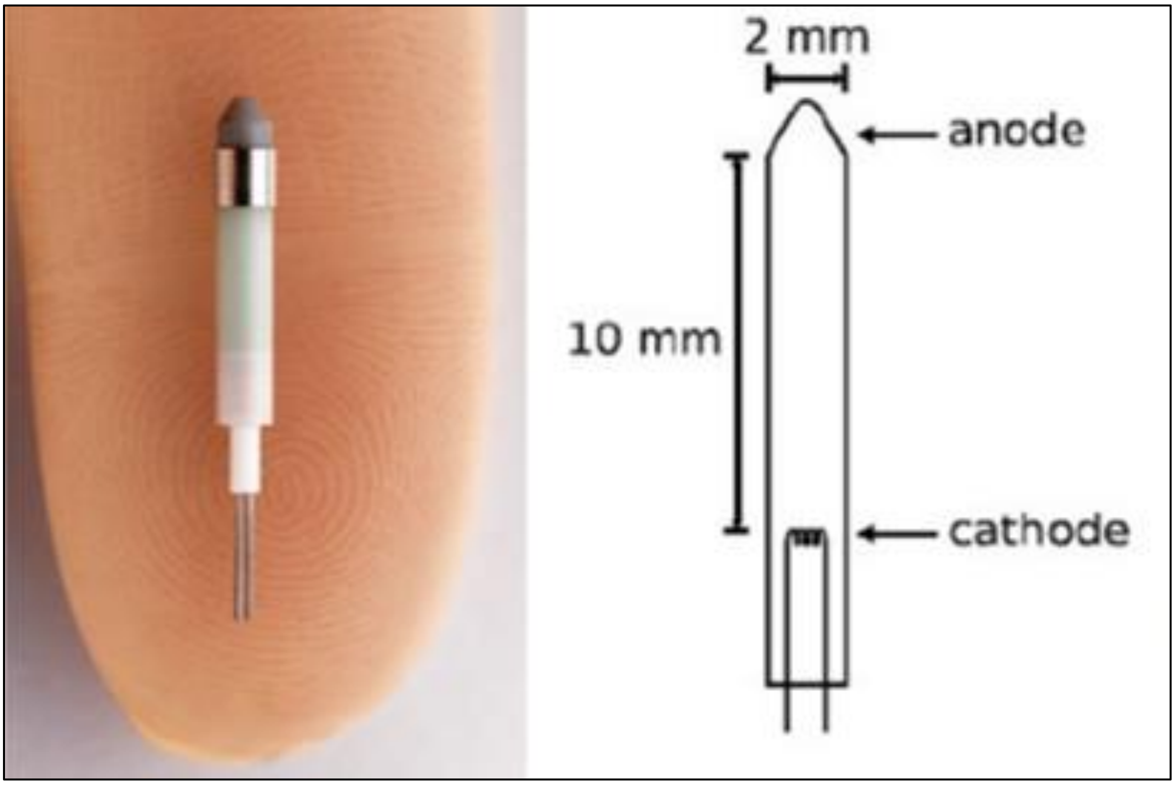

Figure 16: The S700 source on a human finger (left) and its internal structure (right), dimensions are approximations [36, p. 955]

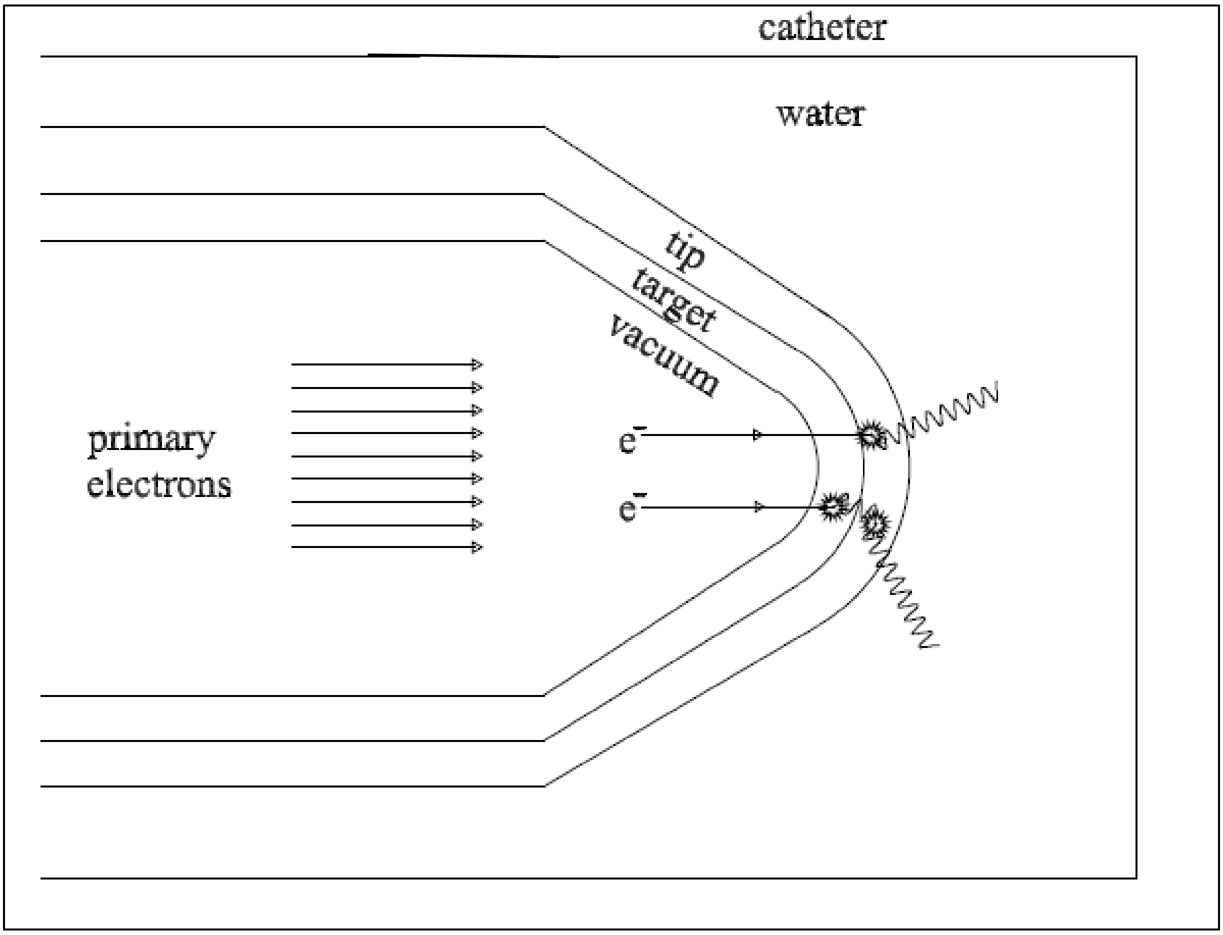

Figure 17: simplified representation of the S700 source tip in the catheter [18, p.38]

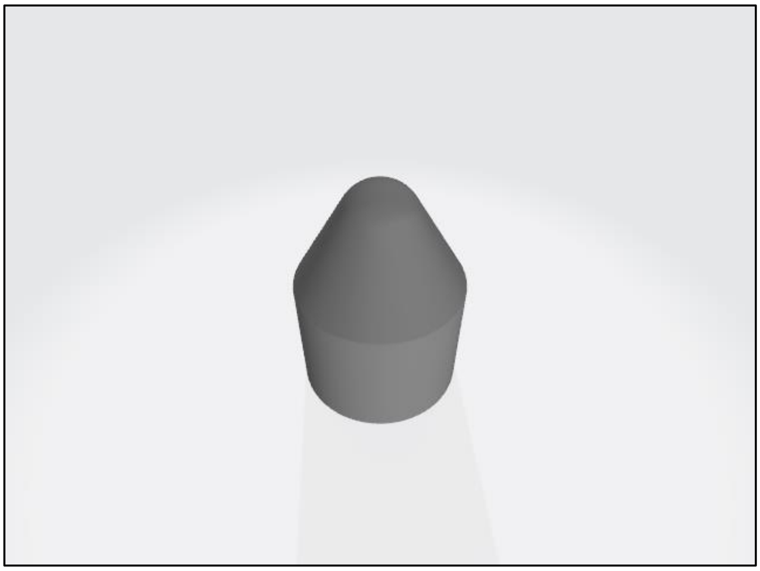

Figure 18: tip of the S700 source consisting of an Aluminium-Nitride alloy

Zooming out, figure 19 and figure 20 show the S700 x-ray source connected to the power supply of the XOFT treatment unit by a duet consisting of an HV cable and a HV connector. Additionally, figure 21 shows the treatment unit and the coolant bag connected to the coolant inlet/outlet.

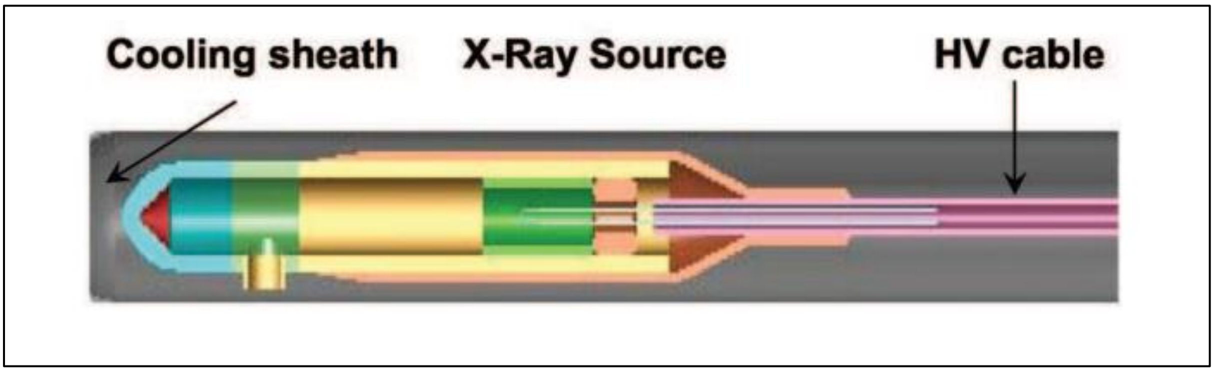

Figure 19: The S700 source, surrounded by the catheter (which is also referred to as the cooling sheath in literature), is connected to the HV cable [34, p. 4021]

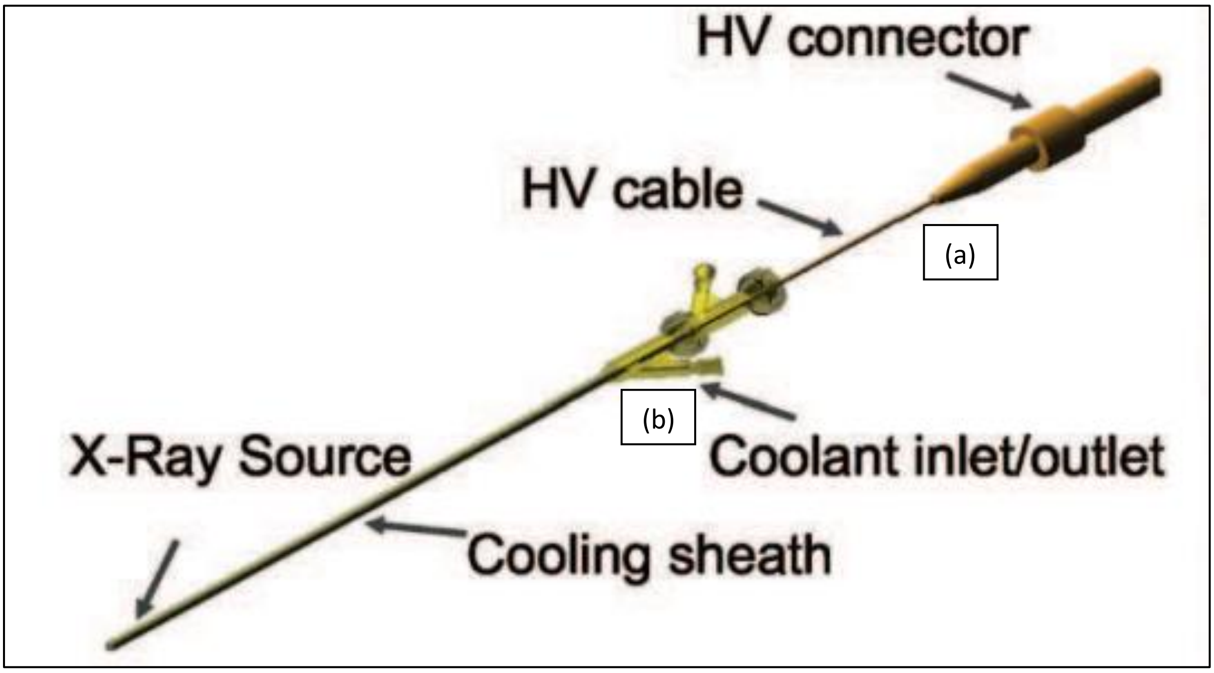

Figure 20: (a) the HV connector attaches the HV cable to the power supply of the treatment unit and (b) the coolant inlet/outlet are connected to the coolant bag [34, p. 4021]

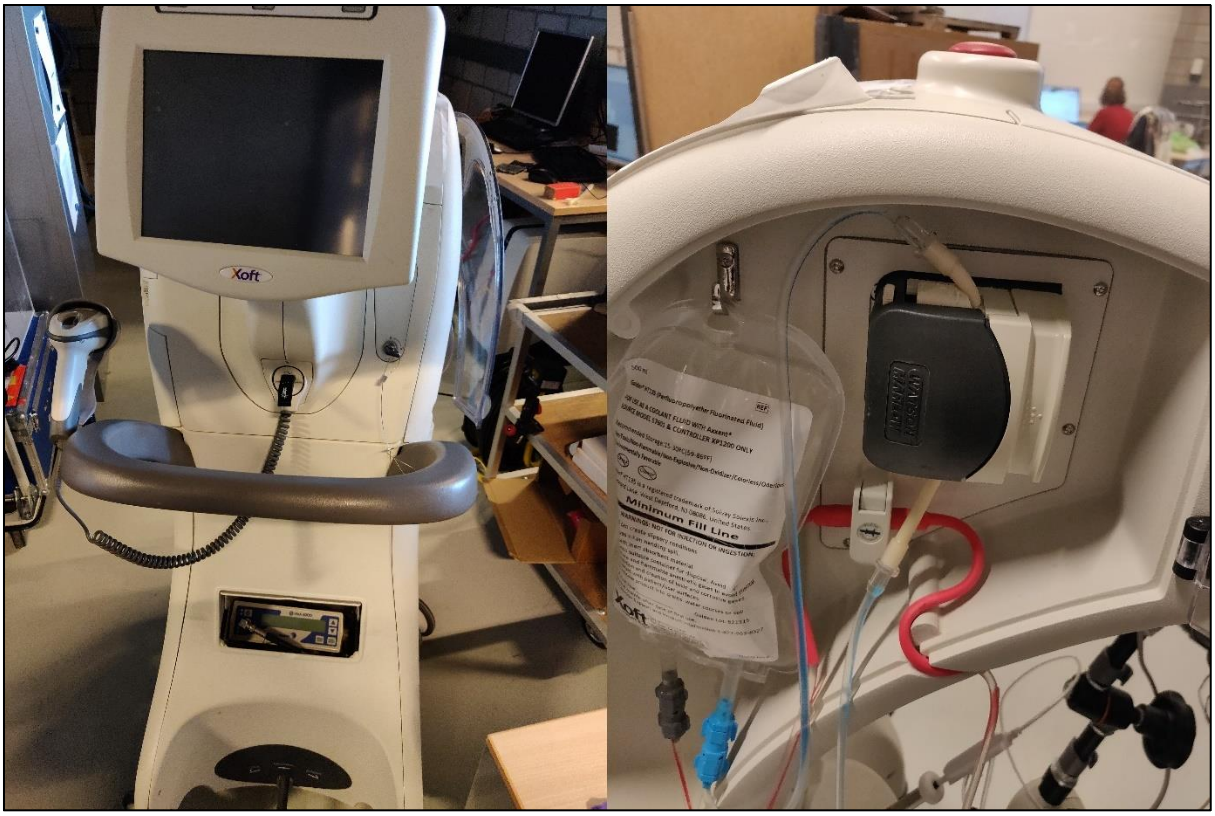

Figure 21: The XOFT accent treatment unit (left) and the associated cooling bag connected to the coolant inlet/outlet (right)

The XOFT eBx System can be equipped with several site-specific applicators to obtain maximal dose conformality [36]. As such, conical applicators with a diameter ranging from 10-50 mm are commercially available to treat small and large skin lesions. These applicators are all equipped with a polycarbonate disc at the base of the cone to ensure a flat contact with the patient’s skin [34]. The associated S700 source ought to be positioned at the end of the source channel at the cone's apex. Furthermore, each of these applicators is fitted with an aluminium-based flattening filter, wrapping itself around the source [36]. This flattening filter is designed to deliver a uniform dose to the skin of the patient and is unique to the diameter of the applicator. Finally, the Touhy-Borst adapter attached to the cone ensures that the S700 source stays in place during the treatment [36]. Figure 22 shows the 35 mm applicator used in this thesis. Figure 23 shows the model of the flattening filter used in the 35 mm applicator.

Figure 22: XOFT Accent skin applicator (35 mm)

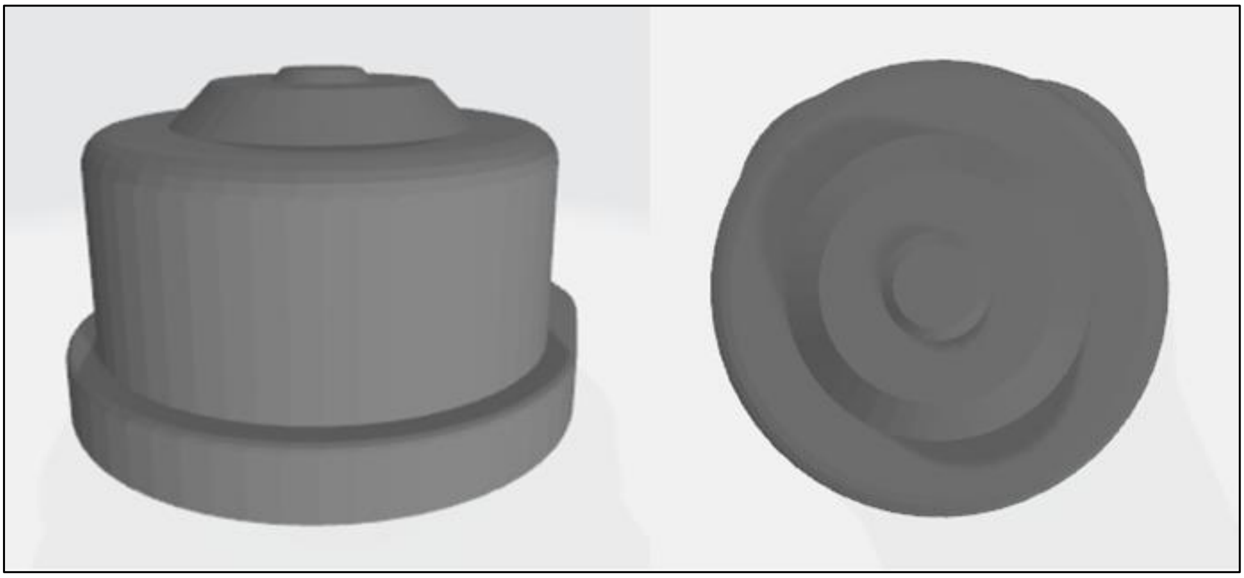

Figure 23: Aluminium flattening filter used in the 35 mm applicator: more material in the middle flattens the beam

Operating at a tube voltage of 50 kV and a tube current of 300 μA, the S700 source generates an air-kerma strength of 1400 $\frac{\mathrm{Gy*cm^2}}{\mathrm{h}}$ [34]. Although this is a high dose rate, shielding concerns that often arise when discussing conventional HDR brachytherapy are limited, considering that the S700 source produces photons with an energy $\leq 50\ \mathrm{keV}$ [34]. Indeed, section 2.3 explained that these low-energy photons are more likely to interact in matter, making it easier to shield the physician from said photons. Lastly, treatments using the XOFT eBx System have been recorded to depict rapid dose drop offs comparable to LDR I-125 treatments [34].

3.2 Dosimetry

Historically, permanent low dose rate brachytherapy sources were characterized by the TG-43 formalism to define the dose rate for a cylindrically symmetric, photon emitting, brachytherapy source [26, 34]. This demographic was later extended to the S700 source by [34]. However, it would be incorrect to characterise the dose output of the S700 source for the treatment of skin lesions by using TG-43. Indeed, contrary to seeds in permanent brachytherapy, the S700 source is not placed in the patient's body for this application. As mentioned in section 3.1, the source is instead located at the apex of the conical applicator. A better option for the dose characterisation of the S700 source is the TG-61 formalism for 40 – 300 kVp x-ray dosimetry [37]. The TG-61 formalism comprises 2 available methods including the in-air method for low- and medium-energy x-rays and the in-phantom method for medium-energy x-rays [26]. For the 50 kVp S700 source, XOFT, inc. uses an adapted TG-61 formalism where the air kerma is determined using a free-in-air measurement and a backscatter factor is applied to account for the effect of phantom scatter [37]. When using this method, the surface of the phantom is regarded as the point of reference for all calculations and measurements. Formula 7 describes the relationship between the dose to water at that reference point $\mathrm{D_{w,z=0}}$ and the corrected well chamber measurement M (charge) obtained at that reference point [26, 37]. A well chamber is a type of ionisation chamber designed with a central cavity, in which the S700 source is placed. More information on ionisation chambers is available in appendix C.

$$D_{w,z=0} = M * \; N_K * B_W * P_{stem,air} * \left[\left(\frac{\bar{\mu}_{en}}{\rho}\right)^{w}_{air}\right]_{air} \tag{7}$$

In formula 7, $\mathrm{N_K}$ is the Accredited Dosimetry Calibration Laboratory (ADCL) air kerma calibration factor, which relates the chamber measurement M to an equivalent air kerma. Furthermore, $\mathrm{B_W}$ is the backscatter factor accounting for backscattering due to the phantom, $\mathrm{P_{stem,air}}$ is the chamber stem correction factor and finally $\left[\left(\frac{\bar{\mu}_{\mathrm{en}}}{\rho}\right)^{\mathrm{w}}_{\mathrm{air}}\right]_{\mathrm{air}}$ is the ratio of water to air of the mean mass-energy absorption coefficients averaged over the photon spectrum of the x-ray source [37]. The corrected well chamber measurement M is derived using formula 8.

$$M = \; M_{raw} * P_{TP} * P_{ion} * P_{pol} * P_{elec} \tag{8}$$

In formula 8, $\mathrm{M_{raw}}$ represents the uncorrected charge created in the well chamber, $\mathrm{P_{TP}}$ is the correction factor accounting for a deviation of the pressure and/or temperature from the norm of 760 mmHg and 22 °C, $\mathrm{P_{ion}}$ is the correction factor accounting for ion recombination, $\mathrm{P_{pol}}$ is the correction factor accounting for the polarity effect and finally $\mathrm{P_{elec}}$ is the correction factor which is used when the electrometer is calibrated separately from the well chamber [37]. Finally, the dose rate $\mathrm{\dot{D}_{w,z=0}}$ at the reference point can be calculated using formula 9.

$$\dot{\mathrm{D}}_{\mathrm{w,z=0}} = \frac{D_{w,z=0}}{T + \delta t} \tag{9}$$

In formula 9, T is the exposure time, while δt accounts for the end effect. This effect accounts for the extra dose delivered prior to the start of the timer, which is induced during the ramp up.

3.3 Typical photon spectra

[18] recorded and listed typical photon spectra of the associated S700 source at 40 kVp and 50 kVp using an Amptek XR-100T cadmium telluride spectrometer. The results are visualized in figure 24.

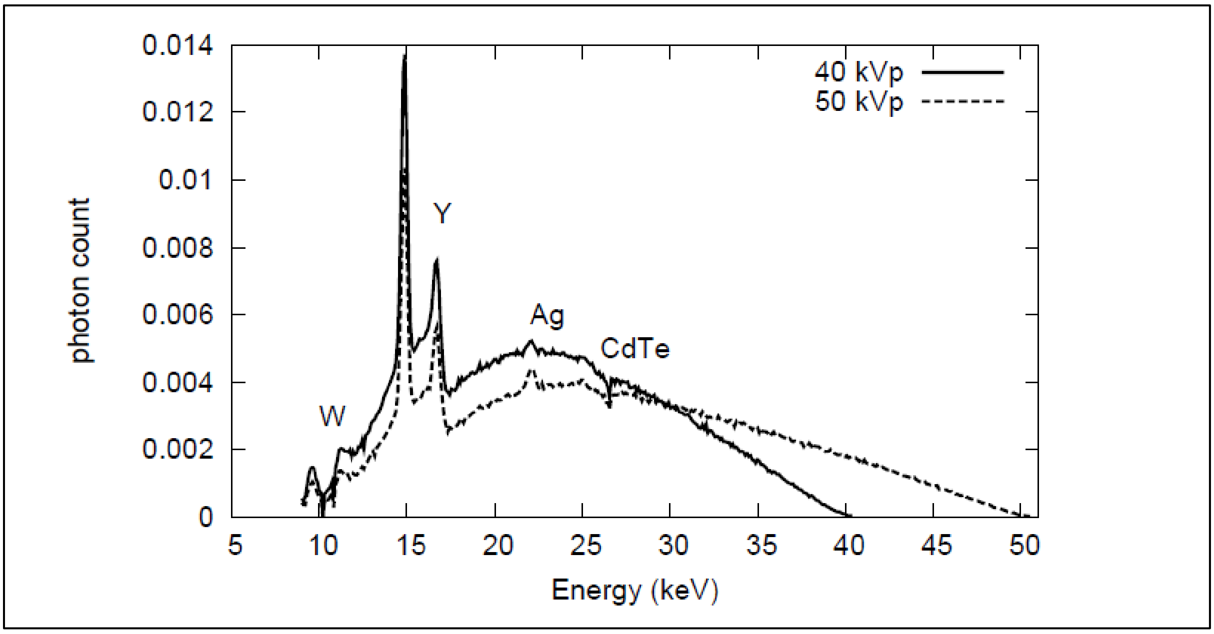

Figure 24: Photon spectra measured at 40 kVp and 50 kVp using an Amptek XR-100T cadmium telluride spectrometer

Tungsten L characteristic X-rays were observed at 9.7 and 11.3 keV while Yttrium K characteristic x-rays were measured at 14.9 and 16.7 keV [18]. Furthermore, a characteristic K x-ray peak of 22 keV attributable to silver (which is a constituent in the brazing alloys) was located at 22 keV. Even though the spectrometer was corrected for detector response, the photo-escape edge artifact resulting from the cadmium telluride spectrometer was recorded at 26.5 keV.

It was concluded that 87% of the photons were created in the Tungsten target and that 7 % of the photons originated from primary electrons interacting in the Yttrium tip [18]. Also, 1 % of the photons resulted from primary electrons interacting in other parts of the x-ray tube. The remaining 5 % of photons could be attributed mainly to characteristic Yttrium x-ray photons created in a two-part phenomenon. In this phenomenon, photons generated by primary electrons impinging on the target interacted in the Yttrium tip. Due to the vacancies created by the photoelectric effect, characteristic Yttrium photons were finally detected [18].

4 Dose output evaluation

To evaluate the dose output of teletherapy and brachytherapy treatments, the PDD and transversal dose profiles are often measured and compared to simulated results and other radiotherapy techniques. For the XOFT eBx System to be deemed eligible to treat skin lesions, the PDD and the transversal dose profiles need to be measured and compared to simulated results in relevant situations. Considering that the particle beam is concurrent to the z-axis, the PDD evaluates the dose along this same z-axis. In contrast, transversal dose profiles evaluate the dose perpendicularly to the beam, i.e. the x- and y-axis.

4.1 PDD

As mentioned in section 1.3.1, previous theses already succeeded in creating the original TOPAS MC model which was validated for the prediction of PDD measurements pertaining to the XOFT eBx System. Consequently, this section solely provides some basic information about PDD curves. No further PDD measurements were carried out in this thesis.

The PDD curve provides information about the relationship between the dose and its associated depth in a specific phantom. The curve of the PDD therefore is therefore a plot of the normalized dose measured in a phantom along the beam and the corresponding depth inside the phantom. The aforementioned normalization is calculated relative to the maximal dose measured in that same phantom. The PDD is dependent on (1) the field size, (2) the evaluated depth, (3) the SSD and finally (4) the photon energy hv, considering that section 2.3 explained that the likelihood of interaction is inversely proportional to hv. The PDD curves, pertaining to the XOFT eBx System, measured in RW3 and Plastic Water LR, can be found in figure 3 and figure 4.

4.2 Transversal dose profiles

The focus of this thesis is directed at the second type of dose evaluation, which are transversal dose profiles. Transversal dose profiles provide information about the expected transversal dose drop off when measuring at a certain distance away from the beam axis. Indeed, transversal dose profiles plot the normalized dose to the corresponding distance away from the beam axis which is usually calculated relative to the dose measured on the beam axis. The distance is generally also normalized relative to the position of the beam. These transversal dose profiles can be evaluated at the surface of a phantom, but also at a certain depth inside a phantom. [26] evaluated simulated transversal dose profiles using the XOFT eBx System which were generated using the original TOPAS MC model. This simulation was carried out on the surface of a plastic water LR phantom. To compare the resulting simulated transversal dose profile to a “real” transversal dose profile pertaining to the XOFT eBx System, transversal dose profiles were measured on the same plastic water LR phantom. For this purpose, EBT3 film dosimetry was utilised. The results were displayed earlier in section 1.3.1, more specifically in figure 5.

5 Film dosimetry

Radiographic films based on silver halide emulsions have been used worldwide for decades as a powerful 2D dosimetry tool for treatment planning and quality assurance [38]. These films have a total thickness of about 0.25 mm, with the active measuring emulsion layer only accounting for a few micrometres in this equation. Therefore, these films are regarded as (one of) the only “real” 2D dosimeters for point measurements [39]. Indeed, compared to competitors like small ion chambers and silicon diodes, films exhibit superior spatial resolution [39]. This makes film dosimetry especially interesting for the acquisition of transversal dose profiles, where it is imperative that the dose is evaluated at the same depth in a phantom as they can easily be inserted into the phantom at the desired depth. In addition, radiographic films are known for their ruggedness and permanent recording of irradiation [38]. Consequently, these radiographic films like EDR2 and XV2 were often used to determine transversal dose profiles to verify IMRT plans [39].

Despite these advantages, radiographic films have decreased in popularity in recent years. This is mainly due to the invention of superior radiochromic films who retain the previously mentioned advantages of radiographic films but mostly eliminate known disadvantages like the need for chemical processing, large energy dependence at lower photon energies, sensitivity to light and temperature and non-tissue equivalence [38, 39]. After irradiating a radiochromic film, the crystalline diacetylenes in the sensitive layer become polymerized [40]. Finally, the irradiated area turns blue or red (depending on the composition of the particular diacetylenes) which can be detected by graphical scanners [40]. The discoloration of the radiochromic film at a specific location is then quantified as a corresponding optical density (OD) which in turn is finally converted into a measured absorbed dose using the calibration curve which links the OD and the associated absorbed dose received by the radiochromic film during the irradiation. This process is further discussed in section 7.1.2.

The GAFchromic™ EBT film was initially produced to replace radiographic films for quality assurance regarding IMRT treatments and belongs to the aforementioned category of radiochromic films [39]. Since then, they have found multiple applications in radiotherapy, including characterization of proton beams, skin dose measurements and brachytherapy [39]. Although several models are available they all share the same internal materials in different configurations. The specific diacetylene in these radiochromic films is the lithium salt pentacosa-10,12-diyonic acid (LiPCDA) [40]. As these crystals are too big to provide useful sensitivity they are first dissolved in a solvent. After dispersing these crystals in an aqueous gelatine solution (functioning as a binder), this active layer is sandwiched between passive substate materials to safeguard the active layer. The orientation of the crystals is then finally fixed upon drying [40]. In most cases, polyester is the substrate material of choice. The design of the EBT3 film is shown in figure 25. In this particular case, the active layer of 26 µm is sandwiched between the passive polyester layers of 125 µm [38]. The EBT3 model is suitable for a dose range of 0.01 – 30 Gy.

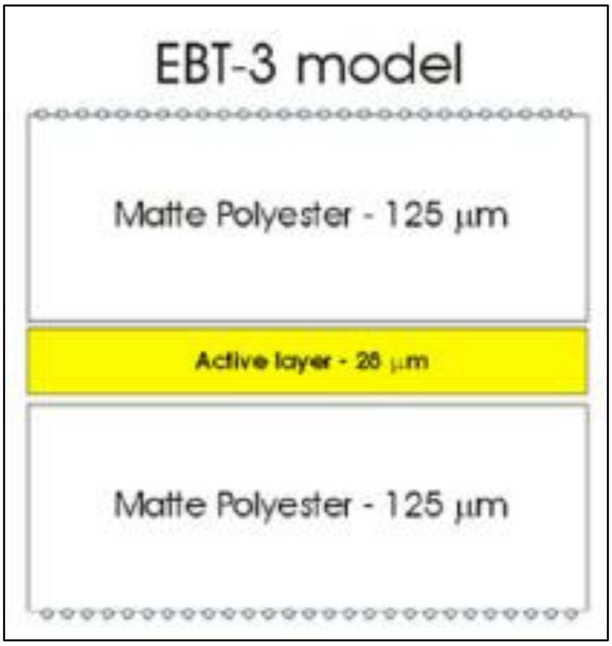

Figure 25: diagram of the GAFchromic EBT3 film [38, p. 2]

Due to the aforementioned advantages and the suitable dose range, EBT3 films, in particular, are the ideal candidate for the measurement of transversal dose profiles pertaining to the XOFT eBx System.

6 Monte Carlo

Monte Carlo simulations can be used to simulate real-life treatments without exposing the patient to the risks that accompany radiation exposure. Consequently, Monte Carlo simulations are extensively used by physicians all around the world for treatment planning and quality assurance. For this thesis in particular, it can be used to (1) simulate irradiations using the XOFT eBx System and (2) produce the associated simulated transversal dose profiles.

6.1 Geant4

Geant4 is a Monte Carlo transport program developed and released in the 1990s by CERN and other collaborators [41]. It was the product of the RD44 program in which 100 scientists and engineers gathered valuable information by conducting multiple independent experiments [40]. The product was an object-oriented Monte Carlo program coded in C++ [41, 42]. Compared to MC codes with similar accuracy like FLUKA and MCMPX, Geant4 offers a higher level of geometrical complexity which is ideal to model the intricate design of the S700 source [42]. Additionally, it openly conveys the physics used for particle transport which can easily be adapted for a range of different applications by virtue of the open-source nature of Geant4 [41].

The three electromagnetic physics models used to govern interactions of electrons and photons are G4 Standard, G4 LowEnergy and G4 Penelope [43]. G4 Standard is the default option as Geant4 was initially designed for high-energy detector simulations [41, 43]. G4 Standard uses simple transport algorithms and is therefore the fastest model. It is applicable to energies ranging from 1 keV to 100 TeV, although it is mainly appropriate for use at higher energies. G4 LowEnergy is suitable for very low energies with a lower bound of 250 eV [43]. Lastly, the G4 Penelope model is based on the MC code Penelope which offers more accurate simulations as atomic relaxation is accounted for [42]. For low energy electrons (typical in EBT), literature seems to agree that G4 Standard is not sufficiently accurate for medical applications [43, 44]. The choice between using G4 LowEnergy and G4 Penelope is more cumbersome as they display similar results. However, [44] noted a slightly more accurate bremsstrahlung production using G4 Penelope compared to G4 LowEnergy. Due to the importance of bremsstrahlung production for low energy electron beams, G4 Penelope is most appropriate for the MC model of the XOFT eBx System.

6.2 TOPAS

The flexibility of Geant4 is the main reason for its popularity with physicists and engineers around the world. However, users perceive this flexibility as a double-edged sword as the code has a very steep learning curve [42]. Consequently, it takes a long time for beginners to correctly use Geant4 for medical physics applications, and even then, there is a significant risk of user-related errors [42]. In the early

2000s, Geant4 was therefore relatively underutilized in medical physics as only a select few research groups with adequate knowledge used this Monte Carlo program.

In 2012, this completely changed with the release of the TOPAS MC tool. The term "tool" refers to the fact that TOPAS is not a Monte Carlo code per se. Rather, TOPAS is a user-friendly extension and enhancement of the MC code Geant4 [42]. As such, it utilizes the full capabilities of Geant4, but it only selects certain default parameters, functions and physics modules which are most appropriate for applications in medical physics [42]. Nevertheless, TOPAS maintains the flexibility of Geant4 in the sense that these default settings may be adjusted, and personal extensions may be added in C++ code. TOPAS was originally created to boost the use of Monte Carlo in proton therapy [42]. Nowadays, TOPAS has been updated on a regular basis to support radiobiology modelling as well as simulations using electron- and photon beams [45].

7 Materials & Methods

7.1 Measuring transversal dose profiles using EBT3 films

7.1.1 Experimental setups

Three different setups were considered using the XOFT eBx System equipped with the S/N 960251 S700 source and the 35 mm conical applicator. This source was operated with a tube voltage of 50 kVp and a tube current of 300 µA. Due to insufficient uniformity of this source, this source was deemed to be non-clinical by XOFT, inc. The purpose of the first setup was to measure transversal dose profiles in air. Consequently, the applicator was placed in contact with the EBT3 film held in place by a wooden frame. The second setup aimed to decipher the impact of backscatter on the measurements of dose profiles. As such, a 4cm thick Plastic Water LR phantom was placed behind the EBT3 film which simulated the irradiation of superficial skin lesion as the tissues, muscles and bone behind the skin would induce backscattering of photons into the skin layers. The third and last setup aimed to simulate the irradiation at 1 cm depth inside the same Plastic Water LR phantom, with 3 cm of Plastic Water LR behind the EBT3 film. This would represent the irradiation of skin lesions expanding into deeper layers of the skin and surrounding tissue. Figure 26 shows these experimental setups.

Figure 26: Experimental setups with measurements in air (left), on the surface of a 4 cm Plastic Water LR phantom (middle) and at 1 cm depth inside this phantom(right)

In actuality, the Plastic Water LR phantom was comprised of 4 separate slabs of Plastic Water LR, each with dimensions of 10x10x1 cm, which allowed the dose measurement at 1 cm needed for the third setup. The wooden holder behind the phantom made sure the slabs were pressed together tightly, thereby minimizing air pockets between successive slabs.

Because of the high dose rate of the S700 source, precautions were taken to protect the physician, according to the “as low as reasonably achievable” (ALARA) principle. The setups visualized in figure 38 were therefore placed in a wooden box reinforced with lead shielding before starting the treatment. This box is depicted in figure 27.

Figure 27: Treatment box

7.1.2 Irradiation and scanning of the films

The following procedure was used to irradiate the EBT3 films for each of the three experimental setups. All films were irradiated for 120 seconds using the nominal air kerma rate of the S700 source of 1400 $\frac{\mathrm{Gy*cm^2}}{\mathrm{h}}$. However, adjustments were made to the initial treatment time before each irradiation to account for the change in source output over several irradiations. Before each irradiation, the actual air kerma rate of the S700 source was measured using Standard Imaging/HDR 1000 Plus well chamber in combination with the Max 4000 electrometer. More information on this topic is available in appendix B. Due to the fact that the source lost some of its original source strength due to wear, most irradiations took around 80-100 seconds instead of the proposed 120 seconds. The dose rate measured by the well chamber was computed using the TG-51 formalism, which is also further laid out in appendix B.

Due to the geometrical shape of the conical 35 mm applicator, the irradiated EBT3 films would contain a blue circle where a dose was deposited, while adjacent untainted areas would remain yellow. Additionally, the shade of blue would be darker in areas where more dose was delivered. An irradiated EBT3 film is shown in figure 28.

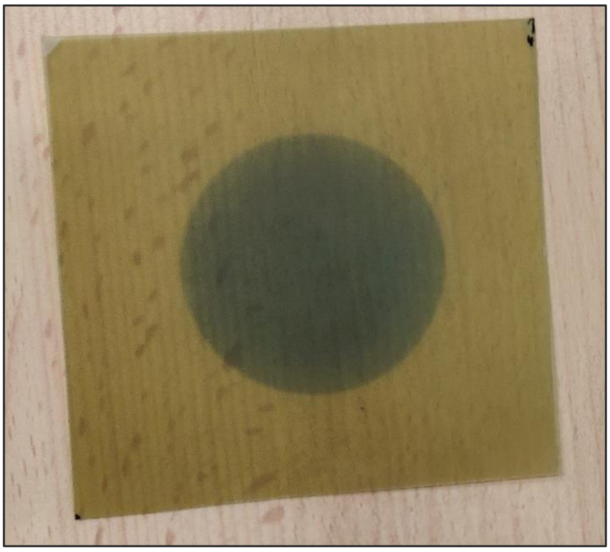

Figure 28: Irradiated EBT3 film

The procedure used to convert a blue discoloration of the EBT3 film to an equivalent dose could be reduced to two major steps. The first step was the scanning of the EBT3 films. These scans were carried out 66 hours after irradiation as some of the diacetylenes in the EBT3 films were not immediately polarised after irradiation. Measuring the scans directly after irradiation would result in a underestimation of the measured dose. To scan the films, the graphical scanner Epson Expression 12000XL Wide-Format Graphic Arts Scanner was used. The scanner first used a light source to scan over the film [46]. After the light hit the film, the light was reflected with a changed intensity and wavelength depending on the film's colour at the location where the light was reflected. The reflected light was then projected through a lens by a series of (curved) mirrors, after which the light hit the Charged-Coupled device (CCD) of the scanner, which held photosensitive cells to convert optical photons into electrons [46]. A red, blue and green strip encapsulated these cells, allowing the CCD to filter out the associated colour. The Epson Expression 12000XL was equipped with a RGB LED source which alternated the emitted colour while scanning the film. This allowed the physician to scan the films using tri-colour channels.

The accumulated charge of each CCD cell was passed through an analog-to-digital (ADC) converter, which converted this charge to a measurable signal for the computer [46]. Finally, these signals were combined and the optical density (OD) was internally calculated according to formula 10.

$$OD = \log_{10}\left(\frac{I_0}{I}\right) \tag{10}$$

In formula 10, I_0 represents the intensity of the initial beam of light and I represents the intensity of the reflected beam of light [40]. Using the calculated OD, filmQA pro is able to reconstruct the colour of the original EBT3 film on each pixel. Figure 29 shows a scanned EBT3 film in filmQA pro.

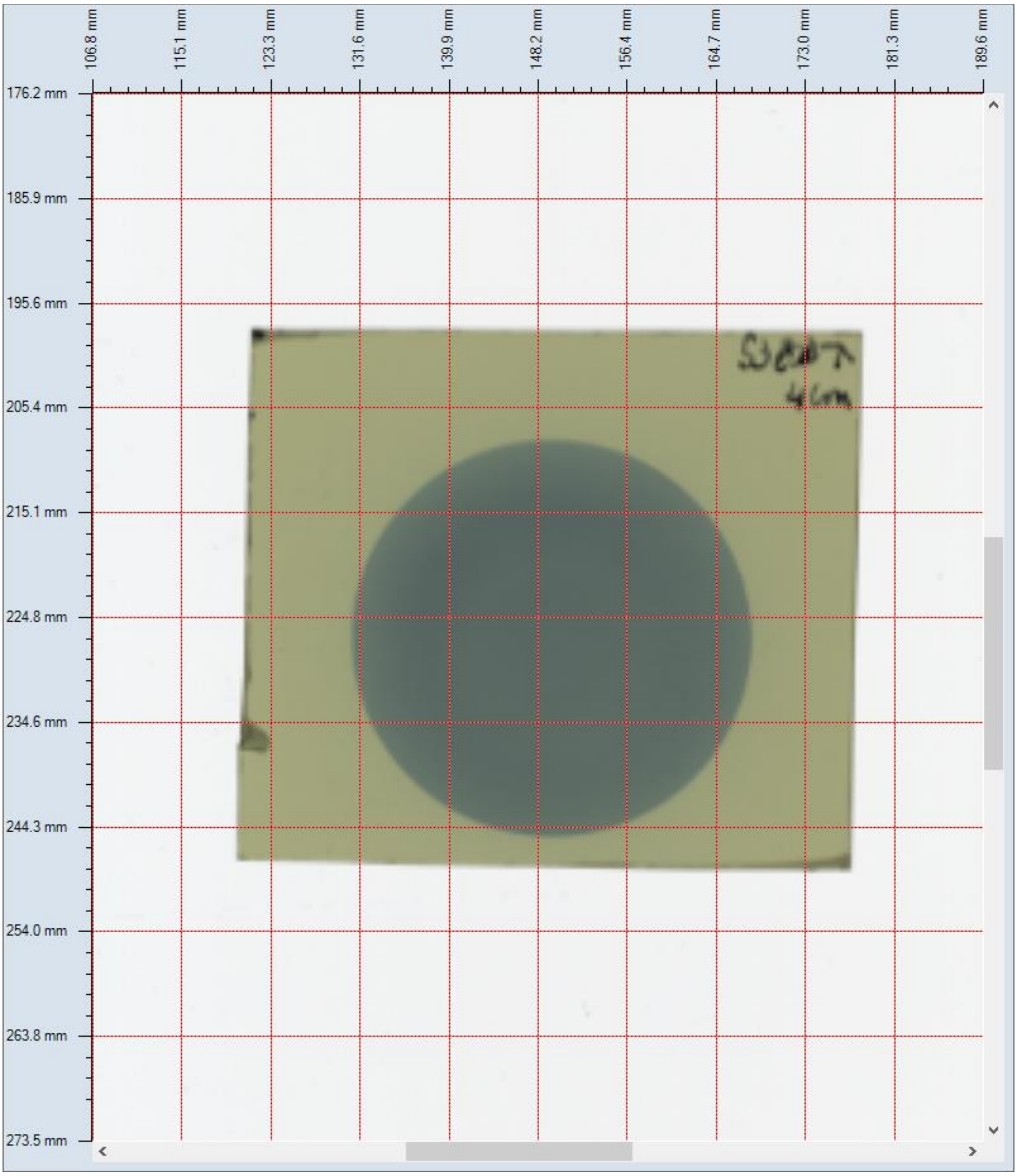

Figure 29: Scanned EBT3 film in filmQA pro

The second step of the procedure includes the transformation of the OD of each pixel to an equivalent dose using calibration curves. These calibration curves were created by irradiating films with a known dose and measuring the associated OD. Using these resulting data points, the OD could be plotted together with the absorbed dose, finally resulting in calibration curves. The absorbed dose was calculated using an adapted version of AAPM TG-61. Considering that these calibration curves were not produced by the writer, but rather by NuTeC personnel in cooperation with Maastro clinic, a more detailed explanation about the calibration procedure can be found in appendix B. Figure 31 shows the calibration curve taken at 66 hours after irradiation, coinciding with the aforementioned time interval between the irradiation of the EBT3 films and the scans. The x-axis represents the dose (cGy) while the y-axis represents the associated OD.

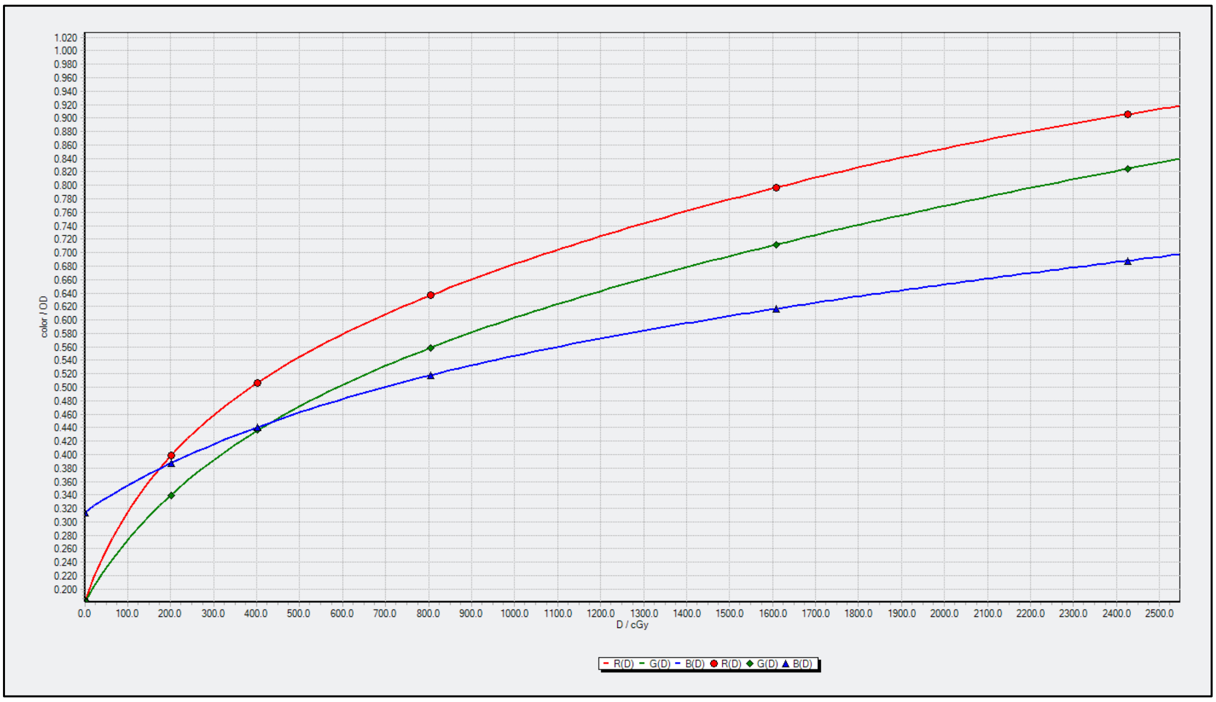

Figure 30: Calibration curve taken at 66 hours after irradiation

7.1.3 Converting dose maps to transversal dose profiles

As mentioned repeatedly in Chapter 4, transversal dose profiles are often measured by reading out the absorbed dose at several points on a line corresponding to either the x-axis or the y-axis. The overlying grid (see figure 29) was used to define the position of each of these data points. The transversal dose profile, measured in air and related to the x-axis, is displayed in figure 31. It should be noted that the x-axis was deemed to be the horizontal that cuts the circular, irradiated area of the EBT3 film in half.

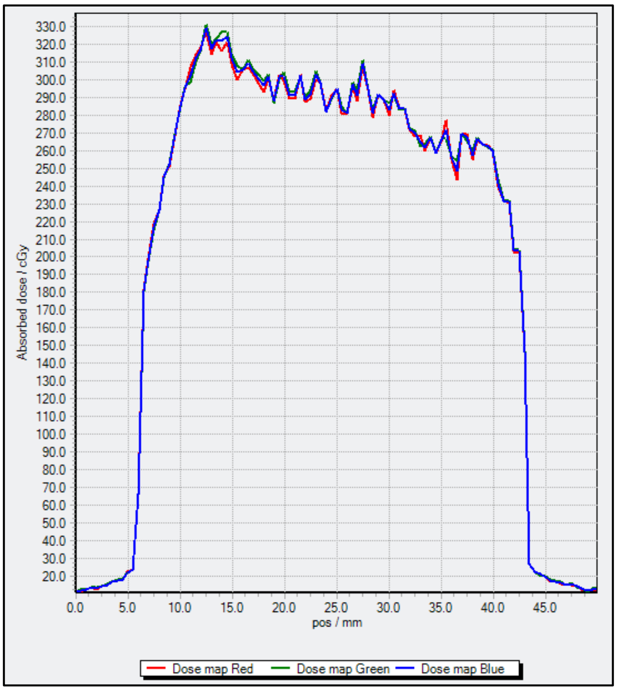

Figure 31: linear transversal dose profile related to the x-axis, measured in air

However, after analysing some measurements, it was determined that these types of linear transversal dose profiles (see figure 31) were not suitable for this thesis. This is explained by the fact that (1) it was impossible to control the orientation of the source relative to the film and (2) the sources were not completely uniform. Because the films were all scanned with the same orientation, the line which was used to construct the linear transversal dose profiles however stayed exactly in the same location. As such, a film A which was hypothetically irradiated in exactly the same way as another film B, but with different orientations of their source relative to the film, would result in completely different linear transversal dose profiles.

To eliminate this problem, transversal dose profiles were instead evaluated on a set of radiuses starting from 0.5 mm up to 24.5 mm with increments of 1 mm for the irradiated EBT3 films in air and in front of the phantom. The EBT3 films irradiated at 1 cm depth in the phantom were evaluated analogously. Still, the outer radius was taken to be 39.5 mm to account for the divergence of the beam due to the increased distance from the applicator surface. filmQA pro v.7 provided the option to evaluate the dose radially using. Nevertheless, it proved hard to align the centre of each of these circles, resulting in potential errors. Instead, these circles were approximated by first obtaining 36 linear transversal dose profiles at angles ranging from 5° to 355° with 10° increments, and then calculating the average absorbed doses at each radius based on the data recorded across the 36 profiles. For these measurements, the centre was located on the beam axis. The average absorbed dose at each radius was finally normalized to the absorbed dose at a radius of 2.5 mm for the first two setups (measurements in air and on the phantom surface) and at 3.5 mm for the last setup (measurement at 1 cm depth in the phantom). Finally, the radial transversal dose profiles could be plotted, representing the normalized absorbed dose at each radius. Henceforth, these kind of profiles will be truncated to transversal dose profiles for both the measurements and the simulations. The aforementioned radiuses selected for normalization were chosen after consideration of the data points originating from the simulated irradiation using the TOPAS MC model, as this allowed the comparison of the measured transversal dose profiles to the associated simulated transversal dose profiles. More on this subject follows in section 7.2.4.

7.2 Generating dose profiles using the MC model

7.2.1 Simulation setups

To verify the validity of the TOPAS MC model, simulated transversal dose profiles were generated using exactly the same three setups listed in 7.1.1. Accordingly, figure 32 shows the setups where the scorer is surrounded by air (left), the scorer is located in front of the 4 cm thick Plastic Water LR phantom (middle) and the scorer is located at 1 cm depth inside the phantom (right).

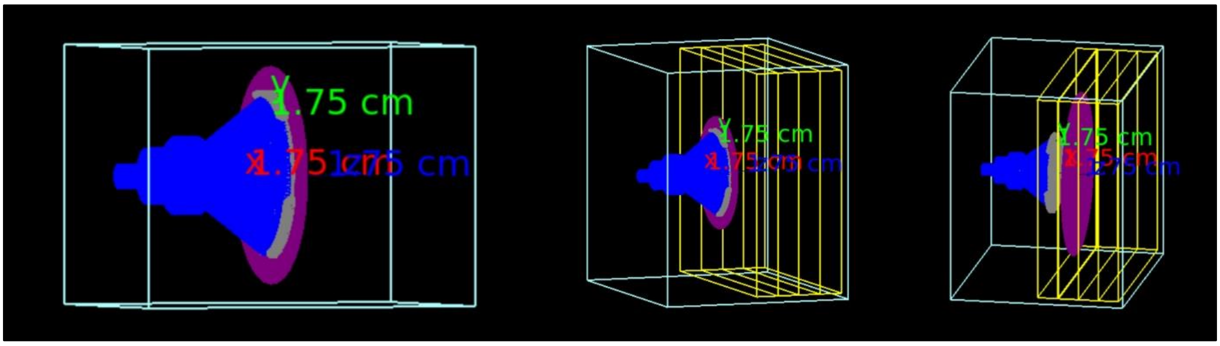

Figure 32: Simulation setups with the scorer in air (left), the scorer on the surface of a 4 cm Plastic Water LR (middle) and the scorer at 1 cm depth in the phantom (right)

In accordance with the experimental setup, the Plastic Water LR phantom was comprised of 4 boxes which each had dimensions of 10x10x1 cm. The material allocated to these boxes was G4_WATER which has similar dosimetric properties to Plastic Water LR, although this could be considered as a slight approximation.

7.2.2 Design and irradiation of the scorer

G4_WATER was also allocated to the scorer which was considered as the virtual counterpart of the EBT3 film to measure the absorbed dose. This scorer was a disc with a thickness of 0.5 mm and a diameter of 50 mm for the first and second setup and 80 mm for the third setup (to account for beam divergence). Moreover, this scorer was partitioned into N sub-scorers, consisting of 1 circular segment in the middle and N-1 ring-shaped segments. The amount of segments N equals 25 for the first two situations, and 40 for the third situation. At first, each segment was 1 mm wide, which resulted in the first version of the scorer, depicted in figure 33. The scorer was only segmented radially and not angularly; the lines intersecting the centre of the scorer are drawn automatically by TOPAS and have no physical implications.

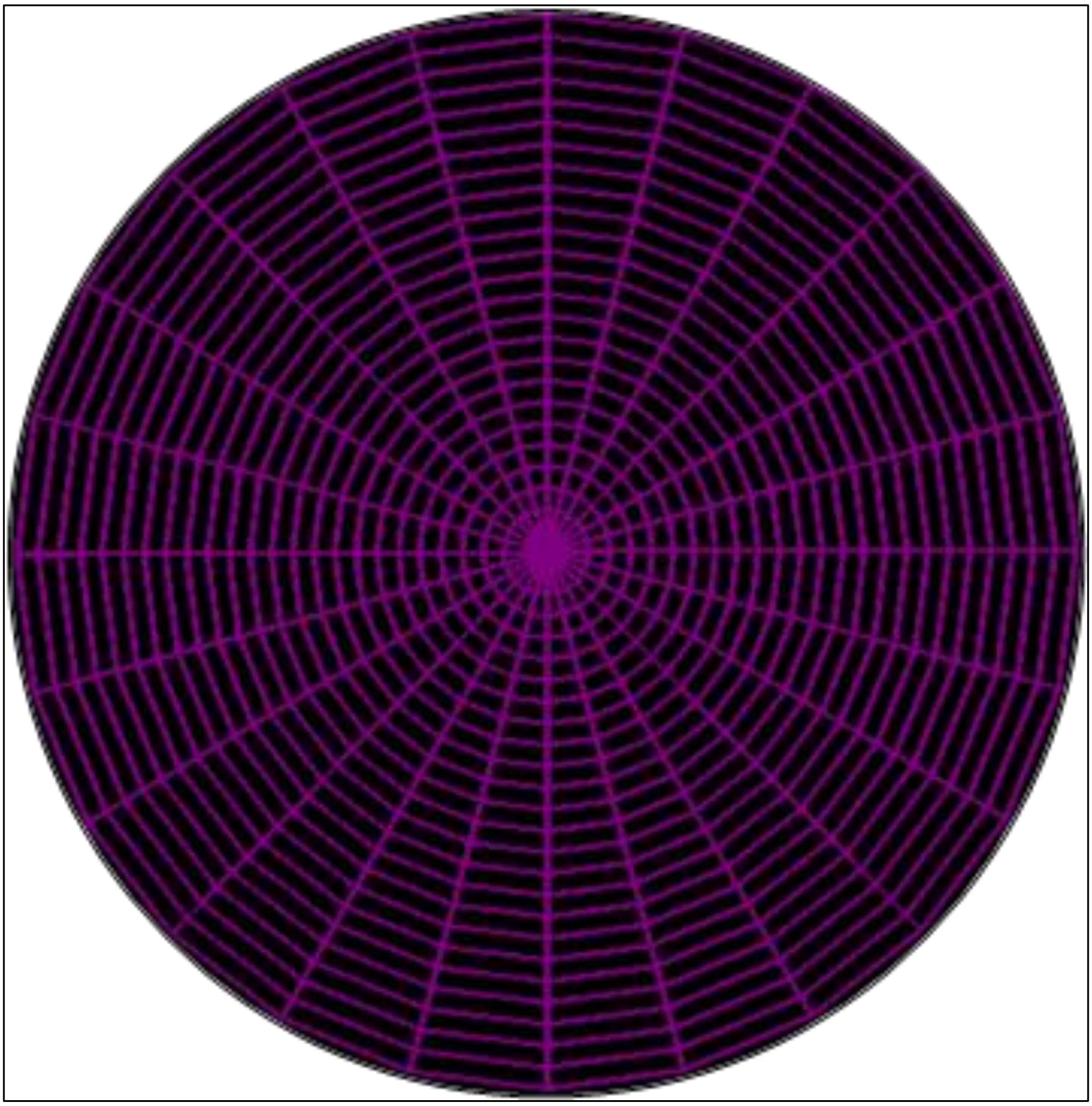

Figure 33: First version of the scorer

The photon spectrum used to irradiate this scorer resulted from the interaction of a virtual electron beam impinging perpendicularly on the target. This electron beam originated from the base of the source tip in vacuum and contained $5 * 10^8$ incident electrons. The design of this electron beam is discussed separately in section 7.2.3. The source tip (see figure 17 and 18) and other parts of the XOFT eBx System, such as the housing of the S700 source, the applicator, the target, the flattening filter, and the catheter with the heat transfer fluid, were imported into the TOPAS MC model using STL files provided by XOFT, Inc. More information on this process and other information regarding the design of the Topas MC model can be found in appendix D.

As conveyed in section 2.2, the relative production of photons in the x-ray tube was severely limited as most of the primary energy from the incident electrons was converted to heat in the target. Regardless, enough photons had to deposit energy in the scorer to produce a trustworthy transversal dose profile with a reasonable uncertainty. Both of these were inversely correlated to the number of photons interacting in the scorer. Subsequently, a huge history of incident electrons needed to be simulated to produce an uncertainty on the transversal dose profiles less than 3%, resulting in a very long computation time. As such, two kinds of variance reduction techniques were applied in the simulations.

The first kind of variance reduction technique employed was particle splitting, defined as Secondary Biasing in TOPAS [47]. More specifically, secondary biasing was a subtype of particle splitting, focused on the splitting of secondary particles after an electromagnetic interaction, such as the splitting of secondary photons created in the bremsstrahlung process. For the simulations carried out in this thesis, a splitting factor of 250 was used. This meant that 250 identical photons were produced every time a photon would originate from the target, significantly reducing the eventual uncertainty on the absorbed dose. To balance out this adaptation the weight (a measure of the importance of a photon) of every photon was also divided by 250. As such, every photon weighted 1/250. Like most other splitting techniques, secondary biasing also subjected these newly created photons to Russian roulette based on their energy and direction [47]. This technique killed photons with certain probability K, where $0 < K < 1$, when the criteria mentioned below were met. If they survived, their weight would increase accordingly with a factor of $1/(1-K)$ [47]. The criteria for Russian roulette to occur, pertaining to the energy of the photons, was chosen to be > 52 keV. This was slightly higher than the energy of 50 keV of the most energetic photons when the S700 source operated at 50 kVp. This implied that Russian roulette pertaining to the energy of the photons was turned off for this thesis. Russian roulette was however still used for the direction of the photons. This subjected a photon to Russian roulette if the photon had a direction pointing away from the ROI [47]. The ROI was defined as a circle with a radius and a translation relative to the target which, as mentioned above, was the splitting location. Figure 34 is visualized below to provide clarity on this subject.

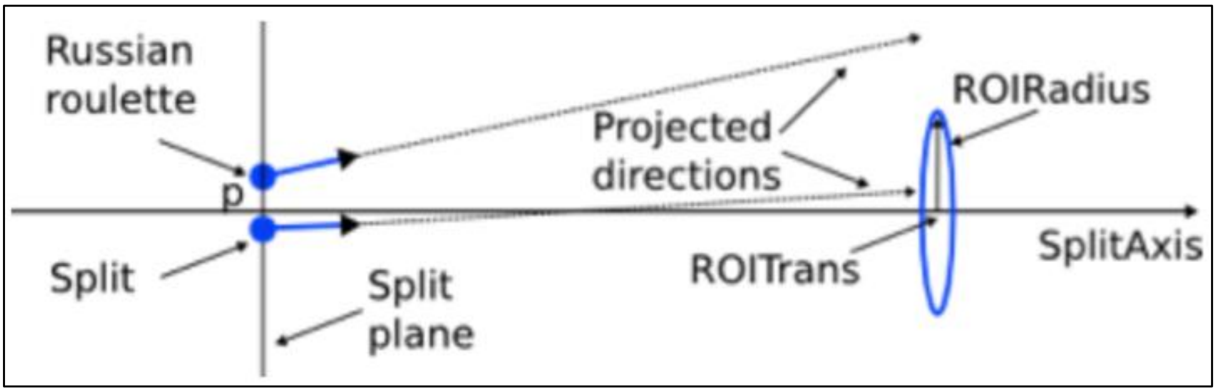

Figure 34: Implementation of Russian roulette for directional splitting [47]

No translation was applied, meaning that the ROI would align with the target itself. The radius of the ROI was set to 17.5 mm which coincided with the radius of the applicator.

A second kind of variance reduction was implemented following the realization that particle splitting alone still yielded an unsatisfactory computation time for the desired uncertainty of 3%. The method entailed the implementation of a linear Track length estimator (TLE). This variance reduction technique approximates the absorbed dose in the film as collision kerma [48]. This resulted in a new definition for the absorbed dose in the film according to formula 11.

$$D = \frac{L}{V} * E * \frac{\mu_{en}}{\rho} \qquad (11)$$

In formula 11, L and V were representative of the length and the volume of a voxel inside the film, E stood for the energy of the photon depositing the dose and $\frac{\mu_{\mathrm{en}}}{\rho}$ was the mass energy absorption coefficient [48]. Using TLE, the dose along the voxels encountered by the photon between two successive collisions was considered, thereby resulting in a major variance reduction [48].

After being subjected to secondary biasing, some of the resulting photons would incur an absorbed dose in multiple segments of the scorer according to the TLE mechanism, represented by formula 10. Besides the sum and the mean of this absorbed dose, each segment of the scorer was also instructed to keep track of the absorbed dose's variance, the absorbed dose's standard deviation, the amount of initial histories and finally the amount of interactions in each segment. After each simulation had completed, the output of each segment was written into a separate Comma-separated values (CSV) file, ready to be processed by the user.

After careful assessment of the uncertainty on the generated transversal dose profiles (the acquisition of the uncertainty will be further discussed in section 7.3), it was found that the uncertainty on the absorbed dose would still be significantly higher than the desired limit of 3%, even reaching as much as 11% in some segments. These large uncertainties would be recorded in the ring-shaped segments closest to the centre, but less so in the circular segment itself. This was a logical result of the scorer's geometry. Indeed, the circular disc comprised segments with the same thickness, which inevitably led to larger surface areas for the ring-shaped segments on the side of the scorer and smaller ones in the middle. Formula 12 and 13, which were respectively the formula for the surface area for the circular segment $\mathrm{A_c}$ and a ring-shaped segment $\mathrm{A_r}$, confirmed this statement.

$$A_c = \pi * R^2 \tag{12}$$

$$A_r = \pi * (R^2 - r^2) \tag{13}$$

In these two formulas, R signified the outer radius of the assessed segment and r signified the inner radius of this segment relative to the center.

When evaluating a ring-shaped segment A close to the centre lying in between 2 mm and 3 mm, the surface area would be 15.71 mm^2, while a segment on the sides of the scorer B lying in between 24 mm and 25 mm from the centre, would result in a surface area of 154.94 mm^2. Therefore, despite the higher photon flux reaching the middle of the scorer compared to the sides, segment B would still register significantly more interactions than segment A. This accounted for the lower uncertainties in the outer segments of the scorer and the higher uncertainties recorded in ring-shaped segments close to the centre. The uncertainty recorded in the circular segment would be slightly above average considering that this segment was very small ($\mathrm{A_c} = 3.14\ \mathrm{mm}^2$) but still acceptable since the beam axis directly intersected with this segment, thereby partly compensating for its small size with the large flux of photons.

As a result, this first design of the scorer was changed in favour of a second design, which adapted the inner and outer radii of its segments to guarantee that each segment had an equal surface area. This second model of the scorer, the ESA scorer, therefore divided its total surface area by 25 (or 40 in the case of the scorer pertaining to the setup at 1 cm depth in the phantom). The radii of these segments could then be calculated by transforming the formulas 19 and 20. In addition to this change, each segment was also divided angularly into 36 segments of 10° each. This second adaptation made it possible to use the same CSV files to construct linear transversal dose profiles corresponding to specific angles. Nevertheless, these were not used for this thesis. The resulting scorer is visualized in figure 35.

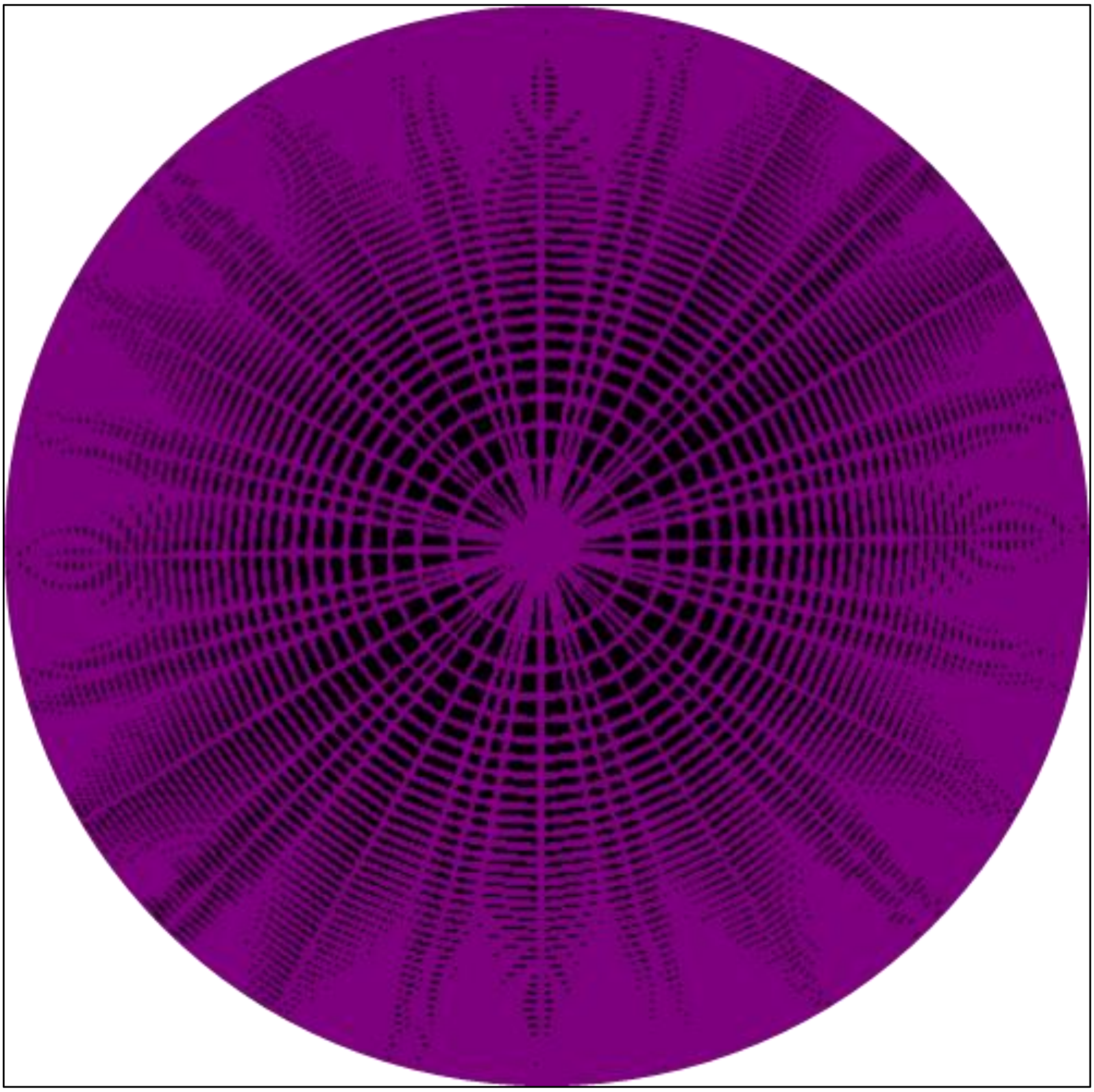

Figure 35: The second model of the scorer: the ESA scorer

In conclusion, the ESA scorer was irradiated with $5 * 10^8$ incident electrons. The electrons collided in the target and produced bremsstrahlung photons which were split by a factor of 250 and subjected to directional Russian roulette coinciding with the 35 mm applicator. The absorbed dose in the ESA scorer due to these photons was calculated using the TLE mechanism. The resulting values, including the summed absorbed dose, mean absorbed dose, variance of the absorbed dose, standard deviation of the absorbed dose, number of initial histories, and number of interactions in each segment, were then written to a separate CSV file. Making use of the services provided by the Vlaams Supercomputer Centrum (VSC), the simulations were carried out on the Genius cluster where a single node was used with 36 cores for each simulation. Such a simulation typically took 14 – 16 hours, depending on the setup and the traffic on the VSC servers.

7.2.3 Design of the electron beam

The original Topas MC model had a simplified design of the electron beam [25,26]. The diameter of the 1.6 mm electron beam was aligned with the diameter of the base of the source tip, from which it originated and impinged perpendicularly on the target. Furthermore, the electron beam had a flat position distribution, which meant that the electrons were dispersed equally in the circular shape. No angular distribution was put in place, which meant that all electrons would traverse the vacuum parallel to the beam axis. Additionally, no particle cutoff was specified which meant that Topas automatically resorted to the default cutoff parameter of 1 mm. This meant that every parameter was cut out of the simulation when the particle was predicted to travel less than 1 mm inside the current medium based on its current energy. Due to the resulting simulated transversal dose profiles (see section 8.2.1) it was however quickly realised that this model of the electron beam in the TOPAS MC model was not exactly correct. When research was carried out concerning the shape and the size of electron beams, it was noted that there was no real consensus about how an electron beam should look like in an x-ray tube [49, 50]. Rather, most sources list that the design of the electron beam is heavily influenced by the design of the specific x-ray tube. For example, a smaller filament would result in a smaller electron beam compared to a larger filament, and a stronger electric field would result in a more tightly focussed electron beam [49, 50]. Additionally, a higher tube current would result in a broader electron beam due to the increased Coulomb force exerted by the larger number of electrons on each other [49]. Moreover, it was anticipated that, in addition to the size and shape of the electron beam, the angular deviation of the electron beam and the distribution of the electrons inside the beam would also change due to these alterations in design of the x-ray tube.

This sentiment was confirmed from direct communication with XOFT, inc. It was communicated that the size and shape of the electron beam could be roughly determined by measuring the focal spot of the photon beam generated in the target. This focal spot was measured using a pin-hole camera fitted with an x-ray image plane (a film dosimeter). Considering that the focal spot was a result of the electron beam impinging on the target, the size and shape of the electron beam would be comparable to those of the focal spot. It should however be considered that these were not a direct measurement of the electron beam, as the detector was more sensitive to the high energy photons. Keeping this in mind, the design of the electron beam changed considerably when comparing different sources. Some sources displayed circular electron beams, while others displayed a point like beam or an elliptical star.

As a result, it was very hard to precisely define the correct approach for the design of the electron beam in the XOFT eBx System. Instead, the electron beam was iteratively refined until the resulting simulated transversal dose profiles agreed within 10% with corresponding measured transversal dose profiles. These changes were carried out with respect to (1) the size of the electron beam, (2) the shape of the electron beam, (3) the distribution of the electrons inside the electron beam and (4) the cutoff distance of the electrons in the electron beam. The resulting change of each adaptation was recorded and summarized in table 3. The final TOPAS MC model was summarized in section 8.2.3, after which this model was used to simulate transversal dose profiles using $1 * 10^9$ histories to further minimize the uncertainty on the simulated transversal dose profiles.

7.2.4 Converting CSV files to transversal dose profiles

After each simulation, the CSV files from the corresponding segments were first downloaded from the VSC server. The summed absorbed dose and the standard deviation on the absorbed dose were then collected from these files, and each of these quantities were then transferred into a separate 36x25 matrices (or 36x40 for the measurement at 1 cm depth) with the rows coinciding with the angular segmentations and the columns coinciding with the radial segmentations. Then, the matrix containing the standard deviations on the absorbed dose was transformed into an equivalent matrix of standard deviations on the summed absorbed dose.

The radiuses of evaluation for the transversal dose profiles were deemed to be the middle of each segment. At each of these radii, the average summed absorbed dose across the 36 angular segments was calculated. Finally, the average dose was plotted in function of the different radii, resulting in transversal dose profiles. The uncertainty on the average dose was also calculated and plotted on this graph. Both the average dose and the uncertainty were normalized relative to the smallest recorded radius, taken to be 2.5 mm for the first 2 simulation setups and 3.5 mm for the third simulation setup. This normalisation was chosen after consideration of the data points resulting from EBT3 film measurements on the one hand, and the data points resulting from the simulated irradiation of the scorer on the other hand. In order to compare the normalised transversal dose profiles, the normalisation had to be calculated at the same radius. Due to the segmentation of the ESA scorer, the first data point of the simulated irradiation coincided with the middle of the circular segment. This data point was located at 2.5 mm for the first two setups and 3.5 mm for the last setup. As such, the normalisation could not be carried out at distances smaller than these data points, which eventually resulted in the normalisation at these same data points for both the measured transversal dose profiles using the EBT3 films, and the simulated transversal dose profiles using the TOPAS MC model.

7.3 Uncertainty analysis

For this thesis, two major sources of uncertainty had to be considered. Firstly, there existed a source of uncertainty on the measurements using the EBT3 films. This originated from the conversion of the film itself to the OD map of the scanned films. These uncertainties could be calculated for each angle from the consistency map in filmQA pro. This consistency map displayed the deviation (in Gy) at each measurement point for the three colour channels. These deviations were first averaged across all colour channels and then across all measurement points for one angle. Then, the individual average deviations for each angle were combined into a grand average across all angles, which was used to calculate the uncertainty of the measured transversal dose profiles. This was accomplished by dividing the aforementioned grand average by the dose measured at 2.5 mm for the first two experimental setups and the dose measured at 3.5 mm for the last experimental setup.

Secondly, there was a source of uncertainty stemming from the simulated irradiations in TOPAS. The first step of calculating this uncertainty was calculating the standard deviation on the absorbed dose calculated by Topas during the simulations. After the simulations had finished, the respective standard deviation of the absorbed dose was deviated into a matrix. This matrix was then multiplied with the square root of the histories to find the matrix representing the standard deviation on the summed absorbed dose. These histories were $5 * 10^8$ incident electrons, except for the simulated transversal dose profiles from the final TOPAS MC model, which were simulated using $1 * 10^9$ histories. Considering that the transversal dose profiles were constructed using the average summed absorbed dose across the 36 angular segments, formula 14 then resulted in the standard deviation on this average summed absorbed dose conform with the principle of error propagation.

$$s_a = \frac{\sqrt{s_1 + s_2 + \cdots + s_{35} + s_{36}}}{36} \tag{14}$$

In formula 14, $\mathrm{s_a}$ was the standard deviation on the average summed dose, $\mathrm{s_k}$ was the standard deviation of the summed dose in angular segment and k is the particular segment evaluated ranging from 1 to 36. After calculating the standard deviation on this average summed absorbed dose at each of the evaluated radii, the corresponding uncertainty at these radii was finally calculated by normalization relative to the average summed dose at 2.5 mm for the first two simulation setups, and 3.5 mm for the third simulation setup. The uncertainties for both the measured and simulated transversal dose profiles were indicated using error bars.

7.4 Evaluation and comparison of the measured transversal dose profiles to the simulated transversal dose profiles

The measured and simulated transversal dose profiles were compared in two ways. Firstly, they were compared using visual inspection after which the maximal difference between the two plots was determined. However, since the measured transversal dose profiles were plotted using different data points than their simulated counterparts, linear interpolation was used to determine additional data points for either the simulated or measured transversal dose profiles, depending on the situation. The calculation used for linear interpolation was performed according to formula 15.

$$D_{new} = D_{old1} + \frac{(r_{new} - r_{old1}) * (D_{old2} - D_{old1})}{(r_{old2} - r_{old1})} \tag{15}$$

In formula 15, $\mathrm{D_{new}}$ was the new interpolated measured dose at the desired radius $\mathrm{r_{new}}$, and $\mathrm{D_{old2}}$/ $\mathrm{D_{old1}}$ were the known measured dose at radii $\mathrm{r_{old2}}$/ $\mathrm{r_{old1}}$, which lay on both sides of the desired radius.

Secondly, the measured and simulated transversal dose profiles were compared using the beam flatness of each profile. The beam flatness for the transversal dose profiles, measured in air and on the phantom surface, was defined using AAPM TG-45. This protocol defined the beam flatness for transversal dose profiles as the maximal dose difference measured inside an interval equivalent to 80% of the full width at half maximum (FWHM) [51]. When the film was in direct contact with the applicator, the FWHM maximum roughly coincided with the nominal beam width of the applicator. As such, instead of calculating 80% of the FWHM of each profile, the interval was defined as 80% of the nominal beam width of 35 mm, which was equal to 28 mm [37]. Since transversal dose profiles were evaluated radially instead of linearly (see section 7.1.3), this interval would lie in between a radius of 2.5 mm and 14 mm. The minimum radius of evaluation of 2.5 mm was chosen to ensure the same evaluation for both the measured and the generated transversal dose profiles. Formula 16 represented the method to calculate the beam flatness F, expressed as a percentage [51].

$$F = \frac{D_{max} - D_{min}}{D_{max} + D_{min}} * 100 \tag{16}$$

In formula 16, D_{max} signified the maximal dose and D_{min} signified the minimal dose measured between a radius of 2.5 mm and 14 mm on a specific transversal dose profile. From formula 16, it could be deducted that a small absolute value for the beam flatness would indicate a flat transversal dose profile, as the difference between the maximal and the minimal dose would be relatively small.

8 Results & Discussion

To accomplish the objectives outlined in section 1.3.2, transversal dose profiles of the XOFT EBX System are firstly measured using EBT3 films. This process is described in section 8.1. In section 8.2, simulated transversal dose profiles are generated using the original Monte Carlo model of the XOFT Accent electronic brachytherapy (EBX) System. After assessing the differences between the measured and simulated dose profiles, the electron beam is iteratively refined (see section 7.2.3) to eventually establish the final Topas MC model. The simulated dose profiles using this final model are then finally compared to the measured transversal dose profiles. The changed induced to the simulated transversal profiles due to different adaptations of the electron beam are also summarized.

After each group of results, there is a short discussion which is necessary to motivate the following measurements/simulations. Nevertheless, in chapter 9, a general discussion is also held to summarise the most important parts. To eliminate possible confusion, the average summed absorbed dose will be referred to as either the absorbed dose or simply “dose” in this chapter.

8.1 Measured transversal dose profiles

8.1.1 Original source

In figure 36, the measured transversal dose profiles are shown for the irradiations (1) in air, (2) on the surface of the Plastic Water LR phantom and (3) at 1 cm depth inside this phantom. All measurements are conducted using the original source (see section 7.1.1)

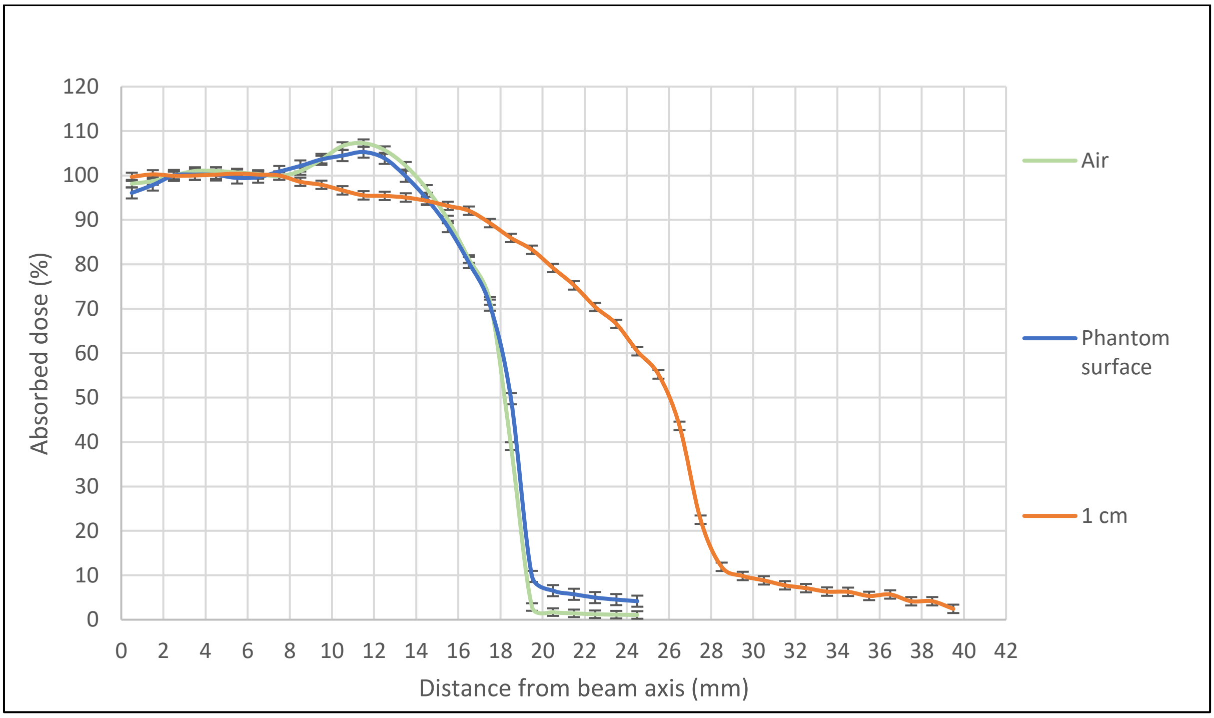

Figure 36: Measured transversal dose profiles for the three setups, using the original source

Intuitively, a higher dose is expected on the beam axis as the photon flux increases close to the beam axis, which is the case for the transversal dose profile measured at 1 cm depth inside the phantom. However, the exact opposite is observed on the transversal dose profiles measured in air and on the phantom surface. Indeed, both of these transversal dose profiles clearly exhibit an off-axis dose increase which in literature is often referred to as a “horn” on the profile due to its physical appearance. The horns are located at 11.5 mm for both profiles. The peak dose levels measured on these horns are 107.3% in air and 105.3% on the phantom surface.

The first potential culprit for the formation of these horns was deemed to be the flattening filter equipped in the 35 mm applicator. As illustrated in figure 23, the flattening filter has more material in the middle and less material on the edges. As such, photons in the middle of the beam must pass through more material than photons on the edges of the beam. As such, these photons are more likely to interact in the flattening filter, resulting in them not reaching the EBT3 film. This design is intentional and aims to compensate for the increased photon flux close to the beam axis, thus theoretically resulting in flat transversal dose profiles. The hypothesis was that this flattening filter was designed to ensure a flat dose profiles for depth irradiations, where the scattering from the photons inside the body towards the beam axis would result in a flat profile. The dose profile at 1 cm depth inside the phantom seemed to confirm this statement. Therefore, the absence of scattering could potentially explain the presence of the horn observed in the transversal dose profiles measured in air and on the phantom surface. In these cases, the flattening filter may cause an overcompensation, resulting in the observed horn on the associated transversal dose profile.

To prove this hypothesis, three additional non-clinical S700 sources were used to measure transversal dose profiles for the same experimental setups, which were then compared to the transversal dose profiles using the original S/N 960251 S700 source. Considering that the same 35 mm applicator was used with the same flattening filter as before, the resulting transversal dose profiles of the three new sources should contain roughly the same horns at the same location (around 11.5 mm), if the new sources were identical to the original source.

8.1.2 Comparison of the original source to other sources

For the next graphs the original S/N 960251 S700 source is referred to as S1. Additionally, the three new non-clinical S700 sources with serial numbers 927021, 960258 and 960386, are referred to as S2, S3 and S4, respectively. Figure 37 shows the transversal dose profile measured in air, while figure 38 shows the transversal dose profiles measured on the surface of the Plastic Water LR phantom. Finally, figure 39 shows the transversal dose profiles measured at 1 cm depth inside the phantom.

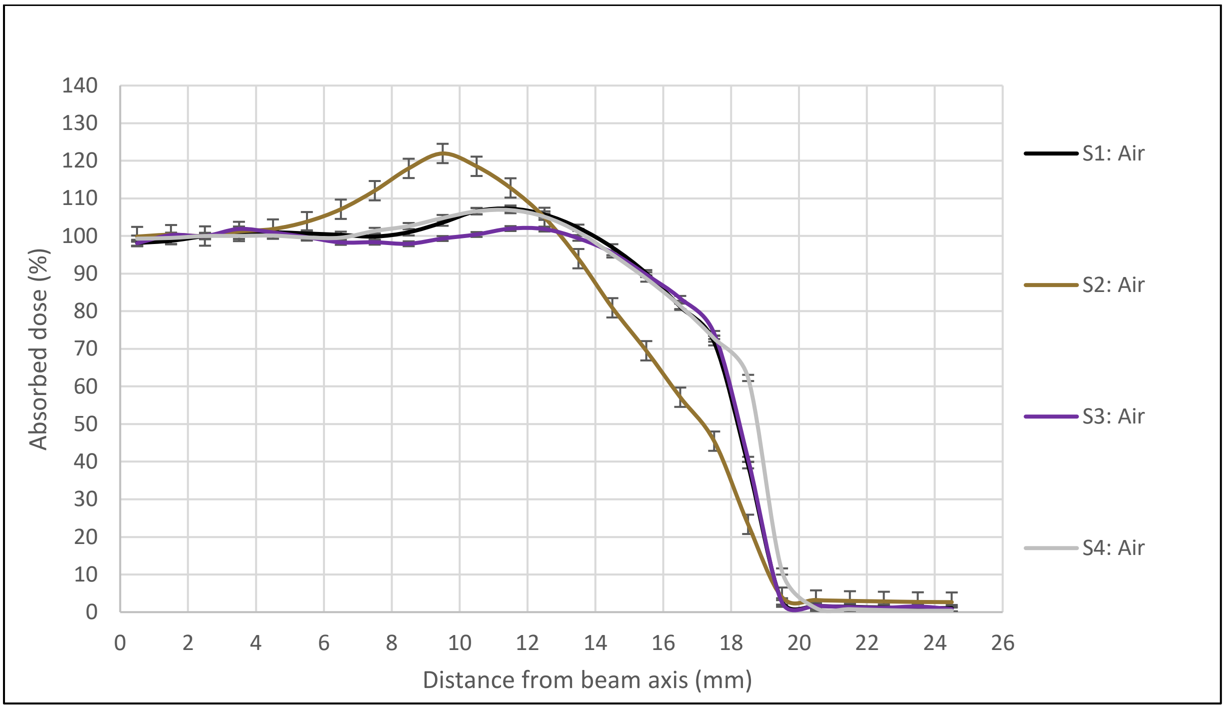

Figure 37: Transversal dose profiles measured in air using the four different sources

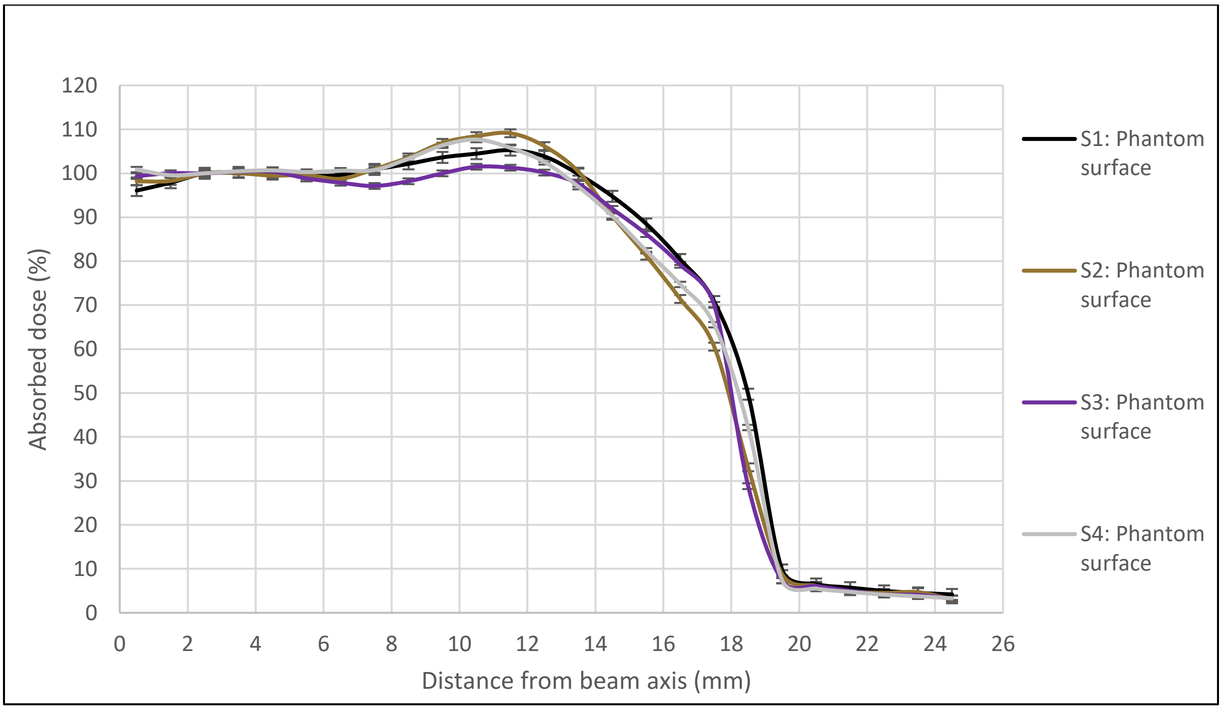

Figure 38: Transversal dose profiles measured on the phantom surface using the four different sources

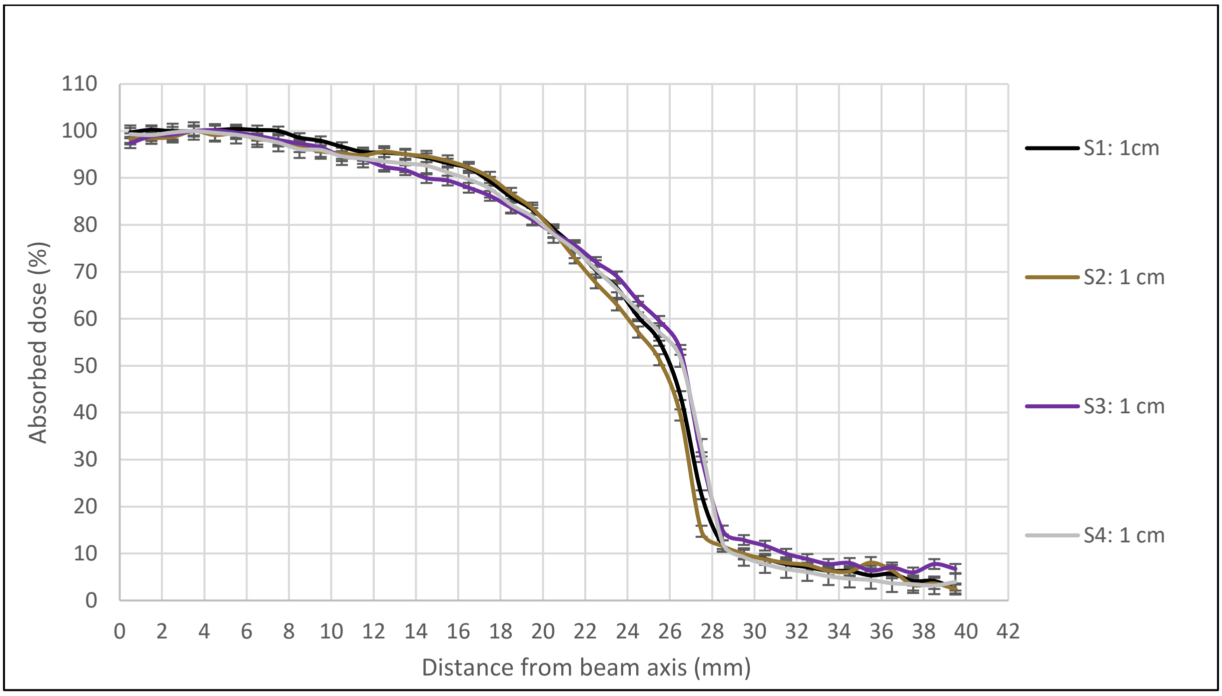

Figure 39: Transversal dose profiles measured at 1 cm depth in the phantom for the four different sources

On figure 37 and 38, it can be concluded that the horns on the measured transversal dose profiles not only vary in height but also in location when comparing the four different sources. As such, it can be concluded that the horns primarily originate from the sources themselves rather than the flattening filter. However, it cannot be entirely ruled out that the flattening filter may have some influence on the formation of the horns, as all sources exhibit horns on their transversal dose profiles in both air and on the phantom surface. The noticeable (albeit smaller) differences between the different transversal dose profiles measured at 1 cm on figure 39 support the conclusion that a change in source has a considerable impact on the shape of the transversal dose profiles.

Overall, it can be deduced that S3 produces the flattest transversal dose profiles. Subsequently, this source is selected as the benchmark for the measurement of transversal dose profiles. As such, the simulated transversal dose profiles will henceforth be compared to the measured transversal dose profiles using S3.

8.2 Simulated transversal dose profiles

8.2.1 Original TOPAS MC model

Figure 40, figure 41 and figure 42, show the measured and simulated transversal dose profiles for the setups in air, on the surface of the Plastic Water LR phantom and at 1 cm depth inside this phantom.

For the first two setups, the beam flatness is also calculated for both the measurements and the simulations. These are recorded in table 1 and 2.

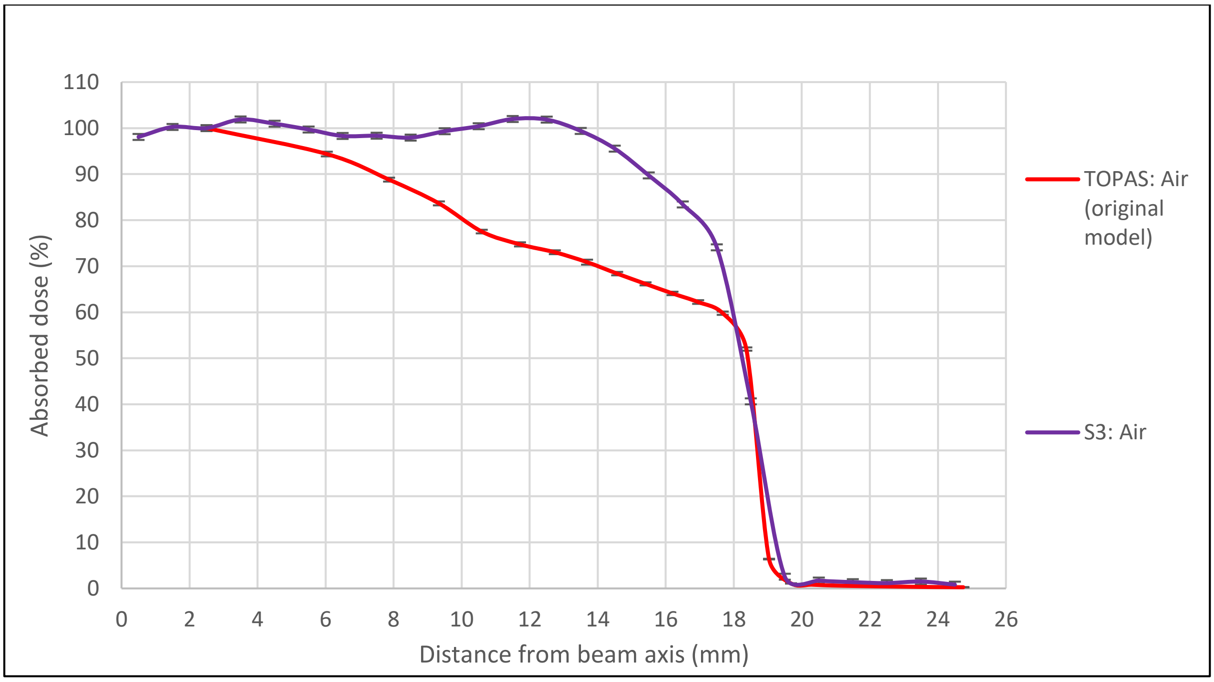

Figure 40: Measured and simulated (original Topas MC model) transversal dose profiles in air

Table 1: Beam flatness calculated for the measured and simulated (original Topas MC model) transversal dose profiles in air

Type of transversal dose profile	D_{max} (%)	D_{min} (%)	beam flatness F (%)
Measured	102.0	97.9	2.0
Simulated	100.0	70.9	17.0

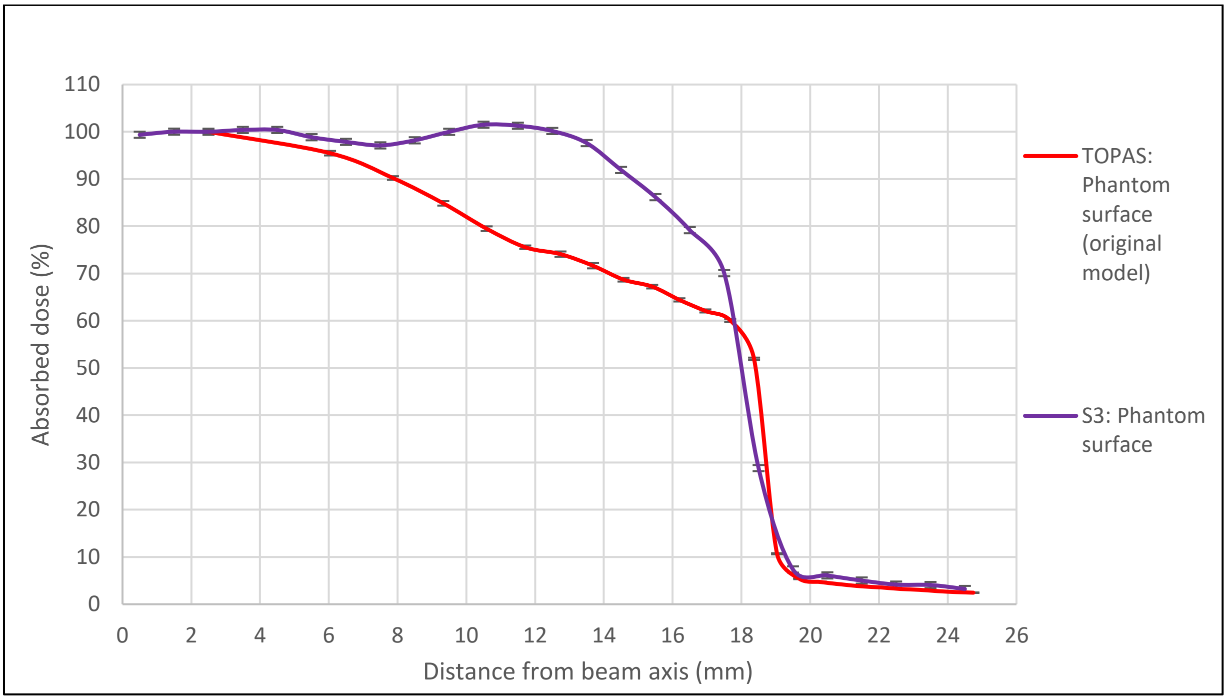

Figure 41: Measured and simulated (original Topas MC model) transversal dose profiles on the phantom surface

Table 2: Beam flatness calculated for the measured and simulated (original Topas MC model) transversal dose profiles on the phantom surface

Type of transversal dose profile	D_{max} (%)	D_{min} (%)	beam flatness F (%)
Measured	101.5	97.1	2.2
Simulated	100.0	71.6	16.5

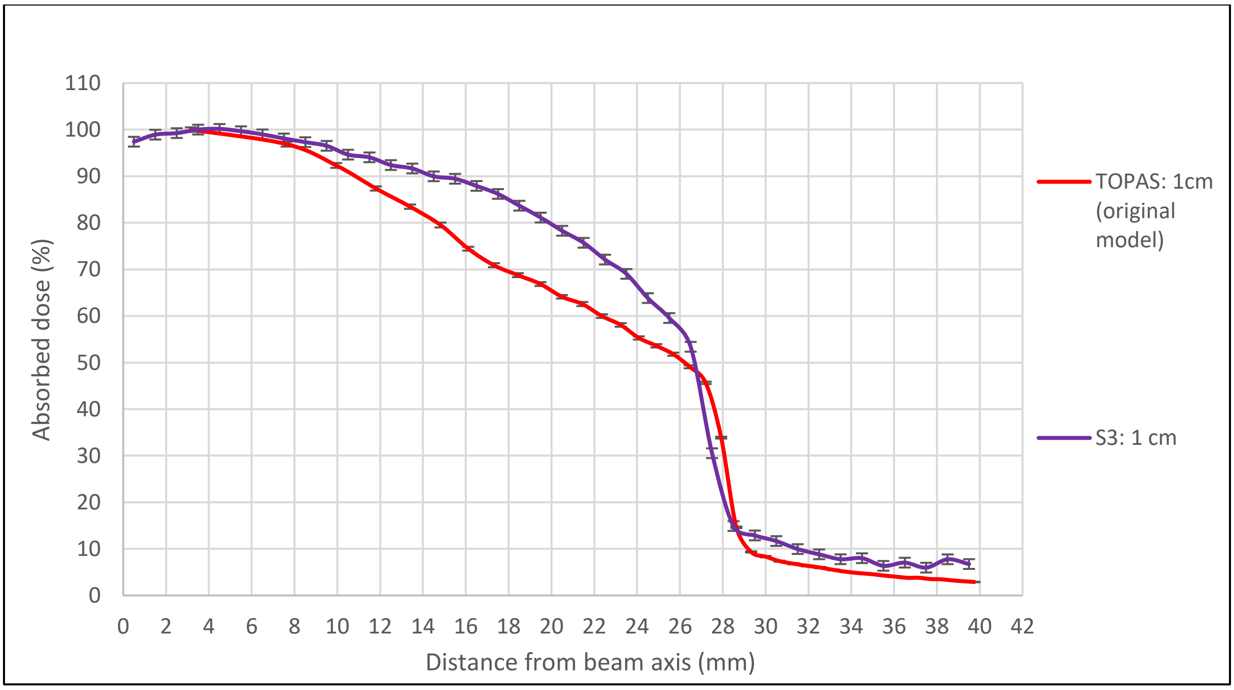

Figure 42: Measured and simulated (original TOPAS MC model) transversal dose profiles at 1 cm depth inside the phantom

For each of the three setups, there are significant discrepancies (higher than 10%) between the measured and the simulated transversal dose profiles. This is especially the case for the profiles belonging to the irradiations in air (figure 40) and on the surface of the Plastic Water LR phantom (figure 41), as the simulated transversal dose profiles display a radial dose drop off instead of the horns on the measured transversal dose profiles. The maximal difference between the corresponding dose profiles is 28.4% in air and 25.7% on the surface of the phantom, both recorded at 12.5 mm. These results are echoed by the difference in beam flatness, recorded at 15.0% and 14.3%, respectively. When compared to the former two setups, the setup at 1 cm depth in the phantom (figure 42) results in lower differences between the transversal dose profiles due the absence of the horn on the measured transversal dose profile. The maximal difference is located at 17.3 mm and amounts to 15.8%.

8.2.2 Adaptation of the electron beam

Size of the electron beam

Firstly, the size of the electron beam is adapted. As such, the size of the electron beam is downscaled from a diameter of 1.6 mm to a pencil beam with a diameter of 0.2 mm. Figure 43 depicts the transversal dose profiles measured at the surface of the Plastic Water LR phantom, along with the simulated profiles using the original model and the pencil beam model.

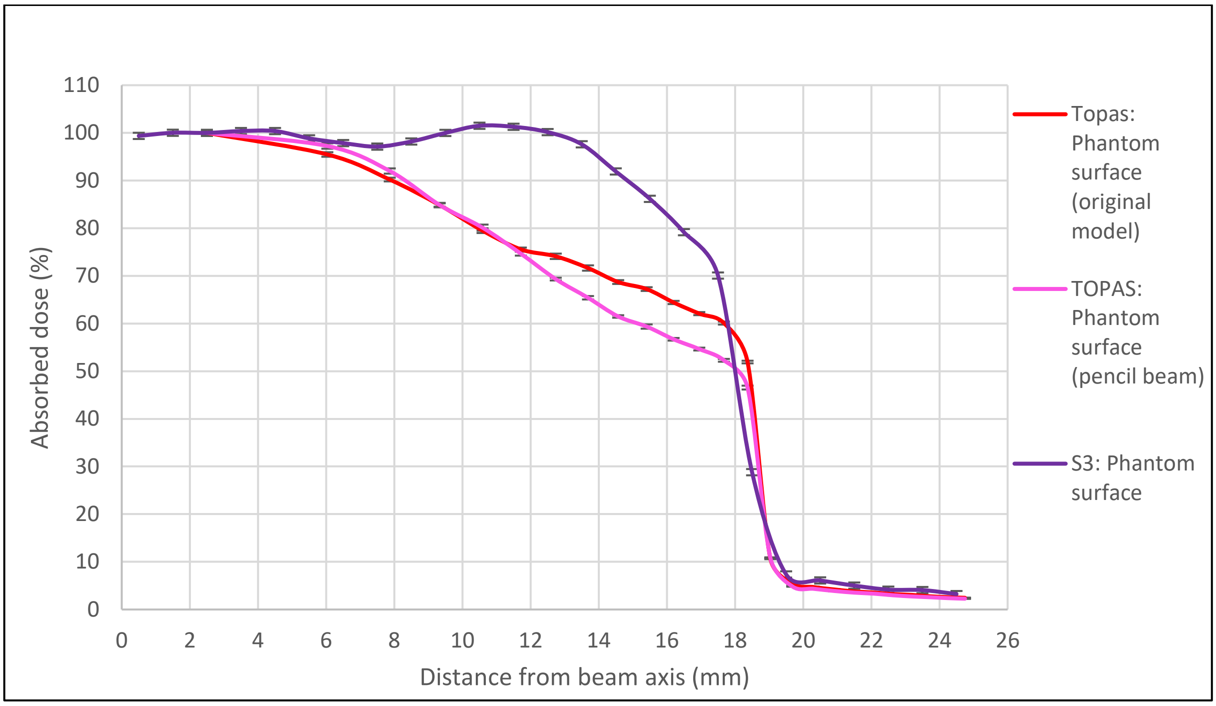

Figure 43: Measured transversal dose profile compared to simulated transversal dose profiles of (1) the original TOPAS MC model and (2) the pencil beam model, all profiles taken at the phantom surface.

The transversal dose profile generated using the pencil beam model (figure 43) exhibits a central increase in dose from a radius of 2.5 mm to approximately 9 mm, while simultaneously showing a decrease in dose on the sides of the profile starting around a radius of 12 mm. Indeed, the flat position distribution demands that the same number of electrons ($5 * 10^8$) are dispersed equally inside the circular shape of the electron beam. Consequently, reducing the size of the electron beam leads to a higher concentration of electrons near the beam axis of the electron beam. This, in turn, results in a higher photon flux close to the beam axis of the photon beam at the cost of the photon flux further from the beam axis, thereby accounting for the shape of the transversal dose profile.

While research was done regarding the impact of changing the size of the electron beam on the corresponding dose profile, it was realized that the STL file used to model the source tip was downscaled very slightly when imported into TOPAS. More information on this subject is available in appendix D. As such, the electron beam is downscaled accordingly. This leads to a new electron beam with a diameter of exactly 1.596944 mm which is henceforth used. This very small adaptation does not have any impact on the simulated transversal dose profiles. Thus, this change was applied for the next simulations, even though this was still considered as the original TOPAS MC model.

Shape of the electron beam

Secondly, the circular shape of the electron beam is changed into an elliptical shape. The long axis was aligned sequentially with both the x-axis and the y-axis which had the same length than the source tip diameter as before. The short axis with a diameter of 1.0 mm was aligned with the other axis. Figure 44 contains the simulated transversal dose profiles on the phantom surface for these elliptical electron beams and the original model.

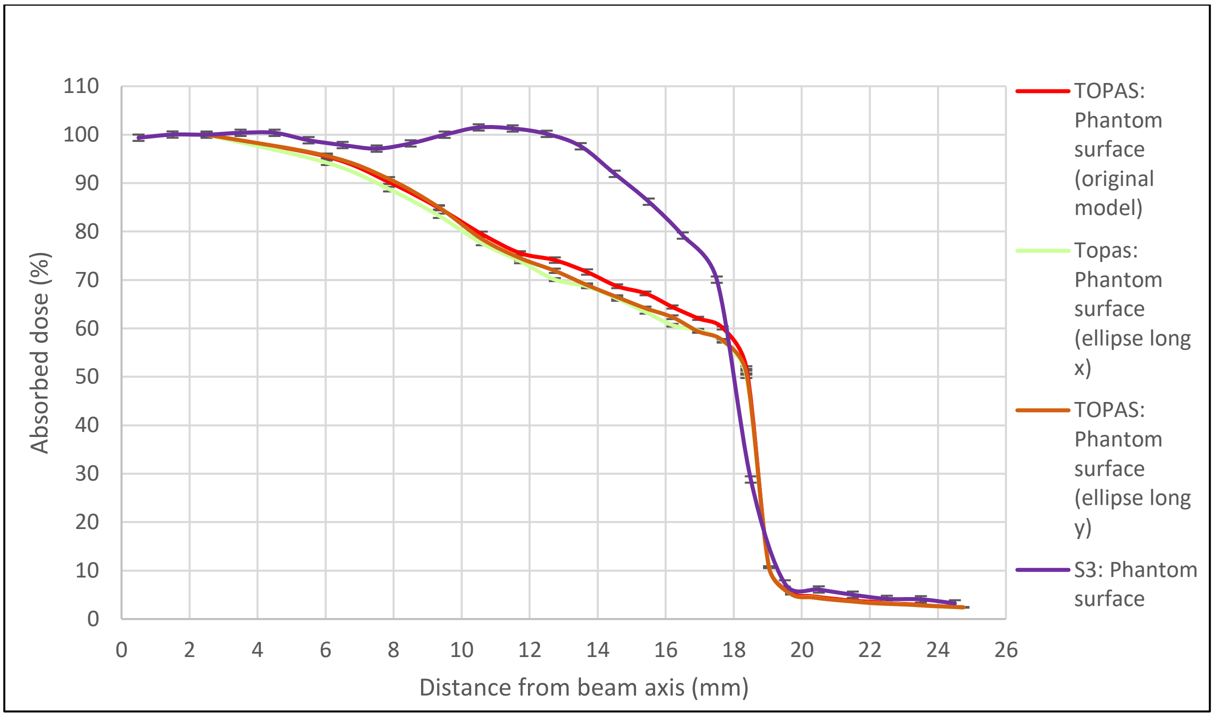

Figure 44: Measured transversal dose profile compared to simulated transversal dose profiles of (1) the original TOPAS MC model and (2) the elliptical beam model, all profiles taken at the phantom surface

Very small differences are noticed between the original model and the elliptical models across all the evaluated radii, but mostly at the edges of the transversal dose profiles. These discrepancies amount to about 3% at most. When comparing the transversal dose profiles of both of the elliptical models with each other, it can be deduced that the differences are negligible as they are mostly confined within the uncertainty intervals represented by the error bars. This is understandable, as a decrease in dose on one axis is compensated by an increase in dose on the other axis due to the radial evaluation of the transversal dose profiles. As a result, the circular electron beam is preserved for the following simulations.

Distribution of electrons in the electron beam

Thirdly, the distribution of the electrons inside the electron beam is altered. Two new models are created which both implement distributions which are Gaussian in nature. The first model implements a Gaussian position distribution of the electrons in the circular beam. This distribution, which is implemented for both the x- and the y-axis has a mean (μ) coinciding with the beam axis and a standard deviation (σ) equal to half the diameter of the circular electron beam. The second model introduces a Gaussian distribution to the angular distribution of the electrons relative to the x- and y-axis. The Gaussian distribution allows for some electrons to traverse the x-ray tube in a non-parallel manner to the electron beam axis, taking into account the coulomb forces exerted by the electrons on each other. The μ of this Gaussian is chosen to be parallel to the beam axis while σ is chosen to be 30°. The cutoff angle in this case is equal to 90° relative to the beam axis. This cutoff angle makes sure that no particles are distributed in unrealistic directions. The results are shown in figure 45.

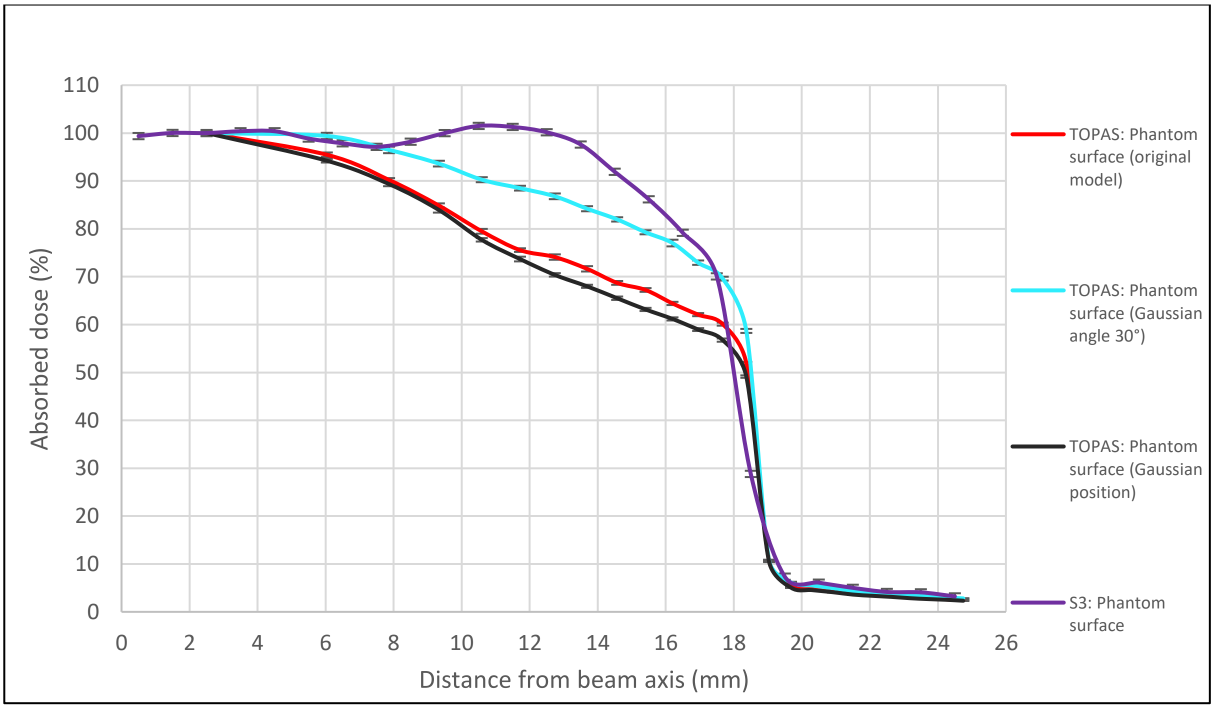

Figure 45: Measured transversal dose profile compared to simulated transversal dose profiles of (1) the original TOPAS MC model and (2) the Gaussian models, all profiles taken at the phantom surface

Small differences are observed on the simulated transversal dose profiles at radii further from the centre when comparing the transversal dose profiles of the original TOPAS MC model and the Gaussian position model. Starting from 0% at 9 mm, these increase to 4% at 15mm. The explanation for this phenomenon is similar to the explanation given for the shape of the simulated transversal dose profiles resulting from the pencil beam model (see figure 43). Indeed, the gaussian position distribution would result in more dose centrally on the axis and a dose drop off on the sides of the profiles. However, only a dose drop off on the sides is registered while the increase of the dose centrally remains absent. Either way, as the objective is to bring the simulated transversal dose profile closer to the measured transversal dose profile, the flat position distribution is maintained.

Regarding the Gaussian angle model, large differences are recorded between the transversal dose profiles across all the evaluated radii, with a maximum of 13.3% at 14.6 mm. Indeed, because of the inclusion of the gaussian angular distribution, an increased number of electrons interact in the outer parts of the target which in turn results in more photons interacting in outer segments of the scorer, increasing the dose in these segments. As such, the difference in absorbed dose between the segments close to the centre and the outer segments decreased, thus increasing the relative dose across the whole profile.

It is clear that the inclusion of a Gaussian angular distribution is a very important step towards the realisation of the final TOPAS MC model. It is however not clear (1) what impact a different standard deviation has on the transversal dose profile and (2) what the ideal standard deviation is for this model. Therefore, new simulations are carried out with standard deviations ranging from 20° up to 90°. The results are visualized in figure 46.

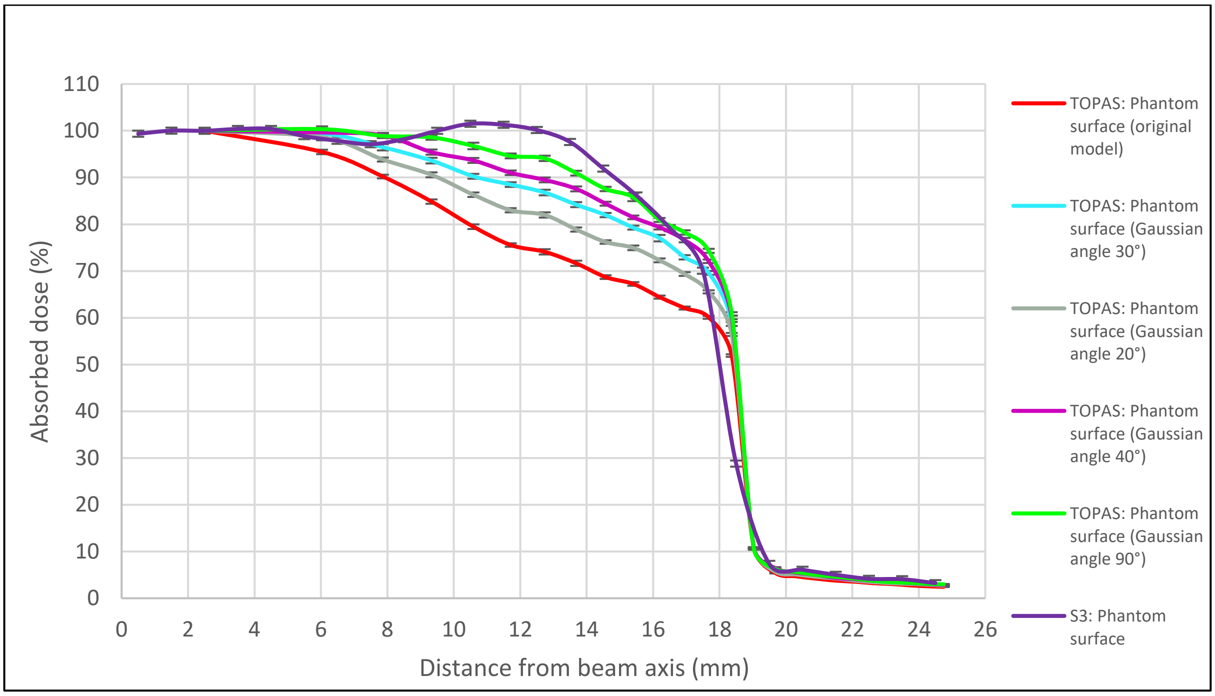

Figure 46: Measured transversal dose profile compared to simulated transversal dose profiles of (1) the original TOPAS MC model and (2) Gaussian angle models with standard deviations of 20°, 30°, 40° and 90°, all profiles taken at the phantom surface

A rise in the standard deviation distinctly leads to an increased dose on the sides of the resulting transversal dose profile, owing to the increased likelihood of electrons interacting in the outer regions of the target. This, in turn, yields a higher dose in the outer segments of the scorer, due to an increase in photon flux. However, the relative increase in dose to the increase in standard deviation strongly decreases as the standard deviation itself increases. This can be observed in Figure 46, where the simulated transversal dose profiles exhibit a decreasing distance between them as the standard deviations increase. Indeed, when the standard deviation reaches very high numbers, the increase in dose is no longer solely due to the effect of the gaussian distribution itself, but more so due to the fact that a lot of electrons simply collide with the edges of the source tip instead of interacting in the target. This strongly inhibits the photons production which flattens out the resulting transversal dose profile.

Even though a high standard deviation of 90° results in a simulated transversal dose profile at the phantom surface which closely resembles the corresponding measured dose profile, it was decided that the electron beam in the model should be kept relatively realistic. As such, the standard deviation is equalled to an acceptable 45°. However, this would still be an overestimation of the standard deviation of the electron beam in a real S700 x-ray tube. Conclusively, the new intermediate model includes a gaussian angular distribution with a standard deviation of 45° combined with the aforementioned alterations.

Particle cutoff

Finally, the particle cutoff is reduced to 1 µm for both electrons and photons. This decision is made based on the hypothesis that some electrons, who in reality would react in deeper parts of the target and produce a photon, are eliminated from the simulation because TOPAS deemed them to lack sufficient energy to traverse 1 mm within the target material. More photons would also reach the scorer, which was however considered to be of lesser significance. To test the influence of the new cutoff on the resulting simulated transversal dose profiles, the most recent version of the model (including the Gaussian distribution of 45°) was compared to one without the cutoff. Figure 47 exhibits the results.

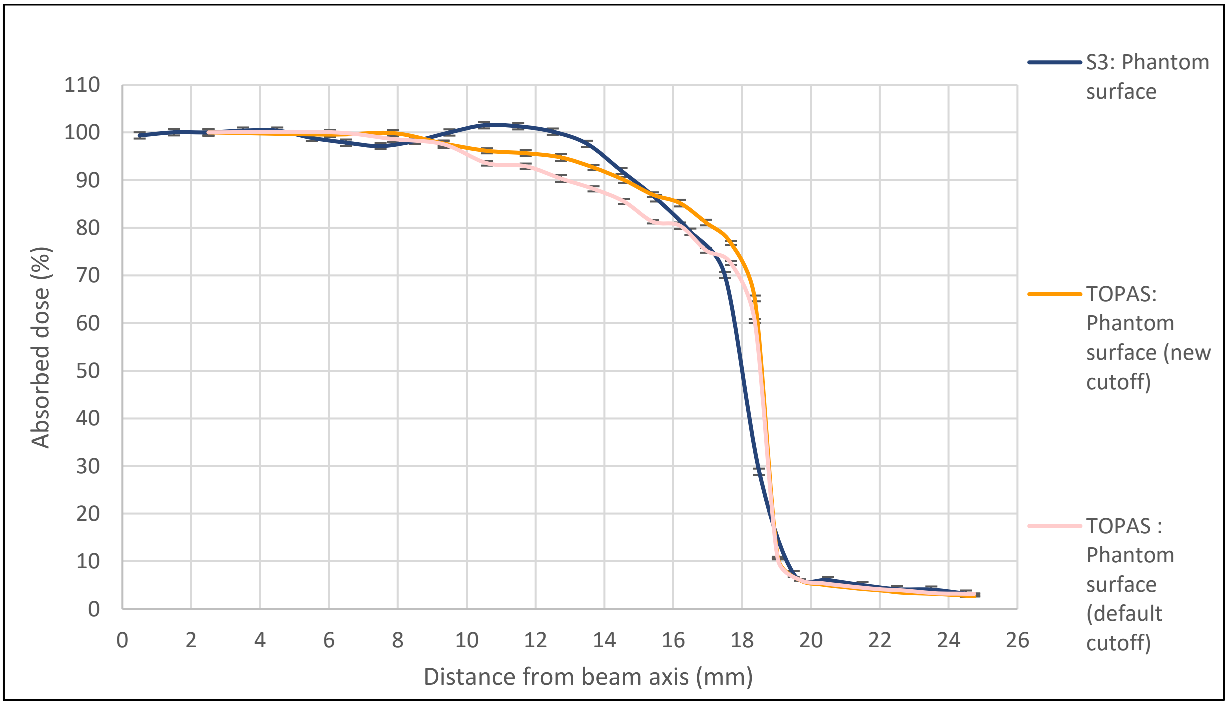

Figure 47: Comparison of simulated transversal dose profiles using the default cutoff and the smaller 1 µm cutoff to the measured transversal dose profiles at the Plastic Water LR phantom surface

As expected, electrons that normally would have been cut out of the simulation are now able to interact in deeper parts of the target, therefore increasing the efficiency of photon production. This, in turn, increases the dose deposited in the scorer. However, from figure 47 it would seem that this adaptation has a higher impact on the dose further away from the beam axis. To make sure that this isn't solely due to the normalisation, the absolute transversal dose profiles are plotted in figure 48, without the usual normalisation.

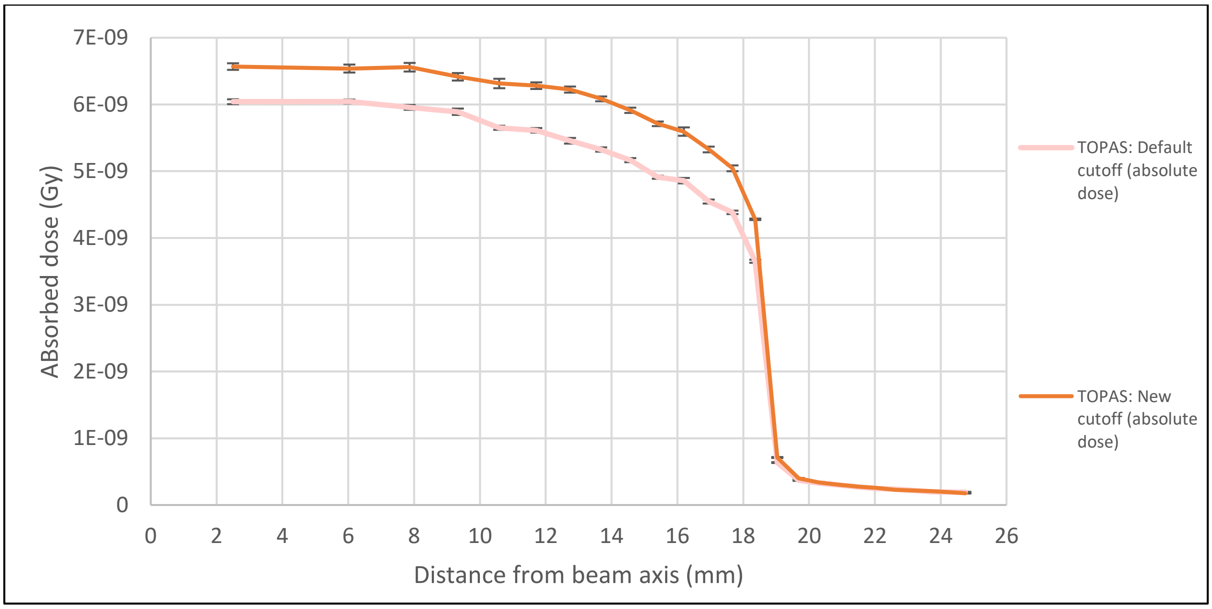

Figure 48: Simulated absolute transversal dose profiles on the phantom surface using the default and the new cutoff

From figure 48, it can be concluded that the enhanced photon generation efficiency leads to an overall increase in absorbed dose across the entire simulated absolute transversal dose profiles. Moreover, the difference in absorbed dose is more or less identical across the whole profile, meaning that the normalisation is indeed the reason for the apparent increase in relative absorbed dose in figure 47. Due to the increased photon generation efficiency and the favourable effect on the relative simulated transversal dose profiles, the new cutoff of 1 µm is added to ultimately bring forth the final TOPAS MC model.

Summary

Table 3 summarizes the effects on the simulated transversal dose profiles by changing several different electron beam parameters of the original TOPAS MC model.

Table 3: Impact of electron beam parameters on transversal dose profiles

Type of change	Used in final model?	Impact(s) on the transversal dose profiles	Comment(s)
Circular electron beam -> elliptical electron beam	No	- Mostly negligible	- Might give different results for linear transversal dose profiles
Smaller electron beam	Yes	- Increase in dose close to beam axis - Decrease in dose on sides of the profile	- Electron beam has to be significantly smaller to induce visible changes on profiles
Flat position distribution -> Gaussian position distribution	No	- Decrease in dose on sides of the profile	/
No angular distribution -> Gaussian angular distribution	Yes	- Increase in dose across the whole profile - Flatter profile	- σ = 45° was chosen for the final model
Smaller particle cutoff	Yes	- increase in absolute dose - increased photon production efficiency	- 1 µm was chosen for the final model

8.2.3 Final Topas MC model

The differences between the electron beam of the final TOPAS MC model and the electron beam of the original TOPAS MC model are (1) the slightly smaller electron beam diameter, (2) the gaussian angular distribution (σ = 45°) and (3) the decreased cutoff distance (1 µm). In each of the following figures the simulated transversal dose profiles, which were generated by the original TOPAS MC model as well as the final TOPAS MC model, were compared among themselves and to the measured transversal dose profiles. Figure 49, figure 50 and figure 51 show the results in air, on top of the Plastic Water LR phantom, and at 1 cm depth inside the phantom. As before, table 4 and 5 show the calculated beam flatness for the first two setups. The simulated transversal dose profiles using the final TOPAS MC model were generated using $1 * 10^9$ histories to further minimize the uncertainty on the profiles.

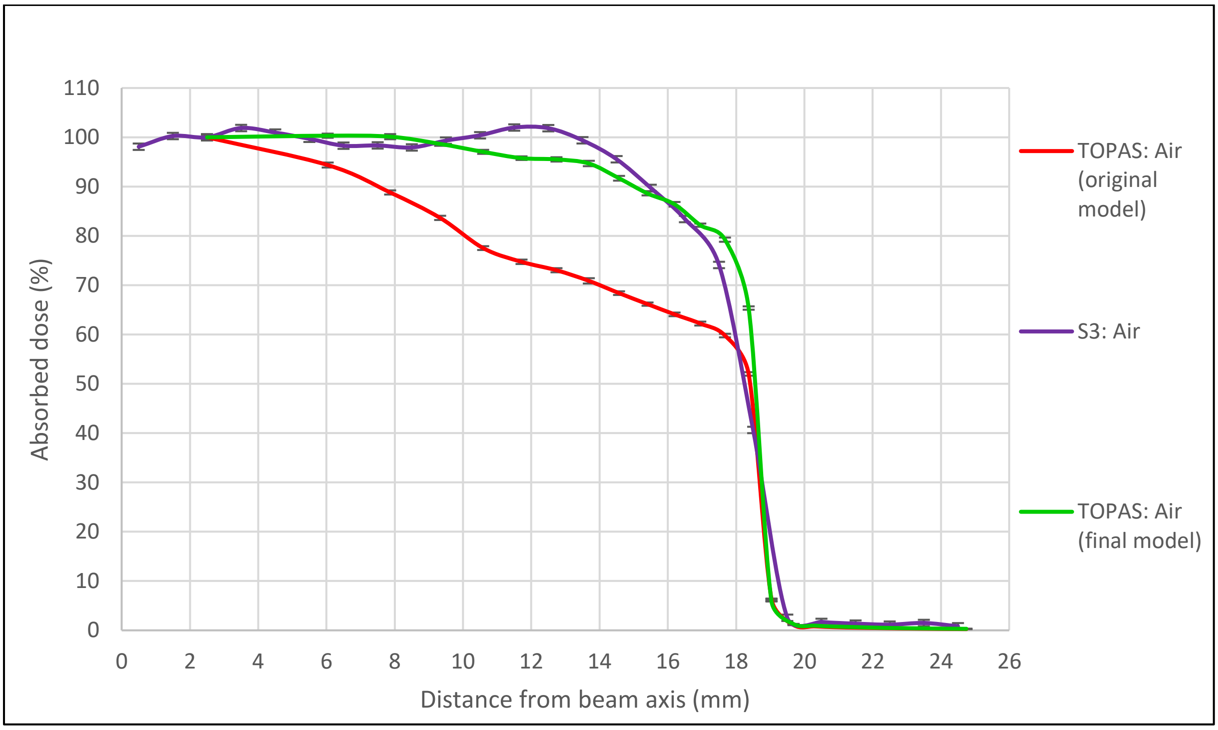

Figure 49: Measured and simulated (final TOPAS MC model) transversal dose profiles in air

Table 4: Beam flatness calculated for the measured and simulated (final TOPAS MC model) transversal dose profiles in air

Type of transversal dose profile	D_{max} (%)	D_{min} (%)	beam flatness F (%)
Measured	102.0	97.9	2.0
Simulated: Original model	100.0	70.9	17.0
Simulated: Original model	100.8	90.6	5.4

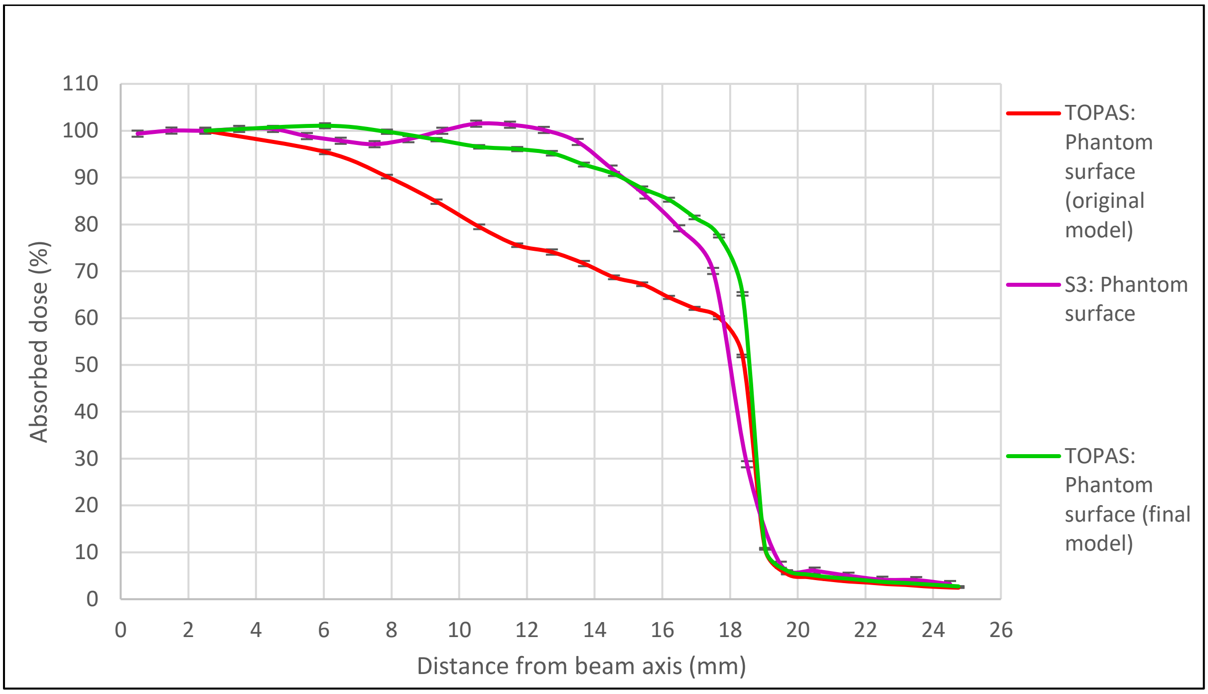

Figure 50: Measured and simulated (final TOPAS MC model) transversal dose profiles on the phantom surface

Table 5: Beam flatness calculated for the measured and simulated (final TOPAS MC model) transversal dose profiles on the phantom surface

Type of transversal dose profile	D_{max} (%)	D_{min} (%)	beam flatness F (%)
Measured	101.5	97.1	2.2
Simulated: Original model	100.0	71.6	16.5
Simulated: Original model	100.0	89.4	5.6

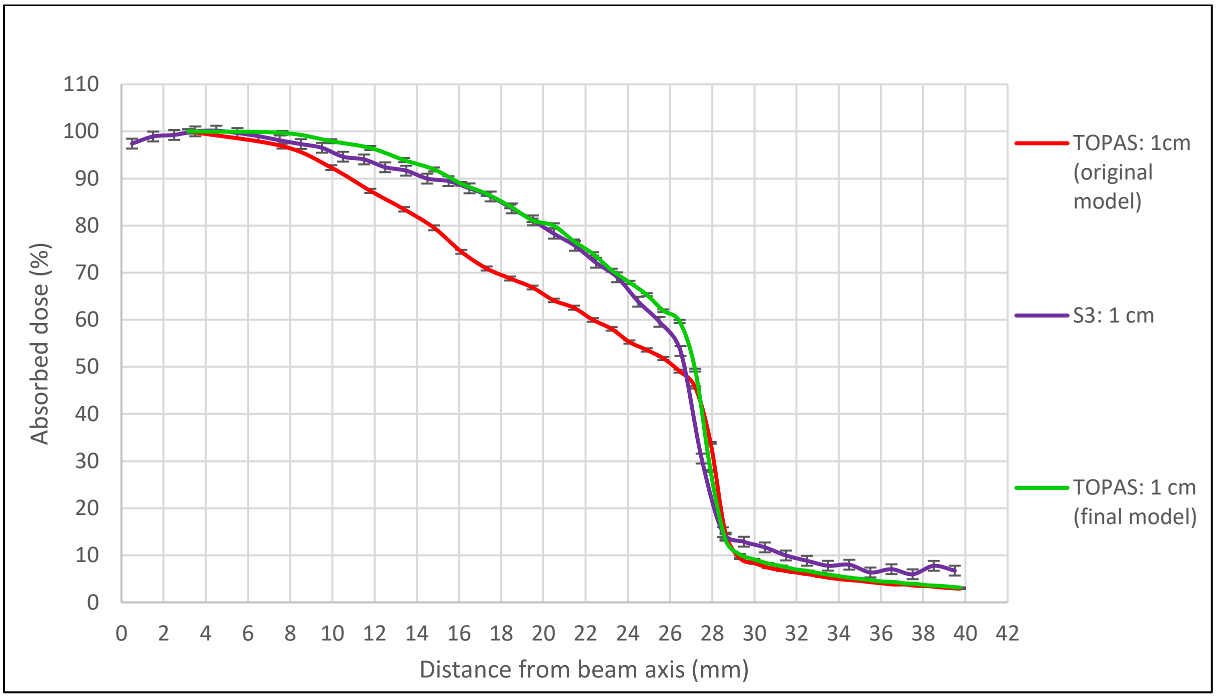

Figure 51: Measured and simulated (final TOPAS MC model) transversal dose profiles at 1 cm depth in the phantom

When comparing the simulated transversal dose profiles of the final TOPAS MC model to those of the original TOPAS MC model, it can be deducted that there is a significant increase in dose on the sides of the profiles. As a result, the maximal differences between corresponding simulated transversal dose profiles (final TOPAS MC model) and measured transversal dose profiles are well within the prescribed limit of 10%. These maximal differences equate to 6.3% at 12.5 mm in air, 5.0% at 11.7 mm on the Plastic Water LR phantom surface, and 3.0% at 12.5 mm at 1 cm depth inside the phantom. The disparity between the beam flatness of the measured and simulated transversal dose profiles in air and on the phantom surface decreased accordingly to 3.4% for both of these setups.

9 General discussion, shortcomings & future work

From the measured transversal dose profiles, it could be concluded that there are significant differences between the dose output of the four non-clinical S700 sources. As a result, the electron beams inside these sources varied accordingly. This aligns with the statements made in section 7.2.3. As mentioned in this section, the design of the electron beam is influenced by several variables, and therefore the electron beam can differ considerably from source to source due to slight variations in the internal structure and specifications. This is especially the case for the miniaturized x-ray sources like the S700 source, considering the very small dimensions of this source. The flattest transversal dose profiles were recorded using the S/N 960258 source (S3), which were hereafter compared to simulated transversal dose profiles, generated using the original TOPAS MC model. As a result, significant discrepancies (larger than 10%) were found between the three pairs of transversal dose profiles, measured in air, on the surface of the Plastic Water LR phantom and at 1 cm depth inside this phantom. In particular, the measured transversal dose profiles in air and on the phantom surface displayed a horn on the profile where the simulated dose profiles displayed a radial dose drop off.

Regarding the impact of the electron beam parameters, it was realised that a smaller electron beam resulted in more dose centrally on the simulated transversal dose profile at the cost of less dose on the sides of the profile. This is an indirect result of confining the electrons in a smaller beam diameter, as a smaller electron beam would result in a smaller photon beam. Changing the shape of the electron beam to an elliptical shape did however not have any significant influence, mostly due to the fact that the transversal dose profiles were evaluated radially. Similarly to a smaller electron beam, the instigation of a Gaussian position distribution resulted in less photons on the sides of the simulated transversal dose profiles, which were in indirect result of the fact that the majority of electrons were concentrated in the middle of the electron beam. A Gaussian angular distribution however resulted in some electrons deviating from the beam axis of the electron beam, which in turn resulted in more photons on the sides of the profile and therefore an off-axis dose increase on the simulated transversal dose profiles. finally, a smaller particle cutoff resulted in some electrons, who would normally be eliminated, interacting in deeper layers of the target. This increased the efficiency of photon production and therefore the absolute absorbed dose on the simulated transversal dose profiles. All of these findings were summarized in table 3. In the final TOPAS MC model, these findings were considered for the design of the electron beam. This final TOPAS MC model generated transversal dose profiles with maximal differences within 10%. However, the horns, which were discernible on the measured transversal dose profiles, were never reproduced on the simulated transversal dose profiles. Finally, the simulated transversal dose profiles had a steeper dose drop off than the measured transversal dose profiles. It is however expected that this phenomenon is not related to a mistake in the design of the TOPAS MC model, but rather to the acquirement of the data points. This is discussed further in the list of shortcomings below.

There are a few shortcomings of this thesis which need to be considered, as they could potentially have an impact on the validity of the results. Firstly, it was particularly difficult to make sure that the film was orthogonal to the beam axis using the existing wooden holders. Even though measurements were taken with the utmost care, errors could still have been introduced on the measured transversal dose profiles. Secondly, the S700 sources used in this thesis are all non-clinical sources, which means that they are on average less uniform than clinical sources. This worsened the variety in design of electron beams when comparing different sources. In addition, the S700 is very small which further exacerbates this problem, as its manufacturing is particularly difficult. On the contrary, the geometry of the XOFT eBx System in TOPAS was constructed using STL files representing the ideal situation. Furthermore, the geometry was not adaptable as the associated STL files could not be adapted manually and there was also no information available on the manufacturing method of different parts, like, for example, the flattening filter. This leads to the conclusion that the simulated transversal dose profiles resulted from an ideal situation which was very hard, if not impossible, to attain in reality. Thirdly, it should be considered that the transversal dose profiles did not contain measurements on, and very close to, the beam axis. This was attributable to the process used to gather the data points. Finally, although these data points roughly use the same intervals, it must be considered that the measured and simulated data points are not accumulated using the same procedure. The simulated data points are the result of a summation of the absorbed dose at a certain radius away from the beam axis, but in actuality this summed absorbed in a segment of the scorer dose is a result of photons striking the whole area of this segment, and not just the evaluated radius. As such, the surrounding points in the same segment are indirectly accounted for, which gives a more precise image about the dose drop off at the edges of the transversal dose profiles, and therefore a more steep dose drop off. Conversely, the measured data points consist of absorbed dose which is only measured at fixed radii. As such, the measured transversal dose profiles lack data required to accurately image the steep dose drop off. Instead, excel connects these data points using linear interpolation, which flattens out this drop off. This problem is worse for the setups in air and on the phantom surface compared to the setup at 1 cm depth, because the transversal dose profile at 1 cm already has a flatter dose drop of on the transversal dose profile due to the scattering of the photons in the phantom.

Future work could be focused on these shortcomings. As such, new holders could be 3D printed to ensure that the EBT3 films were positioned orthogonally to the beam axis. In the case that a clinical source could be acquired, transversal dose profiles could be measured and compared to the simulated transversal dose profile using the final TOPAS MC model to conclude whether this model could be used to validate clinical sources. Additionally, new transversal dose profiles could be plotted which evaluate the dose on, and very close to, the beam axis. However, considering that the model was previously validated for PDD measurements on the beam axis, this may be futile. These new profiles would preferably also contain more data points to accurately create the steep dose drop of. Furthermore, new STL files could be imported with different dimensions which would allow, for example, to characterize the impact of different thicknesses of the flattening filter on the simulated transversal dose profiles and PDD curve. However, this would likely require alterations on several different parts of the geometry of the XOFT eBx System. This would be very challenging and would most likely require close cooperation with XOFT, inc. themselves. Another step further would be to try to change the geometry and dimensions of components of the XOFT eBx System and document the associated transversal dose profiles and PDD curves. By aligning the measured and simulated data, this would in theory allow the researcher to create a mirror image of the real XOFT eBx System and the S700 source by reverse engineering. Finally, new transversal dose profiles could be plotted which evaluate the dose on, and very close to, the beam axis. However, considering that the model was previously validated for PDD measurements on the beam axis, this may be futile.

10 Conclusion

This thesis is the latest addition to the series of theses which are dedicated to the evaluation of the dose output of the XOFT Accent electronic brachytherapy (eBx) System. Indeed, in earlier theses, (1) the gamma spectrum was assessed, (2) a virtual model was created using the MC tool TOPAS and (3) this model was validated for the prediction of PDD curves. In this thesis, this original TOPAS MC model was optimized to generate simulated transversal dose profiles that are within 10% with the corresponding measured transversal dose profiles. Also, the optimal collection of electron beam design parameters were documented together with the impact of adaptations of these parameters on the simulated transversal dose profiles.

Transversal dose profiles specific to the XOFT eBx System, equipped with the S700 source and a 35 mm conical applicator, were evaluated in three different setups: (1) in air, (2) on the surface of a 10x10x4 cm Plastic Water LR phantom, and (3) at 1 cm depth inside this phantom. EBT3 films were employed to measure the transversal dose profiles while the simulated transversal dose profiles were generated using the original TOPAS (version 3.8) MC model. The corresponding transversal dose profiles from each setup were then compared. This initially resulted in maximal discrepancies of 28.4% in air, 25.7% on the phantom surface and 15.8% at 1 cm depth inside this phantom. To close these gaps, the original TOPAS MC model had to be optimized. This was a step-wise process in which electron beam parameters pertaining to the size, shape, distribution and cutoff of the aforementioned electron beam were sequentially changed and then related to changes on the simulated transversal dose profiles. These findings were hereafter (1) summarized in table 3 and (2) used to construct the final TOPAS MC model. This final model contained a circular electron beam with a diameter of 1.596944 mm and a Gaussian angular distribution of the electrons, with a mean (µ) of 0° and a standard deviation (σ) of 45°, measured relative to the beam axis. Also, the cutoff threshold of the particles was decreased from 1 mm to 1 µm. Using this final TOPAS MC model, the discrepancies between the measured dose profiles decreased to 6.3% in air, 5.0% on the phantom surface, and 3% at 1 cm depth inside the phantom. Since these discrepancies were well contained in the proposed interval of 10%, the final TOPAS MC model was validated for transversal dose profiles.

Sources

[1] NHS, “Cancer,” 13 10 2022. [Online]. Available: https://www.nhs.uk/conditions/cancer/. [Accessed 4 Oktober 2022].

[2] International Agency for Research on Cancer, “PRESS RELEASE N° 223,” nternational Agency for Research on Cancer, Lyons, 2013.

[3] International Agency for Research on Cancer, “PRESS RELEASE N°263,” International Agency for Research on Cancer, Lyons, 2018.

[4] B. Rajamanickam, L. Kuo Ann, Y. Richard and Y. Kheng-Wei, “Cancer and Radiation Therapy: Current Advances and Future Directions,” *International Journal of Medical Sciences,* vol. 9, no. 3, pp. 193-199, 2012.

[5] G. Delaney, S. Jacob and C. Featherstone, “The role of radiotherapy in cancer treatment: Estimating optimal utilization from a review of evidence-based clinical guidelines,” *cancer,* vol. 104, no. 6, pp. 1129-1137, 2005.

[6] B. A. Tisdale, “When to Consider Radiation Therapy for Your Patient,” *American Academy of Family Physicians,* vol. 59, no. 5, pp. 1177-1184, 1999.

[7] Canadian Cancer Society, “Side effects of radiation therapy,” Canadian Cancer Society, [Online]. Available: https://cancer.ca/en/treatments/treatment-types/radiation-therapy/side-effects-of-radiation-therapy. [Accessed 8 June 2023].

[8] J. Skowronek, “Current status of brachytherapy in cancer treatment,” *Journal of Contemporary Brachytherapy,* vol. 9, no. 6, pp. 591-589, 2017.

[9] Wiktionary, “brachytherapy,” [Online]. Available: https://en.wiktionary.org/wiki/brachytherapy. [Accessed 10 11 2022].

[10] BXTA, “Seeds,” [Online]. Available: https://bxta.com/uk/healthcare-professionals/seeds/. [Accessed 17 Oktober 2022].

[11] Faculty of Radiation Oncology of the Royal Australian and New Zealand College of Radiologists, “Brachytherapy,” 11 September 2020. [Online]. Available: https://www.targetingcancer.com.au/radiation-therapy/brachytherapy/. [Accessed 17 Oktober 2022].

[12] J. Skowronek, “Brachytherapy in the treatment of skin cancer: an overview,” *Postep Derm Alergol,* vol. 32, no. 5, pp. 362-367, 2015.

[13] D. G. Petereit, S. J. Frank, A. N. Viswanathan, B. Erickson, P. Eifel, P. L. Nguyen and D. E. Wazer, “Brachytherapy: Where Has It Gone?,” *Journal of Clinical Oncology,* vol. 33, no. 9, pp. 980-982, 2015.

[14] C. Van de Voorde *et al.*, “Required hospital capacity in 2025 and criteria for rationalisation of complex cancer surgery, radiotherapy and maternity services,” *KCE Reports,* vol. 289, no. 1, pp. 1-110, 2017.

[15] C. Salembier, O. De Hertogh, J.-F. Daisne and D. Van Gestel, “Brachytherapy in Belgium in 2018. A national survey of the brachytherapy study group of the Belgian SocieTy for Radiotherapy and Oncology (BeSTRO),” *Radiotherapy and Oncology,* vol. 150, no. 1, p. 245–252, 2020.

[16] U. Mahmood, T. Pugh, S. Frank, L. Lawrence, G. Walker, W. Haque, M. Koshy, W. Graber, D. Swanson, K. Hoffman, D. Kuban and A. Lee, “Declining use of brachytherapy for the treatment of prostate cancer,” *Brachytherapy,* vol. 13, no. 2, pp. 157-162, 2014.

[17] B. Gill, J. Lin, T. Krivak, P. Sukumvanich, R. Laskey, M. Ross, J. Lesnock and S. Beriwal, “National Cancer Data Base Analysis of Radiation Therapy Consolidation Modality for Cervical Cancer: The Impact of New Technological Advancement,” *International Journal of Radiation Oncology*Biology*Physics,* vol. 90, no. 5, pp. 1083-1090, 2014.

[18] D. M. C. Liu, Characterization of novel electronic brachytherapy system [eindwerk], Montreal: Medical Physics Unit McGill University, 2007.

[19] P. Ramachandran, “New era of electronic brachytherapy,” *World Journal of Radiology,* vol. 9, no. 4, pp. 148-154, 2017.

[20] N. H. Khan *et al.*, “Skin cancer biology and barriers to treatment: Recent applications of polymeric micro/nanostructures,” *Journal of Advanced Research,* vol. 36, no. 1, pp. 223-247, 2022.

[21] American Cancer Society, “Survival Rates for Melanoma Skin Cancer,” American Cancer Society, 1 March 2023. [Online]. Available: https://www.cancer.org/cancer/melanoma-skin-cancer/detection-diagnosis-staging/survival-rates-for-melanoma-skin-cancer-by-stage.html. [Accessed 8 June 2023].

[22] SkinCancer.net, “Why Don't We Treat Melanoma with SRT?,” 8 January 2022. [Online]. Available: https://skincancer.net/clinical/radiation-melanoma. [Accessed 16 Oktober 2022].

[23] Canadian Cancer Society, “Survival statistics for non-melanoma skin cancer,” [Online]. Available: https://cancer.ca/en/cancer-information/cancer-types/skin-non-melanoma/prognosis-and-survival/survival-statistics#:~:text=Survival%20for%20most%20non%2Dmelanoma,people%20in%20the%20general%20population.. [Accessed 11 Oktober 2022].

[24] L. G. Liezel, F. Rehman Ali and J. T. Lear, “Non-melanoma skin cancer,” *Clinical Medicine,* vol. 16, no. 1, pp. 62-65, 2016.

[25] M. Wieme, Characterisation of an electronic brachytherapy source using measurements and Monte Carlo simulations [eindwerk], Maastricht: Maastro, 2020.

[26] S. Arits, Creation and validation of a Monte Carlo model of a superficial electronic brachytherapy system [eindwerk], Diepenbeek: Gezamenlijke opleiding Industriële Ingenieurswetenschappen UHasselt & KU Leuven, 2020.

[27] R. Behling, Modern Diagnostic X-Ray Sources: Technology, Manufacturing, Reliability, Boca Raton: CRC Press, 2021.

[28] chemeurope, “thermionic emission,” [Online]. Available: https://www.chemeurope.com/en/encyclopedia/Thermionic_emission.html. [Accessed 2022 Oktober 19].

[29] E. B. Podgorsak, Radiation Oncology Physics: a handbook for teachers and students, Vienna: International Atomic Energy Agency, 2005.

[30] J. E. Martin, Physics for radiation protection, Weinheim: Wiley-VCH, 2013.

[31] Encyclopaedia Britannica, “tungsten chemical eliment,” 18 November 2022. [Online]. Available: https://www.britannica.com/science/tungsten-chemical-element. [Accessed 22 November 2022].

[32] Werth, “X-RAY SOURCE – 2,” [Online]. Available: https://werthinc.com/x-ray-source-2/#:~:text=X%2Dray%20tubes%20with%20transmission,a%20higher%20resolution%20is%20achievable.. [Accessed 22 Oktober 2022].

[33] S. Wang et al., “Respective radiation output characteristics of transmission-target and reflection-target X-ray tubes with the same beam quality,” *Radiation Physics and Chemistry,* vol. 158, no. 1, pp. 188-193, 2019.

[34] M. J. Rivard, S. D. Davis, L. A. DeWerd, T. W. Rusch and S. Axelrod, “Calculated and measured brachytherapy dosimetry parameters in water for the Xoft Axxent X-Ray Source: An electronic brachytherapy source,” *Medical Physics,* vol. 33, no. 11, pp. 4020-4032, 2006.

[35] R. K. Fulkerson, J. A. Micka and L. A. DeWerd, “Dosimetric characterization and output verification for conical brachytherapy surface applicators. Part I. Electronic brachytherapy source,” *Medical Physics,* vol. 41, no. 2, pp. 1-21, 2014.

[36] R. K. Fulkerson *et al*., “Surface brachytherapy: Joint report of the AAPM and the GEC-ESTRO Task,” *Medical Physics,* vol. 47, no. 10, pp. e951-e987, 2020.

[37] Xoft, inc., Axxent® Electronic Brachytherapy System® Operator Manual, San José: Xoft inc., 2009.

[38] S. Devic, N. Tomic and D. Lewis, “Reference radiochromic film dosimetry: Review of technical aspects,” *Physica Medica,* vol. 32, no. 4, pp. 541-556, 2016.

[39] J. Sorriaux, A. Kacperek, S. Rossomme, J. A. Lee, D. Bertrand, S. Vynckier and E. Sterpin, “Evaluation of Gafchromic® EBT3 films characteristics in therapy photon, electron and proton beams,” *Physica Medica,* vol. 29, no. 6, pp. 599-606, 2013.

[40] M. J. Williams and P. E. Metcalfe, “Radiochromic Film Dosimetry and its Applications in Radiotherapy,” *FACULTY OF ENGINEERING - PAPERS (ARCHIVE),* vol. 1, no. 1, pp. 75-99, 2011.

[41] J. Perl, J. Shin, J. Schumann, B. Faddegon and H. Paganetti, “TOPAS: An innovative proton Monte Carlo platform for research and clinical applications,” *Medical Physics,* vol. 39, no. 11, pp. 6818-6837, 2012.

[42] S. Agostinelli *et al*., “Geant4—a simulation toolkit,” *Nuclear Instruments and Methods in Physics Research,* vol. 506, no. 3, pp. 250-303, 2003.

[43] F. Verhaegen and E. Poon, “Accuracy of the photon and electron physics in GEANT4 for radiotherapy applications,” *Medical Physics,* vol. 32, no. 6, pp. 1696 - 1711, 2005.

[44] L. Pandola, C. Andenna and B. Caccia, “Validation of the Geant4 simulation of bremsstrahlung from thick targets below 3 MeV,” *Nuclear Instruments and Methods in Physics Research B,* vol. 350, no. 1, pp. 41-48, 2015.

[45] B. Faddegon, J. Ramos-Mendez, J. Schuemann, M. A, J. Shin and H. Paganetti, “The TOPAS Tool for Particle Simulation, a Monte Carlo Simulation Tool for Physics, Biology and Clinical Research,” *Physica medica,* vol. 72, no. 1, p. 114–121, 2020.

[46] J. Tyson, “How Scanners Work,” HowStuffWorks, 21 March 2001. [Online]. Available: https://computer.howstuffworks.com/scanner.htm. [Accessed 15 December 2022].

[47] TOPAS MC Inc., “TOPAS Documentation: Release 3.8,” TOPAS MC Inc., San Francisco, 2022.

[48] F. Berumen, Y. Ma, J. Ramos-Méndez, J. Perl and Beaulieu, “Validation of the TOPAS Monte Carlo toolkit for HDR brachytherapy,” *Brachytherapy,* vol. 20, no. 4, pp. 911-921, 2021.

[49] J. Jones, “Focal spot,” radiopaedia, 18 September 2021. [Online]. Available: https://radiopaedia.org/articles/focal-spot#:~:text=Focal%20spot%20is%20the%20area,apparent%20source%20of%20x%2Drays.. [Accessed 8 June 2023].

[50] V. B. Nuculaes *et al*., “Design and characterization of electron beam focusing for X-ray generation in novel medical imaging architecture,” *Physics of Plasmas,* vol. 21, no. 5, pp. 1-9, 2014.

[51] R. Nath *et al*., “AAPM code of practice for radiotherapy accelerators: Report of AAPM Radiation Therapy Task Group No. 45,” *Medical Physics,* vol. 21, no. 7, pp. 1031-1215, 1994.

[52] X. Shao and A. Khurseed, “A Review Paper on “Graphene Field Emission for Electron Microscopy",” *applied sciences,* vol. 8, no. 6, p. 868, 2018.

[53] P. Ramachandran, D. Wanigaratne, J. Hagekrykou, M. Geso and S. David, “Brachytherapy utilising miniaturised X-ray tubes – clinical implementation and future applications,” *Journal of Physics: Conference Series,* vol. 1154, no. 1, pp. 1-6, 2019.

[54] R. A. Weersink *et al*., “Integration of optical imaging with a small animal irradiator,” *Medical Physics,* vol. 41, no. 10, pp. 1-13, 2014.

[55] K. S. Krane, Introductory Nuclear Physics, Oregon: John Wiley & Sons, 1991.

Appendix

Appendix A: The X-ray tube

Production of electrons

The emission current density J ($\frac{\mathrm{A}}{\mathrm{m}^2}$) of the heated cathode filament is proportional to the temperature of the filament [27, 28]. Formula 17 describes this relationship.

$$J = A * T^2 * e^{\frac{-W}{k*T}} \tag{17}$$

In formula 17, T is the temperature of the filament (°K), W is the work function, k is the Boltzmann constant and finally A is the Richardson's constant. The Richardson's constant A itself is calculated according to formula 18. In practice however, the Richardson's constant is firmly correlated to the material of the filament [28].

$$A = \frac{4 * \pi * m * k^2 * e}{h^3} = 1.20173 * 10^6 \frac{A}{m^2 * K^2} \tag{18}$$

In formula 18, m represents the rest mass of an electron (kg) , e represents the charge of an electron (eV) and the Planck's constant is defined by h.

A second option is to emit electrons using field emission. This technique entails that electrons have a non-zero chance to tunnel through a solid surface to the vacuum using a high local static electric field [52]. One of the more prominent examples are the carbon nanotube (CNT) field emitters [52]. The principle of field emission has to be approached using quantum-mechanics and is too complex to cover in this thesis completely. For more info on this subject, [52] can be consulted.

Energy groups of x-ray beams

When the electrons are emitted from the emitter, they are accelerated from the cathode to the target anode by an electric field and the electron beam is focused on this target anode by focusing electrodes. Depending on the strength of the electric field the electrons are typically accelerated to kinetic energies ranging from 10 keV to 50 MeV, thereby producing X-ray beams ranging from 10 kVp to 50 MV [29]. In practice, x-ray beams are grouped in 3 different categories depending on their energy. Firstly, there are superficial x-rays, ranging from 10 keV to 100 keV. X-rays produced by x-ray tubes in EBT are also included in this group, as most of these x-ray tubes operate at tube voltages between 50 kVp and 100 kVp [53]. Secondly, there are orthogonal x-ray beams ranging from 100 keV to 500 keV. Lastly, beams with energies above 1 MV are aptly named megavoltage x-ray beams [29]. Superficial x-ray beams and orthogonal x-ray beams can be produced using x-ray tubes. Megavoltage x-ray beams are only included in this section for completeness since these x-rays are not produced using x-ray tubes but with specialized equipment such as linear accelerators and microtrons [29].

Model for the interactions of electrons in matter

How an incident electrons interacts with the target is highly dependent on the distance of the electron to the nucleus of a target atom [29]. In figure 52, this distance is portrayed by the parameter b. The parameter a is the radius of the target atom. If b >> a then the electron will undergo a soft collision with the whole atom. In this case, only a very small portion of the energy of the incident electron will be transferred to orbital electrons. When $b \approx a$, the electron will undergo a hard collision with an orbital electron where a significant amount of energy will be transferred from the incident electron to the orbital electron that was struck. Finally, when b >> a the incident electron undergoes a radiative interaction with the target nucleus. This interaction results in the emission of a photon by the incident electron. The energy of this photon ranges from zero to the energy of the incident electron. Moreover, the energy of the photon will increase as b decreases. This process is called bremsstrahlung.

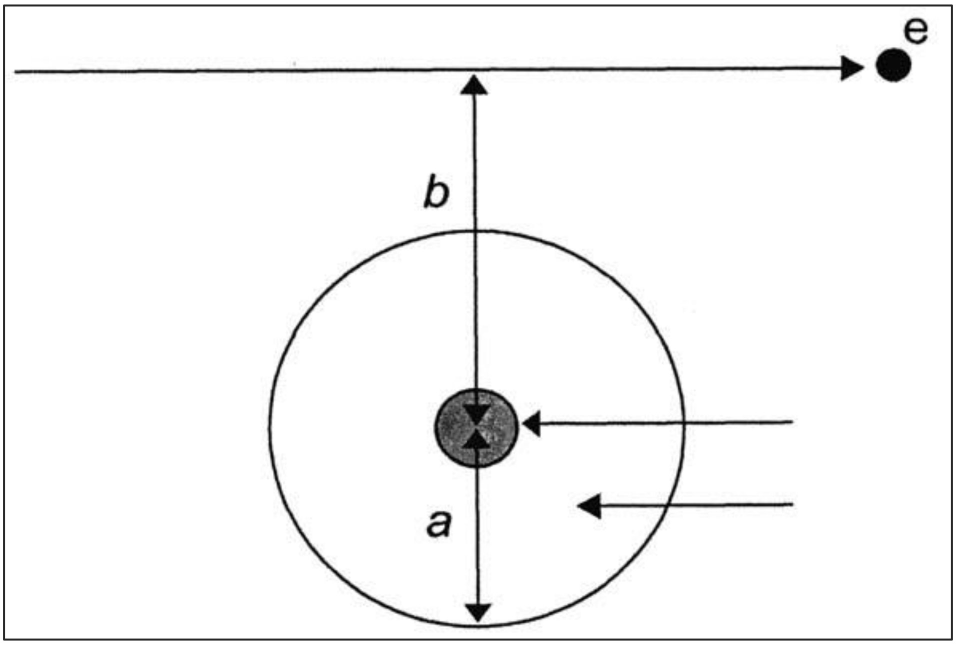

Figure 52: Interactions of electrons in matter [29, p. 22]

Using this model, the total stopping power $\mathrm{S_{tot}}$ can be divided into 2 parts [29]. The collision stopping power $\mathrm{S_{col}}$ governs energy losses correlated to coulomb interactions between the incident electron and orbital electrons resulting in ionization or excitation of the target atom. The energy losses related to bremsstrahlung are characterized by the radiative stopping power $\mathrm{S_{rad}}$ [29]. The total stopping power can be calculated using formula 1, which was visualised and explained in section 2.2. Similarly, the mass stopping power $\left(\frac{\mathrm{S}}{\rho}\right)_{\mathrm{tot}}$, which signifies the ratio of the total stopping power to the density ρ of the target, is calculated using formula 2.

For free electrons the energy transfers due to soft collisions can be combined with those of hard collisions using the Møller cross-sections [26]. Incorporation into the Bethe-Bloch formula results in formula 19 to calculate the mass collisional stopping power.

$$\left(\frac{S}{\rho}\right)_{col} = \frac{N_A Z}{A} * \frac{\pi r_e^2 2 m_e c^2}{\beta^2}\left[\ln\left(\frac{E_K}{I}\right)^2 + \ln\left(1+\frac{\tau}{2}\right) + F^-(\tau) - \delta\right] \tag{19}$$

In formula 18, $\mathrm{N_A}$ is the Avogadro number, A is the atomic mass number, Z is the atomic number, $\mathrm{r_e}$ is the classical electron radius (m), $\mathrm{m_e c^2}$ is the rest energy of an electron(eV) , β is the ratio of the velocity of the electron v and the velocity of light c, I is the mean excitation energy (eV), τ is the ratio of the kinetic energy $\mathrm{E_K}$ to the rest energy of an electron $\mathrm{m_e c^2}$, and δ is a term used to correct for the density effect. The function $\mathrm{F^-(\tau)}$ for electrons can be found using formula 20.

$$F^-(\tau) = (1-\beta^2) * \left[1 + \frac{\tau^2}{8} - (2\tau + 1) * \ln 2\right] \tag{20}$$

Contrariwise, the mass radiative stopping power on the other hand is calculated using formula 21, which is known as the Bethe-Heitler formula for electrons [29].

$$\left(\frac{S}{\rho}\right)_{rad} = \sigma_0 * \frac{N_A Z^2}{A} * (E_K + m_e c^2) * \bar{B}_r \tag{21}$$

In formula 21, $\overline{\mathrm{B}}_{\mathrm{r}}$ is a function of Z and E_{K}, while σ is another constant which is calculated using formula 22. In this formula α represents the fine structure constant.

$$\sigma = \alpha * \left(\frac{e^2}{4\pi e_0 m_e c^2}\right)^2 = 5.80 * 10^{-28} \frac{cm^2}{atom} \tag{22}$$

Appendix B: Calibration of the EBT3 films & associated apparatus

As mentioned in section 7.1.2, calibration curves were used to convert the OD on EBT3 films to the absorbed dose. These calibration curves were constructed on 19/12/2022. The irradiations were carried out using the X-Rad Small Animal Radiation Therapy device type 225Cx, operating at 60 kVp. The schematic representation of this device, which is often used for radiation biology research on small animals, is visualised in figure 53 [26, 54].

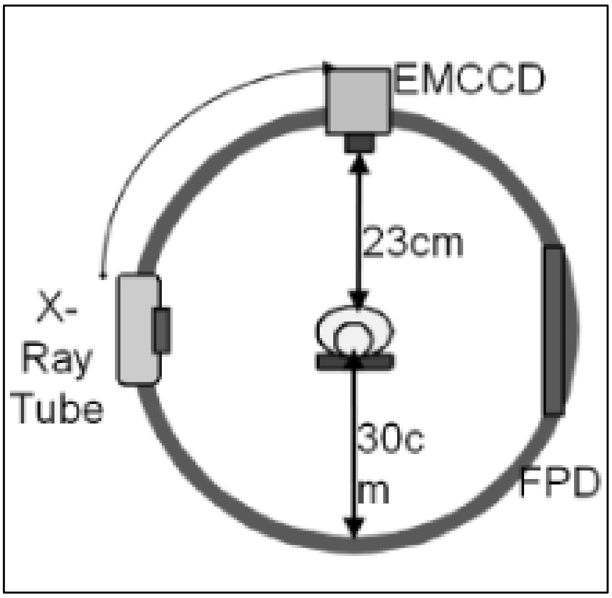

Figure 53: schematic representation of the X-Rad Small Animal Radiation Therapy device type 225Cx [54, p.2]

In accordance with figure 53, the device was fitted with an x-ray tube, a flat panel detector for cone beam Computed tomography (CT) imaging and a Electron Multiplying Charge-Coupled Device (EMCCD) camera which can provide accurate, real-time images during irradiation [54]. These were all secured to a c-arm gantry and secured inside a shielding box. During a general irradiation of an animal, the c-arm would rotate around the central bench upon which the small animal was restrained. However, for the calibrations, the c-arm gantry was stationary above the bench.

The first step for the construction of the calibration curves was the calculation of the dose rate at the surface of a water phantom which was located on the bench. The dose rate was calculated according to TG-61 (see section 3.2). Table 6 shows the calculation of the corrected chamber measurement M according to formula 8. The raw chamber measurement $\mathrm{M}_{\mathrm{raw}}$ is the amount of charges at the phantom surface. This ion current, induced into the PTW TN30012-10 S/N 000287 farmer chamber at the phantom surface, was measured by the Keithley 35040 electrometer.

Table 6: Calculation of the corrected chamber measurement M

$\mathrm{M}_{\mathrm{raw}}$	36.3800 nC
P_{TP}	1.0158
$\mathrm{P}_{\mathrm{ion}}$	0.9994
$\mathrm{P}_{\mathrm{pol}}$	1.0033
$\mathrm{P}_{\mathrm{elec}}$	1.0000
M	37.0551 nC

Table 7 can be used to calculate the dose to water $D_{w,z=0}$ on top of the water phantom conform to formula 7.

Table 7: Calculation of the dose to water $D_{w,z=0}$ at the phantom surface

M	37.0551 nC
N_K	4.7380 cGy/nC
B_W	1.1995
$P_{stem,air}$	1.0000
$\left[\left(\frac{\bar{\mu}_{en}}{\rho}\right)_{air}^{w}\right]_{air}$	1.0851
$D_{w,z=0}$	228.5290 cGy

Finally, the dose rate at the phantom surface can be calculated using table 8 and formula 9.

Table 8: Calculation of the dose rate $\dot{D}_{w,z=0}$at the phantom surface

$D_{w,z=0}$	228.5290 cGy
T	60.0000 s
δt	0.2667 s
$\dot{\mathrm{D}}_{\mathrm{w,z=0}}$	3.7920 cGy/s

Considering that the EBT3 films were irradiated at the phantom surface, this dose rate would be applicable to the EBT3 films when they were irradiated at this location. Hence, the second step for the construction of the calibration curves was irradiating the EBT3 films with a desired dose by choosing an appropriate exposure time in the X-Rad Small Animal Radiation Therapy device. As such, five different EBT3 films were irradiated with an incrementing exposure time, thereby resulting in five EBT3 films with an incrementing absorbed dose. The EBT3 films were irradiated with absorbed doses ranging from 0 cGy to just over 2400 cGy. For the third and last step, these EBT3 films were scanned in FilmQA Pro at different time intervals, and for each time interval the calibration curve was constructed by linking the absorbed dose to the OD. This OD was the average OD measured in a rectangular ROI placed centrally on the scanned EBT3 film. Figure 30 shows the calibration curve taken at 66 hours after irradiation. For more detailed information, [26] can be consulted since the calibration in this thesis was carried out similarly.

Appendix C: Ionisation chambers

In this thesis, ionisation chambers are used to measure (1) calibrate the source output of the S700 source (well chamber) and for the creation of calibration curves for EBT3 films (farmer chamber). When the x-ray photons pass through the gas filled well chamber, some x-ray photons interact with the gas molecules, splitting them into positive ions and negative electrons [29, 55]. The electric field established between the central electrode and the outer electrode causes the ions and the electrode to drift towards the oppositely charged electrode, which creates a charge in the well chamber measured by the electrometer [29, 55]. This can be retraced to a dose rate using formula 7, formula 8 and formula 9. The design of a well type ionisation chamber and a farmer type ionisation chamber is visualised in figure 54.

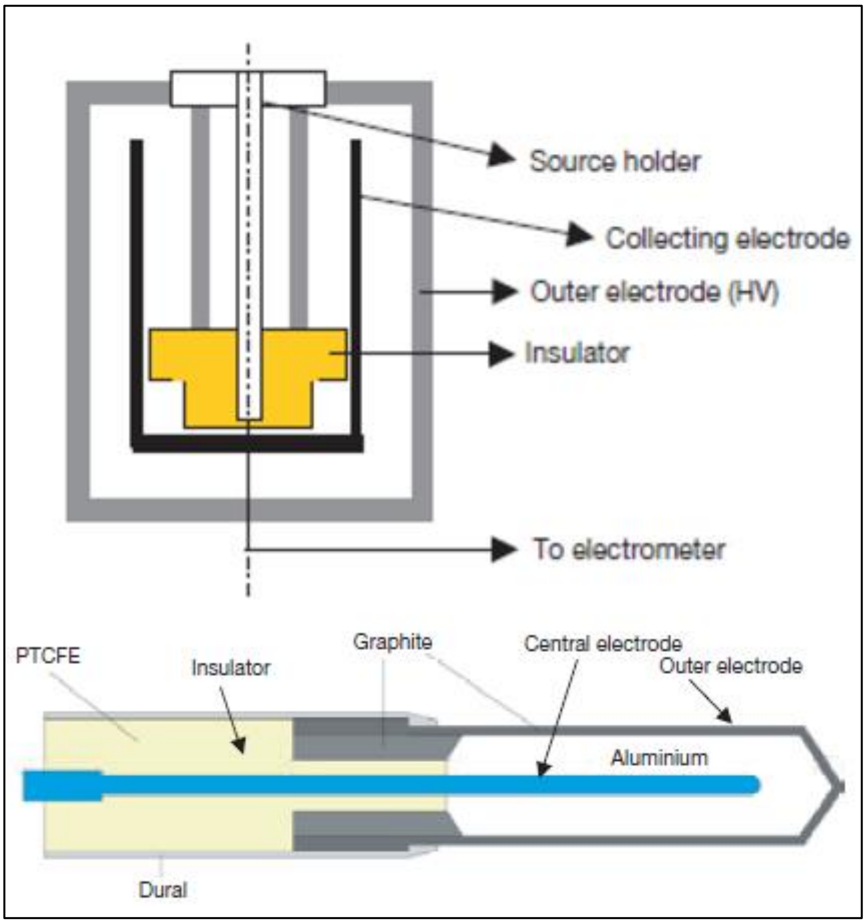

Figure 54: Design of the well type ionisation chamber (above) and the farmer type ionisation chamber (below) [29, p. 81 and p. 77]

Appendix D: Topas

Architecture

A parameter file consisting of a set of lines constructed using the TOPAS Parameter system together with overridable default parameters are the input need for TOPAS to start a simulation. In TOPAS several different parameter files may also be implemented into another parameter file using the includeFile statement. Indeed, the main parameter file run.topas includes parameter files from the folder which is aptly named parameterfiles. These files contain information about the geometry and material selection of the S700 source and the 35 mm applicator as well as files defining the electron beam, the scorer, the used physics which govern the interactions, variance reduction techniques and visualization of the simulation.

Components

The S700 source, the 35 mm applicator, the scorer, the phantom and other components can be built in TOPAS using a combination of geometries and assigned different types of materials. Indeed, the phantoms were defined as boxes of G4_Water in TOPAS while the scorer was defined as a cylinder containing G4_Water. The other components were imported into TOPAS using STL files. The STL format converts geometries to a tessellation using triangular or quadrangular surfaces to approximate the volume. Figure 55 shows the tessellation of the source tip [27].

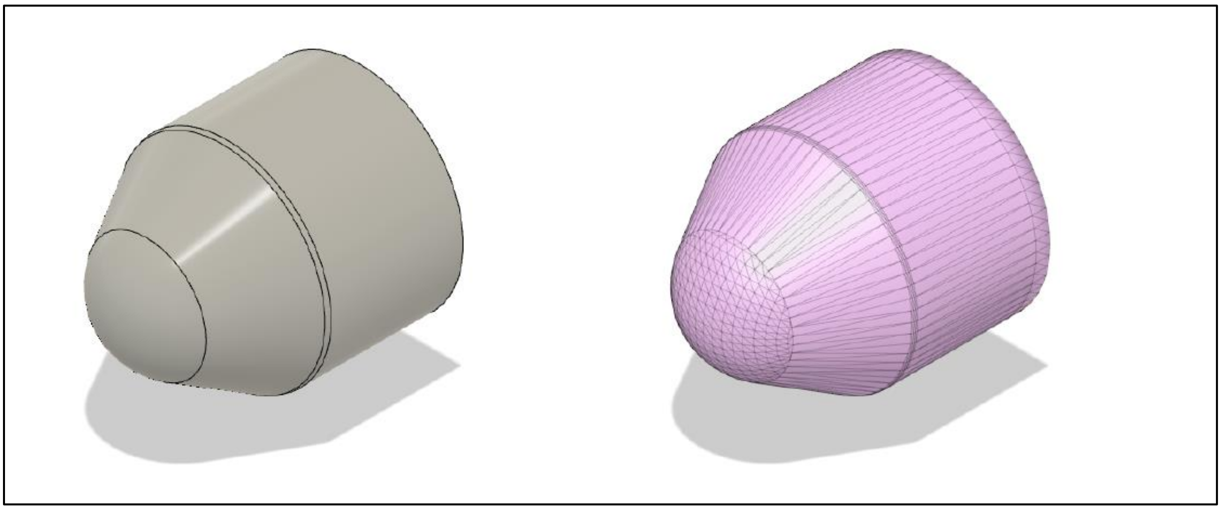

Figure 55: The conversion of the continuous source tip (left) to a tessellated source tip encapsulated by an STL file (right) [26, p.60]

While this function is crucial to simulate complex geometries like the S700 source, some problems were observed when using tessellated solids for MC simulations in TOPAS. Firstly, small overlaps were detected due to triangular facets of one component overlapping with another. To avoid simulations shutting down due to these small overlaps, a tolerance of 25 µm was implemented. The second problem is a bug in Geant4 where an electron can get stuck in a tessellated solid. Indeed, when an electron does not move within 10 steps the particle is killed resulting in no energy transferred to the tessellated solid. To limit the number of electrons getting stuck [26] used MeshLab to (1) align the facets and (2) to make sure they are connected in order to have a closed volume for the original TOPAS MC model. As defined by the creators of Geant4 themselves the impact of these stuck electrons depends on the amount of particles relative to the total amount of electrons in the simulated electron beam. In the simulations for this thesis on average 3 % of $5 * 10^8$ incident electrons were lost to aforementioned phenomenon, which is not negligible but acceptable.